Free-surface flow around a vertical strut in a real fluid
Yu, Xing
ProQuest Dissertations and Theses; 1996; ProQuest Dissertations & Theses Global

INFORMATION TO USERS

This manuscript has been reproduced from the microfilm master. UMI films the text directly from the original or copy submitted. Thus, some thesis and dissertation copies are in typewriter face, while others may be from any type of computer printer.

The quality of this reproduction is dependent upon the quality of the copy submitted. Broken or indistinct print, colored or poor quality illustrations and photographs, print bleedthrough, substandard margins, and improper alignment can adversely affect reproduction.

In the unlikely event that the author did not send UMI a complete manuscript and there are missing pages, these will be noted. Also, if unauthorized copyright material had to be removed, a note will indicate the deletion.

Oversize materials (e.g., maps, drawings, charts) are reproduced by sectioning the original, beginning at the upper left-hand corner and continuing from left to right in equal sections with small overlaps. Each original is also photographed in one exposure and is included in reduced form at the back of the book.

Photographs included in the original manuscript have been reproduced xerographically in this copy. Higher quality 6" x 9" black and white photographic prints are available for any photographs or illustrations appearing in this copy for an additional charge. Contact UMI directly to order.

UMI

A Bell & Howell Information Company
300 North Zeeb Road, Ann Arbor MI 48106-1346 USA
313/761-4700 800/521-0600

Reproduced with permission of the copyright owner. Further reproduction prohibited without permission. www.manaraa.com

Reproduced with permission of the copyright owner. Further reproduction prohibited without permission. www.manaraa.com

Free-Surface Flow Around a Vertical Strut in a Real Fluid

by

Xing Yu

B.Eng. (Shanghai Jiao Tong University) 1986
M.S. (University of California at Berkeley) 1992

A dissertation submitted in partial satisfaction of the

requirements for the degree of

Doctor of Philosophy

in

Engineering-Naval Architecture
and Offshore Engineering

in the

GRADUATE DIVISION

of the

UNIVERSITY of CALIFORNIA at BERKELEY

Committee in charge:

Professor Ronald W. Yeung, Chair
Professor William C. Webster
Professor Stanley A. Berger

1996

Reproduced with permission of the copyright owner. Further reproduction prohibited without permission. www.manaraa.com

UMI Number: 9703331

UMI Microform 9703331
Copyright 1996, by UMI Company. All rights reserved.

This microform edition is protected against unauthorized copying under Title 17, United States Code.

UMI
300 North Zeeb Road
Ann Arbor, MI 48103

Reproduced with permission of the copyright owner. Further reproduction prohibited without permission. www.manaraa.com

The dissertation of Xing Yu is approved:

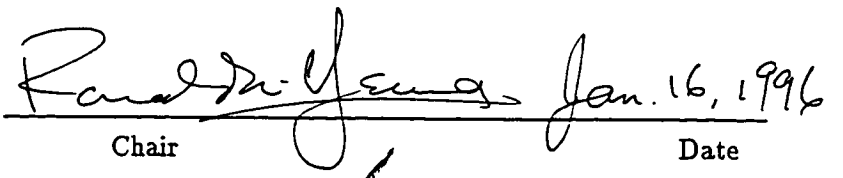

Chair Date

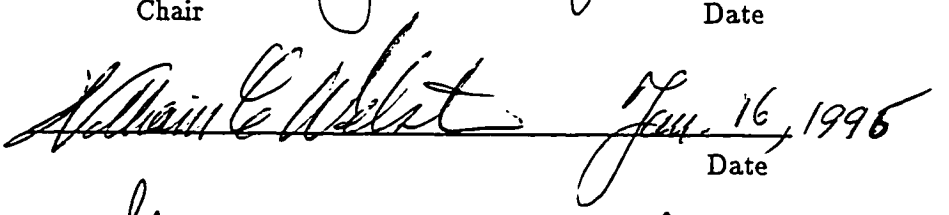

Date

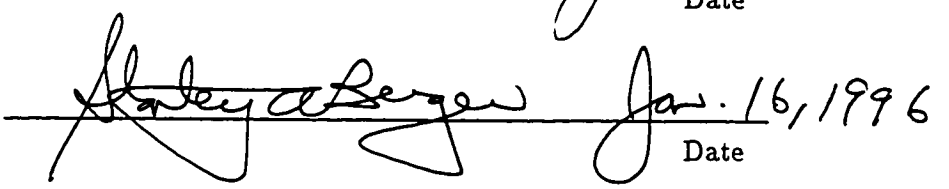

Date

University of California at Berkeley

1996

Reproduced with permission of the copyright owner. Further reproduction prohibited without permission. www.manaraa.com

Contents

Reproduced with permission of the copyright owner. Further reproduction prohibited without permission. www.manaraa.com

Reproduced with permission of the copyright owner. Further reproduction prohibited without permission. www.manaraa.com

Acknowledgements

I wish to express my deepest gratitude to Prof. R. W. Yeung, whose insights in hydrodynamics and ingenuity in numerical analysis have made the completion this dissertation possible. I am grateful for his support and mentorship during the course of my studies at U.C. Berkeley. His commitment to excellence and his dedication to his work have been inspirational to me.

I sincerely thank my thesis committee members, Prof. W. C. Webster and Prof. S. A. Berger, for their help and encouragement during the course of my dissertation work. Special thanks are due to Prof. J. V. Wehausen for many helpful discussions.

During my stay at U.C. Berkeley, M. Vaidhyanathan, M. Parthasarathy, A. Hamilton and D. Roddier have provided help on numerous occasions, especially during some "computer crises". I cannot thank them enough.

My utmost gratitude goes to my parents for the sacrifices they made to make my attendance to graduate school possible and for their support and encouragement during my stay here.

This research has been supported by the Office of Naval Research under Grant N00014-91-J1155 for most part, as well as by Grant N00014-91-J1614 during 1994-95. Partial support is also provided by a Shell Foundation Grant. I would also like to acknowledge the University of California for providing me financial support in the form of the Regents' Fellowship for the year 1992-93 and the Ira Abraham, Sr. and Georgina Koenig Abraham Scholarship for the year 1993-94.

Reproduced with permission of the copyright owner. Further reproduction prohibited without permission. www.manaraa.com

Chapter 1

Introduction

The hydrodynamic interaction between surface gravity waves and ship hulls or marine structures has always been of great interest to naval architects and ocean engineers. Traditionally, this free-surface flow problem has been treated using the *potential-flow theory*, which assumes that the fluid viscosity can be neglected.

Potential-flow theory along with linearized free-surface conditions and higher-order ones have yielded results valid for problems with small-amplitude waves and small body motions. Nonlinear free-surface effects are important when waves are steep and body motions are large. The inviscid models based on mixed Eulerian-Lagrangian approach attributed to Longuet-Higgins and Cokelet (1976) have succeeded in studying some of these nonlinear effects. Some important recent progresses have been made in the development of boundary element methods (e.g. Nakos et al., 1992 and Raven, 1992). These methods are capable of predicting some quantities of interest, e.g. the global wave patterns generated by a moving ship, and forces acting on an oscillating structure. Thorough survey of these inviscid-fluid analyses may be found in Yeung (1982).

Despite the success achieved by the potential-flow theory, there are other cases, in which the effects of fluid viscosity are important, and the inviscid-fluid assumption is thus not appropriate. Some of such cases include the studies of ship wake, large-amplitude motion of marine structures, and nonlinear roll motion of ships. To understand these flow phenomena, one needs to study the flow details near the

Reproduced with permission of the copyright owner. Further reproduction prohibited without permission. www.manaraa.com

body and near the free surface, with the effects of viscosity considered.

1.1 Free-surface flow near a surface-piercing body

It is well known that, for a flow near a wall, the shear layer is formed adjacent to the wall because of vanishing velocity at the wall. In many cases, this shear layer is rather thin, and the inviscid-flow solution is valid exterior of this thin shear layer. This observation led to the famous *boundary-layer theory*, which has been proven successful in analyzing laminar flows over streamlined bodies (e.g. Schlichting, 1968). However, in the case of bluff bodies or in the after portion of a streamlined body, the flow separation results in vortex shedding in the wake. This can only be analyzed using the fully nonlinear *Navier-Stokes equations*. On a free-surface, a shear layer is generated due to the vanishing of shear stress. The free-surface shear layer is usually weak compared to wall boundary layers. It can be shown that the vorticity generation at a free surface is proportional to the surface curvature (see Batchelor, 1970). When the waves are steep, the generation of vortices at the free surface is significant. This process is again governed by the Navier-Stokes equations.

In wave-body interaction problems, owing to the presence of both the wall and the free surface, complex viscous effects are present. Waves interact with the wall boundary layers, and induce flow separations and eddy-shedding. In turn, eddies shed from the bodies interact with the free surface, resulting in wave deformation and generation of secondary vortices. When a ship travels on the ocean surface, it sheds vortices in its wake. This wake pattern is found to be very persistent in time and could sometimes reach 75 kilometers in length (Griffin et al., 1988). This phenomenon is believed to be a complex process which involves the interaction between the vorticity generated by the ship and the surface waves. In the case of steep waves past a bluff structure, waves induce flow separation behind the structure, resulting in significantly different forces.

Another closely related phenomenon is the possible generation and intensification of the so-called necklace vortices from the bow area of a ship. It was observed by Baba (1969) that breaking waves originate at the ship's bow and trail along the hull,

Reproduced with permission of the copyright owner. Further reproduction prohibited without permission. www.manaraa.com

inducing vortices in the shape of a necklace. This upstream wave-breaking contributes significantly to the ship resistance. Baba (1981) claimed that the bow-free-surface juncture bears the same vorticity intensification phenomenon of the "wing-fuselage" juncture of Hawthorne (1954). However, Yeung and Ananthakrishnan (1992) found that a clean free surface was unable to generate a very strong cross-stream vortex. They postulated that the breaking waves around a blunt bow is predominantly driven by gravitational and inertial forces. As their results are for two-dimensional flows, their immediate implications on three-dimensional flows are still not obvious.

In this thesis, the flows near a vertical circular cylinder are examined. Particular attention is on the vortical flow patterns near the body and the free surface. Cylindrical shapes may be viewed as non-ship like, but they are of great practical significance in many marine-related applications. Furthermore, in terms of flow separation, such shapes offer more insights than most streamlined or thin-bodies. With a little increase in mathematical complexity, flows near an elliptical cylinder or a spheroidal hull can be considered as generalizations of the present work. The solution of these three-dimensional, time-dependent, free-surface viscous flow problems requires an accurate, yet efficient numerical method.

1.2 Methods for free-surface flows in a viscous fluid

Although the equations governing viscous free-surface flow problems are nonlinear, and hence are formidable for theoretical analyses, many numerical methods have been developed to solve these problems. However, viscous flow problems are much more difficult to solve than their inviscid counterparts, and no definitive methods have yet been established to be a front runner, depending on the level of resolution to be achieved.

So far most of the Navier-Stokes computations are done by using the *finite difference methods*, which can be divided into two categories: Marker-and-Cell (MAC) method and the boundary-fitted-coordinates method.

Reproduced with permission of the copyright owner. Further reproduction prohibited without permission. www.manaraa.com

Initiated by Harlow and Welch (1966), MAC method uses finite-difference method on a rectangular grid and the free surface is tracked using marked particles. Miyata (1981) used this method to study two-dimensional ship bow-flow problems, and realistically captured viscous-flow phenomena such as eddy shedding under the free surface. Arguing that the viscous-stress conditions are critical only at low Reynolds-numbers, the author applied inviscid conditions at the free surface, and thus was not able to resolve flow details near the free surface. Using finite-volume method, Zhu et al (1993) studied three-dimensional viscous flows about a ship using the *Reynolds-Averaged-Navier-Stokes equations* (RANS) with a hybrid turbulence model. It seems that their method is capable of predicting flow phenomena, such as the flow separation from the hull, the generation of longitudinal vortex, and the resultant wake pattern distortion in the stern region. However, only a "double-body" free surface was implemented in their study.

The implementation of free-surface boundary condition has been greatly improved by the introduction of boundary-fitted-coordinates method, in which the grids conform to the boundary rather than rectangular grids. Shank (1977) first used this method to study flow around a circular cylinder or a hydrofoil. Yeung and Ananthakrishnan (1992) developed a sophisticated grid generation technique to study two-dimensional viscous ship bow flows. Viscosity effects, such as the generation of free-surface shear layer near the bow, the inception of bow vortices, and the effects of surface contaminants were simulated successfully. Tahara and Stern (1994) studied viscous ship flow using the RANS equations with the Baldwin-Lomax turbulence model, nonlinear inviscid free-surface conditions, and a grid based on boundary-fitted coordinates. Chen et al. and Weems et al. (1994) predicted near-field ship flows using RANS equations with a second-order k-ϵ closure turbulence model, nonlinear inviscid free-surface conditions, and boundary-fitted coordinates. To save computational effects, a zonal approach was used in their work, which matches the near-field viscous flow to a potential flow in the far-field. Similar approaches were used by Campana et al (1994) to study the drift motion of a ship, accounting for the viscous effects. Farmer et al. (1994) used a multigrid solution method to simulate viscous ship flows with the Baldwin-Lomax turbulence model and nonlinear inviscid free-surface condi-

Reproduced with permission of the copyright owner. Further reproduction prohibited without permission. www.manaraa.com

tions. The exact viscous free-surface conditions are implemented by Alessandrini and Delhommeau (1994) in their viscous ship flow calculations. In view of these recent developments, the current status of viscous ship hydrodynamics is such that the steady resistance and steady flow can be predicted reasonably well qualitatively, whereas the detailed flow patterns near the ship stern or the free surface are not adequately resolved. There is need for improvement in the area of numerical accuracy, turbulence modeling, and the treatment of free-surface conditions. The numerical accuracy is a concern for all the finite-difference methods, due to the presence of "numerical viscosity", which plagues the solutions at larger Reynolds numbers.

Alternate approaches, which are particularly useful in large Reynolds number flows, are the vortex methods. They are well developed for two-dimensional problems. A primitive form of the vortex methods is the discrete vortex method, in which vortices are generated at each time step at the separation points on the body. A satisfactory solution of the flow past a body using this method was obtained by Sarpkaya (1968). Although this model is only for large Reynolds number, it is widely used due to its simplicity. A vortex method, which is based on Navier-Stokes equations, was originated by Chorin (1973). This method, known as the *random vortex method*, differs from the discrete vortex method in the sense that vortices are generated not only from the separation points, but all around the body to satisfy the no-slip body condition. This method is a grid-free method, which does not suffer from the "numerical viscosity" associated with most of the time-stepping field-discretization methods. This property makes the method particularly suitable for flows of large Reynolds numbers. Since the method was introduced, many improvements have been made, and it has been applied successfully to many fluid flow problems. Stansby and Dixon (1983) simulated uniform and oscillating flows past a circular cylinder in conjunction with a vortex-in-cell method to speed up the computation. Yeung and Vaidhyanathan (1992) developed a random vortex method capable of solving two-dimensional separated flows in the presence of a free surface. This new development allows one to investigate complex free-surface flows using random vortex method. However, because of its extensive computational requirements, it is yet to be extended to three dimensions.

Reproduced with permission of the copyright owner. Further reproduction prohibited without permission. www.manaraa.com

1.3 Spectral methods of solution

The development of higher-order numerical methods has led to the *spectral methods*, which are, at least formally, of infinite-order accuracy. The term "spectral method" does not refer to one particular numerical method, but rather a whole class of numerical methods. They are characterized by the expansion of the solution in terms of, often orthogonal, basis functions, such as a Fourier series. Since the mid-nineteenth century, they have been standard analytical tools for linear, separable differential equations. Nonlinearities presented considerable algebraic difficulties, until they were surmounted effectively in the early 1970s (Orszag 1969). The solution of a variety of boundary value problems using spectral methods was systematically discussed in a monograph by Gottlieb and Orszag (1977). The book by Canuto et al. (1987) contains a detailed description of many spectral algorithms and presents an exhaustive discussion of the theoretical aspects of these numerical methods. A comprehensive review of spectral methods in fluid dynamics is found in Hussaini and Zang (1987). The popularity of these methods arises from several advantages that they have over common finite difference methods. Firstly, they converge rapidly. Secondly, the methods have low or no "numerical viscosity". Thirdly, their computation requirement is low.

The most straightforward class of spectral methods is the *spectral collocation methods*, in which the expansion coefficients are computed so that the differential equation is satisfied exactly at a set of collocation points. After they were introduced by Gottlieb and Orszag (1977), the work of Canuto and Quarteroni (1981) laid down a solid theoretical basis for these methods. Tan (1985) developed an efficient spectral collocation method to solve three-dimensional Poisson's equation and Helmholtz's equation using Chebyshev series and Fourier series. A review which covers the theory and application of these collocation methods is found in Hussaini et al (1989).

Although, as pointed out by Orszag (1980), spectral collocation methods can be used to deal with general geometries through mappings, they are generally unsuitable for complex geometries. A new technique that combines the ideas of spectral methods with those of finite element methods is the *spectral element methods*.

Reproduced with permission of the copyright owner. Further reproduction prohibited without permission. www.manaraa.com

These combined methods have the advantages of both methods: the high efficiency and accuracy of a spectral method, and the geometrical flexibility of a finite element method. Patera (1984) studied two-dimensional separated flow in a channel expansion using rectilinear spectral elements. Korczak and Patera (1986) extended the former work to solve two-dimensional viscous flow in arbitrary geometries using isoparametric spectral elements. Tan (1989) combined the above two-dimensional isoparametric spectral element technique and a Chebyshev expansion in the third direction, to study three-dimensional flow past a strut. Numerical results were obtained for Reynolds number up to 1,000. Karniadakis et al (1986) used spectral element methods to study vortex shedding phenomenon after a cylinder, and their numerical results achieved good agreements with the experimental results. Spectral method today has become the principal solution technique in simulation of turbulent flow and the computation of transition to turbulence.

In this thesis, a spectral collocation method is developed to solve free-surface flow problems near a surface-piercing body for both inviscid and viscous fluids.

1.4 Thesis outline

The thesis is complied as follows. In Chapter 2, the theoretical background for transient three-dimensional *inviscid* free-surface flow is briefly reviewed. A spectral collocation method for solving these problems is introduced and detailed. Specifically, a spectral Poisson equation solver is developed in cylindrical coordinates. In Chapter 3, after numerical validation and accuracy assessment, the spectral Poisson equation solver is applied to solve several three-dimensional inviscid free-surface flow problems of practical interest. These include: a Cauchy-Poisson wave problem, a radiation problem of a circular cylinder, and a second-order wave diffraction problem by a circular cylinder. In Chapter 4, the governing equations and boundary conditions for solving *viscous* free-surface flow problems are formulated. A numerical procedure for solving this viscous-flow problem by a spectral collocation method is explained. This methodology is based on the projection method originally proposed by Chorin (1968), but implemented with an ADI scheme and a spectral-collocation technique.

Reproduced with permission of the copyright owner. Further reproduction prohibited without permission. www.manaraa.com

The numerical results for *viscous* flow problems are given in Chapter 5. Several test problems are first shown to establish the overall accuracy. Numerical results for a viscous Cauchy-Poisson wave problem, for uniform flows past a circular cylinder under a free-slip surface and a real free surface are presented. The complex vortical flow phenomena near the body and the free surface are examined and discussed. Chapter 6 summarizes the present work and addresses some possible future extensions to this research.

Reproduced with permission of the copyright owner. Further reproduction prohibited without permission. www.manaraa.com

Chapter 2

Spectral method for inviscid flow problem

In this chapter, the theoretical background for solving transient three-dimensional inviscid free-surface flow will be detailed. The mathematical formulation will be first described, and the numerical treatment will follow.

The following notations are adopted in this thesis: vector quantities and matrices are shown in bold faces (e.g., $\mathbf{x}$), complex quantities in sans serif type (e.g., $\mathsf{i} = \sqrt{-1}$), and dimensional quantities are marked by a prime "′".

Let there be a characteristic length L' and a characteristic velocity U' associated with the flow to be studied. All variables and parameters used henceforth will be taken as non-dimensionalized with respect to L', U' and the fluid density ρ', unless otherwise stated. The appropriate characteristic length and velocity for each problem to be studied will be different and will be specified when necessary.

2.1 Problem formulation

Consider a fixed cylindrical coordinate system (r', θ, z') chosen so that the $z'-$axis points vertically upwards and the undisturbed free-surface is at $z' = 0$ (see Fig. 2.1). The fluid region Ω is enclosed by the cylindrical body boundary $\mathcal{S}$ located at $r' = r'_i$, free-surface $\mathcal{F}$ at $z' = 0$, far-field boundary Σ at $r' = r'_o$, and a bottom $\mathcal{B}$

Reproduced with permission of the copyright owner. Further reproduction prohibited without permission. www.manaraa.com

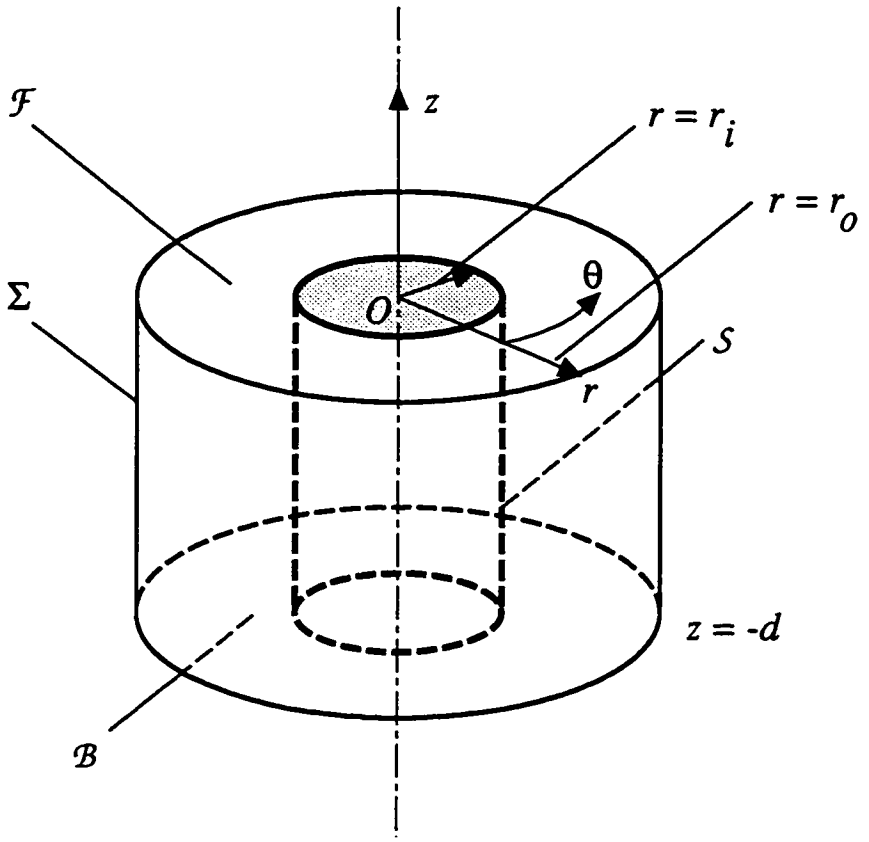

Figure 2.1: Notation and coordinate system.

located at $z' = -d'$. We first choose the take the following two characteristic scales: length $L' = r_i'$, velocity $U' = \sqrt{g' r_i'}$, where g' denotes gravitational acceleration.

Field equation

Under the assumptions that the flow is irrotational and the fluid incompressible, it can be shown that there exists a velocity potential of the flow ϕ, which satisfies the Laplace equation

$$\nabla^2 \phi = 0 \tag{2.1}$$

in the domain Ω, with the following boundary conditions (see e.g. Wehausen and Laitone, 1960).

Reproduced with permission of the copyright owner. Further reproduction prohibited without permission. www.manaraa.com

Boundary and initial conditions

On free surface $\mathcal{F}$, if one further assumes that the wave elevation is small compared with wave length, the following linerized dynamic condition

$$\frac{\partial \phi}{\partial t} = -\eta, \qquad z = 0 \tag{2.2}$$

can be derived using Euler's integral. By integrating the above Eqn. (2.2) with respect to time t, one can obtain a Dirichlet condition for ϕ. Here $\eta(r, \theta, t)$ is the free-surface elevation, which satisfies the following linearized kinematic condition:

$$\frac{\partial \eta}{\partial t} = \frac{\partial \phi}{\partial z}, \qquad z = 0. \tag{2.3}$$

The exact or nonlinear conditions on the free surface can be found in Wehausen and Laitone (1960). On body $\mathcal{S}$, the no-leak condition provides the following Neumann condition:

$$\phi_n = \mathbf{V} \cdot \mathbf{n}, \tag{2.4}$$

where $\mathbf{n}$ is a normal on the body surface pointing outwards of Ω, and $\mathbf{V}$ the prescribed normal-component of the boundary velocity. On bottom $\mathcal{B}$, the following no-leak condition is applicable:

$$\phi_z = 0. \tag{2.5}$$

On the surface Σ, if it is a solid boundary,

$$\phi_n = 0. \tag{2.6}$$

If Σ is taken as a far-field boundary, we may impose

$$\phi = 0 \tag{2.7}$$

as an approximation for an open boundary, provided Σ is taken to be sufficiently large so that no wave disturbances reach Σ. Alternatively, one might consider a time-dependent Sommerfeld type radiation condition as examined in Yeung and Vaidhyanathan (1992) or a matching condition of Yeung (1985). In both cases, it can be treated as a mixed boundary condition within the present framework of solution.

To complete the problem, initial conditions for ϕ and its derivatives ϕ_z on $\mathcal{F}$ should be specified.

Reproduced with permission of the copyright owner. Further reproduction prohibited without permission. www.manaraa.com

Calculation of force and moment

After the hydrodynamic problem for ϕ is solved, the horizontal force F_x on the cylinder and overturning moment M_y about the sea bottom can be obtained by integrating the hydrodynamic pressure using the linearized Euler's integral:

$$F_x = \int_S p n_x dS = -\int_S \rho \phi_t n_x dS, \tag{2.8}$$

$$M_y = \int_S p n_x (z+d) dS = -\int_S \rho \phi_t n_x (z+d) dS. \tag{2.9}$$

These forces are non-dimensionalized here by $\rho' U'^2 r_i'^2$, moment by $\rho' U'^2 r_i'^3$.

2.2 Pseudo-spectral method of solution

2.2.1 A Poisson-equation solver

The solution of Eqn. (2.1) may be considered as a special application of a Poisson solver which is also needed in a number of closely related fluid-mechanics problems, such as the solution of pressure equation in viscous flow problems (to be studied in Chapter 3). Here we will develop a pseudo-spectral formulation using ideas similar to Tan (1985). For the present problem in cylindrical coordinates, we will use Chebyshev polynomials in the vertical direction and Fourier modes in the circumferential direction. The resulting finite-difference equations for the radial direction are treated by a diagonalization technique. The method developed can treat both homogeneous and inhomogeneous boundary conditions of the Dirichlet, Neumann, or mixed type.

For the right-handed cylindrical coordinate system (r, θ, z) shown in Fig. 2.1, the independent variables are defined in the following ranges:

$$\begin{aligned} r_i &\leq r \leq r_o \\ 0 &\leq \theta \leq 2\pi \\ -d &\leq z \leq 0 \end{aligned} \tag{2.10}$$

where r_i and r_o are the radii of the inner and outer cylindrical boundaries respectively. It is convenient to map the above domain into a normalized computational domain

Reproduced with permission of the copyright owner. Further reproduction prohibited without permission. www.manaraa.com

(R, Φ, Z) such that

$$\begin{aligned} -1 &\leq R \leq 1 \\ -1 &\leq \Phi \leq 1 \\ -1 &\leq Z \leq 1 \end{aligned} \tag{2.11}$$

by using the following relations:

$$\begin{aligned} r &= \zeta R + \xi \\ \theta &= (1+\Phi)\pi \\ z &= \kappa(-1+Z) \end{aligned} \tag{2.12}$$

where $\zeta = \frac{1}{2}(r_o - r_i)$, $\xi = \frac{1}{2}(r_o + r_i)$, and $\kappa = d/2$ are scale and translational factors.

In (R, Φ, Z), the Poisson equation $\nabla^2 U = S(R, \Phi, Z)$ can be written as:

$$\left[\mathcal{L} + \frac{1}{(\zeta R+\xi)^2\pi^2}\frac{\partial^2}{\partial\Phi^2} + \frac{\partial^2}{\kappa^2\partial Z^2}\right] U(R,\Phi,Z) = S(R,\Phi,Z) \tag{2.13}$$

where

$$\mathcal{L} \equiv \frac{1}{\zeta^2}\frac{\partial^2}{\partial R^2} + \frac{1}{\zeta(\zeta R+\xi)}\frac{\partial}{\partial R}. \tag{2.14}$$

Here we use U to designate the more general case of an unknown function where the Poisson instead of the Laplace equation is satisfied. Clearly, for inviscid-fluid applications, one would simply take the source term $S = 0$.

The boundary conditions in Eqns. (2.2), (2.3), (2.5), (2.6) or (2.7) can be treated as special cases of the following generalized forms:

$$\alpha_\pm U(\Phi, Z) + \beta_\pm \frac{\partial U(\Phi, Z)}{\partial R} = F_\pm(\Phi, Z), \quad \text{at} \quad R = \pm 1 \tag{2.15}$$

$$A_\pm U(R, \Phi) + B_\pm \frac{\partial U(R, \Phi)}{\partial Z} = H_\pm(R, \Phi), \quad \text{at} \quad Z = \pm 1 \tag{2.16}$$

with all $\alpha_\pm$, $\beta_\pm$, $A_\pm$, and $B_\pm$ considered given constants.

Chebyshev-Fourier expansion

In our spectral approach to the solution of Eqn. (2.13), the functions U, S, $F_\pm$, and $H_\pm$ are approximated by truncated Chebyshev-Fourier series of the form:

$$\begin{Bmatrix} U(R,\Phi,Z) \\ S(R,\Phi,Z) \\ F_\pm(\Phi,Z) \end{Bmatrix} = \sum_{m=-\frac{M}{2}}^{\frac{M}{2}-1} \sum_{n=0}^{N} \begin{Bmatrix} U_{mn}(R) \\ S_{mn}(R) \\ f_{\pm mn} \end{Bmatrix} e^{im\pi\Phi} T_n(Z), \quad \mathrm{i} = \sqrt{-1}, \tag{2.17}$$

Reproduced with permission of the copyright owner. Further reproduction prohibited without permission. www.manaraa.com

and

$$H_{\pm}(R,\Phi) = \sum_{m=-\frac{M}{2}}^{\frac{M}{2}-1} h_{\pm mn}(R) e^{im\pi\Phi}, \tag{2.18}$$

where the Chebyshev polynomials $T_n(Z)$ are given by $\cos[n\cos^{-1} Z]$. Here M and N are the number of modes in Fourier and Chebyshev series respectively. Note that by assumption, we consider S_{mn}, $f_{\pm mn}$, and $h_{\pm mn}$ as given, while the sequence U_{mn} are unknown functions to be solved.

By introducing a Chebyshev-Tau representation (Gottlieb and Orszag, 1977) to incorporate the boundary conditions (2.16) at $Z = \pm 1$, and by applying the recurrence relations for the derivatives of Chebyshev polynomials, we can rewrite:

$$\frac{\partial^2 U}{\partial Z^2} = \sum_{m=-\frac{M}{2}}^{\frac{M}{2}-1} \sum_{n=1}^{N-1} U_{mn}^{(0,2)}(R) e^{im\pi\Phi} T_n(Z), \tag{2.19}$$

where

$$U_{mn}^{(0,2)}(R) = \sum_{q=0}^{N-2} \gamma_{nq} U_{mq}(R) + D_{mn}(R). \tag{2.20}$$

Expressions for γ_{nq} and $D_{mn}(R)$ can be derived and their lengthy expressions are listed in Appendix A. Substitution of the above results (Eqns. 2.19 and 2.20) into the Poisson equation (2.13) yields:

$$\left[\mathcal{L} - \frac{m^2}{(\zeta R+\xi)^2}\right] U_{mn}(R) + \frac{1}{\kappa^2} \sum_{q=0}^{N-2} \gamma_{nq} U_{mq}(R) = S_{mn}(R) - \frac{1}{\kappa^2} D_{mn}(R) \equiv \sigma_{mn}(R) \tag{2.21}$$

for $m = -\frac{M}{2}$ to $\frac{M}{2} - 1$, and $n = 1$ to $N - 1$.

Diagonalization

To avoid solving Eqn. (2.21) with full coupling between m with n, we first proceed to diagonalize a matrix Γ consisting of elements γ_{nq}. Γ is of dimension $N-1$. Thus we assume

$$\epsilon^{-1}\Gamma\epsilon = \Lambda, \tag{2.22}$$

where Λ is a *diagonal* matrix of dimension $N-1$ with diagonal elements λ_n, $n = 1,..,N-1$, as the eigenvalues. ϵ is the associate eigenvector *matrix*, and ϵ^{-1} its

Reproduced with permission of the copyright owner. Further reproduction prohibited without permission. www.manaraa.com

inverse. Next, if we consider the matrices $\mathbf{U}$ and $\mathbf{\Sigma}$ to be defined by elements U_{mn} and σ_{mn}, we may define correspondingly a matrix $\hat{\mathbf{U}}$ with elements $\hat{U}_{mn}$ and $\hat{\mathbf{\Sigma}}$ with elements $\hat{\sigma}_{mn}$ by the following relations:

$$\begin{aligned} \mathbf{U} &= \hat{\mathbf{U}}\boldsymbol{\epsilon}^T, \\ \mathbf{\Sigma} &= \hat{\mathbf{\Sigma}}\boldsymbol{\epsilon}^T, \end{aligned} \tag{2.23}$$

where the superscript T denotes transpose.

Thus by Eqns. (2.22) and (2.23), Eqn. (2.21) reduces to

$$\left[\mathcal{L} - \frac{m^2}{(\zeta R + \xi)^2}\right] \hat{U}_{mn}(R) + \frac{1}{\kappa^2}\lambda_n \hat{U}_{mn}(R) = \hat{\sigma}_{mn}(R), \tag{2.24}$$

or more explicitly

$$\hat{U}''_{mn}(R) + \frac{\zeta}{\zeta R + \xi}\hat{U}'_{mn}(R) + \zeta^2\left[\frac{\lambda_n}{\kappa^2} - \frac{m^2}{(\zeta R + \xi)^2}\right]\hat{U}_{mn}(R) = \zeta^2 \hat{\sigma}_{mn}(R), \tag{2.25}$$

for $m = -\frac{M}{2}$ to $\frac{M}{2} - 1$, and $n = 1$ to $N - 1$. The significance of Eqn. (2.25), in comparison with Eqn. (2.21), is that the system of ordinary differential equations in Eqn. (2.25) is uncoupled in m and n. Had we not made this transformation, we would have to face with the insurmountable task of solving $m \times n$ coupled differential equations.

Solution of ordinary differential equation

To solve the system of ODEs defined in Eqn. (2.25), we may either employ a finite-difference scheme or a Chebyshev collocation method (Hussaini et al., 1989). The latter is found to be much more accurate than the former, and is used in acquiring most of the results in this thesis. The details for both are explained below.

Finite-difference method of solution: If we choose to use a second-order differencing algorithm over a uniform grid of spacing h in the $R-$direction, Eqn. (2.25) can be rewritten as

$$\begin{aligned} \left[\frac{1}{h^2\zeta^2} + \frac{1}{2h\zeta(\zeta R_l + \xi)}\right]\hat{U}^{(l+1)}_{mn} + \left[-\frac{2}{h^2\zeta^2} + \frac{\lambda_n}{\kappa^2} - \frac{m^2}{(\zeta R_l + \xi)^2}\right]\hat{U}^{(l)}_{mn} \\ + \left[\frac{1}{h^2\zeta^2} - \frac{1}{2h\zeta(\zeta R_l + \xi)}\right]\hat{U}^{(l-1)}_{mn} = \hat{\sigma}^{(l)}_{mn}, \end{aligned} \tag{2.26}$$

Reproduced with permission of the copyright owner. Further reproduction prohibited without permission. www.manaraa.com

where $\hat{U}_{mn}^{(l)}$, $l = 2, ..., L-2$, represent the discrete values of $\hat{U}_{mn}(R)$ at $R = R^{(l)}$ with $R^{(l)} \equiv -1+2l/L$. The boundary conditions at $R = \pm 1$ are also discretized, according to Eqn. (2.15), as

$$\left[\alpha_- - \frac{3\beta_-}{2h}\right]\hat{U}_{mn}^{(0)} + \frac{2\beta_-}{h}\hat{U}_{mn}^{(1)} - \frac{\beta_-}{2h}\hat{U}_{mn}^{(2)} = \hat{f}_{-mn} \tag{2.27}$$

$$\frac{\beta_+}{2h}\hat{U}_{mn}^{(L-2)} - \frac{2\beta_+}{h}\hat{U}_{mn}^{(L-1)} + \left[\alpha_+ + \frac{3\beta_+}{2h}\right]\hat{U}_{mn}^{(L)} = \hat{f}_{+mn}, \tag{2.28}$$

where $\hat{f}_{\pm mn}$ are elements of matrix $\hat{\mathbf{F}}_\pm = \mathbf{F}_\pm(\epsilon^T)^{-1}$, with $\mathbf{F}_\pm$ being the matrix containing elements $f_{\pm mn}$. The systems (Eqns. 2.26 to 2.28) yield a set of linear equations with a tridiagonal matrix, which can be solved very efficiently by the Thomas' algorithm (Press et al., 1989).

Spectral-collocation method of solution: A more accurate, although more laborious, way to solve the ODEs in Eqn. (2.25) is to use a spectral collocation method with a Chebyshev spacing in the R–direction. We first expand the unknow function $\hat{U}_{mn}(R)$ at collocation points R_l ($l = 0, ..., L$) into a Chebyshev series

$$\hat{U}_{mn}(R_l) = \sum_{j=0}^{L} a_{mn}^{(j)} T_j(R_l), \tag{2.29}$$

where $T_j(R_l) = \cos(j \cos^{-1} R_l)$. If we assume R_l satisfying a Chebyshev spacing in the R–direction as $R_l = -\cos\frac{\pi}{L}l$, we have

$$\hat{U}_{mn}(R_l) = \sum_{j=0}^{L} a_{mn}^{(j)}(-1)^j \cos\frac{\pi}{L}jl. \tag{2.30}$$

Then the first two derivatives of $\hat{U}_{mn}(R)$ are given by

$$\begin{aligned}
\hat{U}'_{mn}(R_l) &= \sum_{j=0}^{L} a_j(-1)^{j+1}\frac{j}{\sin\frac{\pi}{L}l}\sin\frac{\pi}{L}jl \\
\hat{U}''_{mn}(R_l) &= \sum_{j=0}^{L} a_j\frac{R_l T'_j(R_l) - l^2 T_j(R_l)}{1 - {R_l}^2}.
\end{aligned} \tag{2.31}$$

Substituting Eqns. (2.30) and (2.31) into Eqn. (2.25), we have

$$\sum_{j=0}^{L} A_{mn}^{(lj)} a_{mn}^{(j)} = \zeta\hat{\sigma}_{mn}(R_l) \tag{2.32}$$

Reproduced with permission of the copyright owner. Further reproduction prohibited without permission. www.manaraa.com

where

$$A_{mn}^{(lj)} = \frac{j \sin \frac{\pi}{L} jl}{\sin \frac{\pi}{L} l} \left[\frac{R_l}{1 - {R_l}^2} + \frac{\zeta}{\zeta R_l + \xi} \right] + \cos \frac{\pi}{L} jl \left[\zeta^2 \left(\frac{\lambda_n}{\kappa^2} - \frac{m^2}{\zeta R_l + \xi^2} \right) - \frac{j^2}{1 - {R_l}^2} \right], \tag{2.33}$$

for $l = 1, ..., L-1$. Using the following relations

$$T_j(1) = 1, \quad T_j(-1) = (-1)^j, \quad T_j'(1) = j^2, \quad \text{and} \quad T_j'(-1) = (-1)^{j+1} j^2, \tag{2.34}$$

we may write the boundary conditions in Eqn. (2.16) as

$$\begin{aligned} \sum_{j=0}^{L} A_{mn}^{(0j)} a_{mn}^{(j)} &= f_{-mn} \\ \sum_{j=0}^{L} A_{mn}^{(Lj)} a_{mn}^{(j)} &= f_{+mn} \end{aligned} \tag{2.35}$$

where

$$A_{mn}^{(0j)} = \alpha_-(-1)^j + \beta_-(-1)^{j+1} j^2 \tag{2.36}$$

and

$$A_{mn}^{(Lj)} = \alpha_+ + \beta_+ j^2 \tag{2.37}$$

The above linear systems (Eqns. 2.32 to 2.35) with a full matrix can be solved most accurately with a direct method, or by an iterative method (Orszag, 1980), which is efficient, yet less accurate. In the actual implementation, we use the direct method to assure accuracy.

2.2.2 Treatment of the free-surface conditions

As pointed out earlier, the potential ϕ and wave elevation η on the free surface $\mathcal{F}$ are obtained by integrating Eqns. (2.2) and (2.3) respectively. Implicit difference schemes are used here because of their excellent stability properties (see e.g. Yeung, 1982). To implement such schemes, the following iterative procedure is employed

$$\begin{aligned} \eta_{(p+1)}^{k+1} &= \eta^k + \frac{\Delta t}{2} (\phi_{z(p)}^{k+1} + \phi_z^k) \\ \phi_{(p+1)}^{k+1} &= \phi^k - \frac{\Delta t}{2} (\eta_{(p)}^{k+1} + \eta^k). \end{aligned} \tag{2.38}$$

Reproduced with permission of the copyright owner. Further reproduction prohibited without permission. www.manaraa.com

Here the superscript k denotes an index of the time step and p denotes the index of iterations within a given time step. The iteration process is halted after the pth iteration when

$$|\phi_{z(p)}^{k+1} - \phi_{z(p-1)}^{k+1}| \leq \epsilon, \tag{2.39}$$

where ϵ is a prescribed tolerance value.

It is worthwhile to notice that the particular implicit free-surface conditions in Eqns. (2.38) can also be implemented *without* iterations. By eliminating η^{k+1} from the two equations in Eqns. (2.38), we have

$$\phi^{k+1} + (\frac{\Delta t}{2})^2 \phi_z^{k+1} = \phi^k - \Delta t \eta^k - (\frac{\Delta t}{2})^2 \phi_z^k, \tag{2.40}$$

which is mixed boundary condition for ϕ^{k+1} in the form of Eqn. (2.16). Although the boundary condition in Eqn. (2.40) can be implemented most efficiently in the present formulation, the iterative schemes in Eqn. (2.38) are useful in the treatment of free-surface conditions in moving coordinates, which involve tangential derivatives. In this thesis, Eqn. (2.40) is used throughout in numerical computation.

Reproduced with permission of the copyright owner. Further reproduction prohibited without permission. www.manaraa.com

Chapter 3

Results for inviscid flow

In this chapter, the spectral Poisson solver developed in Section 2.2 will be applied to solve the Laplace equation governing an inviscid flow.

3.1 Analytical validations

Before proceeding to some general and more complex problems, it is essential to establish the accuracy and convergence characteristics of the procedure presented in Chapter 2. For this purpose, we test the procedure against two analytical solutions that can be worked out relatively easily.

3.1.1 Solution of Poisson equation

As a first test case, we wish to verify that the Poisson solver for Eqn. (2.13) to (2.16) can treat any arbitrary function of S accurately and efficient. Here we assume an analytical form of $U(r, \theta, z)$, and evaluate $S(r, \theta, z)$ accordinging to Eqn. (2.13). The boundary conditions (2.15) and (2.16) can be imposed by taking the left-hand side as given and the right-hand side computed. Then the numerical algorithm for the solution of U is applied with S, F, and H as given. The numerical solution can then be compared with the exact solution for different types of boundary conditions.

Reproduced with permission of the copyright owner. Further reproduction prohibited without permission. www.manaraa.com

For this test, we take $U(r,\theta,z)$ as

$$U(r,\theta,z) = A(r)B(\theta)C(z), \tag{3.1}$$

where

$$\begin{aligned} A(r) &= \left[\cos\left\{\frac{\pi}{2}\left(\frac{r-\xi}{\zeta}-1\right)\right\} + \sin\left\{\frac{\pi}{2}\left(\frac{r-\xi}{\zeta}-1\right)\right\}\right], \\ B(\theta) &= \left[\cos\left\{\pi\left(\frac{\theta}{2\pi}-1\right)\right\} + \sin\left\{\pi\left(\frac{\theta}{2\pi}-1\right)\right\}\right], \\ C(z) &= \left[\cos\left\{\frac{\pi}{2}(z-1)\right\} + \sin\left\{\frac{\pi}{2}(z-1)\right\}\right]. \end{aligned} \tag{3.2}$$

The dimensions of the domain are taken as $r_i = 1$, $r_o = 10$ and $d = 2$. The right-hand-side of the Poisson equation $S(r,\theta,z)$ is thus given

$$\begin{aligned} S(r,\theta,z) = &-\frac{\pi}{2}\frac{\zeta B(\theta)C(z)}{r-\xi}\left[\sin\left\{\frac{\pi}{2}\left(\frac{r-\xi}{\zeta}-1\right)\right\} + \cos\left\{\frac{\pi}{2}\left(\frac{r-\xi}{\zeta}-1\right)\right\}\right] \\ &- \left[\frac{\zeta^2}{(r-\xi)^2} + \frac{\pi^2}{2}\right] A(r)B(\theta)C(z). \end{aligned} \tag{3.3}$$

The boundary conditions considered are taken to be one of the following three types:

$$\begin{aligned} &\text{Dirichlet Conditions:} && \alpha_\pm = A_\pm = 1, \quad \beta_\pm = B_\pm = 0, \\ &\text{Neumann Conditions:} && \alpha_\pm = A_\pm = 0, \quad \beta_\pm = B_\pm = 1, \\ &\text{Mixed Conditions:} && \alpha_\pm = A_\pm = 1, \quad \beta_\pm = B_\pm = 1. \end{aligned} \tag{3.4}$$

Once the solution for U has been obtained, its pointwise error can be computed over the entire domain Ω. In Fig. 3.1, the maximum pointwise error of the numerical solution in Ω, relative to the exact analytical solution, is shown for a range of grid resolution. In these and later computations, the grid resolution is measured by the number of radial grids, L, and the number of spectral terms in the circumferential direction, M, and the number of spectral terms in the vertical direction, N. For the specific case in question, we take $L = M = N$, with N ranging from 8 to 32. For comparison purpose, the second-order differencing scheme and the spectral collocation method discussed in Sec. 2.2.1 are both implemented to solve the ODE

Reproduced with permission of the copyright owner. Further reproduction prohibited without permission. www.manaraa.com

in Eqn. (2.25). Fig. 3.1 shows that the value of the error, Er decreases exponentially as the grid resolution N increases for each of the above three types of boundary conditions. Specifically, we observe that

$$Er \sim 10^{-N/N_0}, \tag{3.5}$$

where N_0 is of the order of 20 when the finite-difference scheme is used, and is of order 1 for the spectral collocation method (before the machine accuracy is reached). Fig. 3.1 also shows that primary source of error comes from the discrete approximation in the radial direction. The spectral collocation scheme for solving Eqn. (2.25) yields errors so small that machine accuracy (14 digits) is reached by using merely $L = M = N = 16$.

3.1.2 An axisymmetric Cauchy-Poisson wave problem

To test the accuracy of the algorithm in the handling of wave-related problems, we solve, as the second test case, an axisymmetric Cauchy-Poisson wave problem (see e.g. Lamb, 1932). In this type of problems, one first specifies an initial elevation or velocity of the surface wave, and is then faced with the prediction of the wave evolution at subsequent time. Here we choose characteristic length and velocity as $L' = r_i'$ and $U' = \sqrt{g'r_i'}$, respectively. The governing equations are given in Chapter 2, with the initial conditions to be specified. Here we assume the initial conditions to be of an *axi-symmetric* wave form that occurs between two concentric impermeable vertical cylinders located at $r = r_i$ ($\mathcal{S}$), and at $r = r_o$ (Σ)

$$\frac{\partial \phi}{\partial t} = \exp\left\{-[r - (r_i + r_o)/2]^2\right\} \equiv f(r), \quad \text{at } t = 0 \tag{3.6}$$

$$\phi = 0, \quad \text{at } t = 0 \tag{3.7}$$

An analytical solution of the above problem can be derived by the use of Laplace transform and separation of variables. The details are omitted here. The final results in terms of velocity potential $\phi(r, z, t)$ and wave elevation $\eta(r, t)$ are given as

$$\phi(r, z, t) = \sum_{n=0}^{\infty} g_n \left[J_0(k_n r) - \frac{J_1(k_n r_i)}{N_1(k_n r_i)} N_0(k_n r)\right] \frac{\cosh k_n(z + d)}{\cosh k_n d} \frac{\sin \omega_n t}{\omega_n}, \tag{3.8}$$

Reproduced with permission of the copyright owner. Further reproduction prohibited without permission. www.manaraa.com

and

$$\eta(r,t) = g_0 + \sum_{n=1}^{\infty} g_n \left[J_0(k_n r) - \frac{J_1(k_n r_i)}{N_1(k_n r_i)} N_0(k_n r) \right] \cos \omega_n t, \tag{3.9}$$

where J_ν and N_ν are the Bessel functions of the first and the second kinds of order ν. k_n is the nth zero of the following equation for k

$$J_1(kr_i)N_1(kr_o) - J_1(kr_o)N_1(kr_i) = 0. \tag{3.10}$$

The "natural" frequencies ω_n satisfy a finite-depth "dispersion relation":

$$\omega_n^2 = k_n \tanh k_n d. \tag{3.11}$$

The coefficients g_n in Eqn. (3.9) are given analytically in terms of $f(r)$:

$$g_m = \frac{\int_{r_i}^{r_o} r f(r) dr}{\int_{r_i}^{r_o} r dr} \quad \text{for } m = 0 \tag{3.12}$$

and

$$g_m = \frac{\int_{r_i}^{r_o} r f(r) \left[J_0(k_m r) - \frac{J_1(k_m r_i)}{N_1(k_m r_i)} N_0(k_m r) \right] dr}{\int_{r_i}^{r_o} r \left[J_0(k_m r) - \frac{J_1(k_m r_i)}{N_1(k_m r_i)} N_0(k_m r) \right]^2 dr} \quad \text{for } m = 1, 2, 3.... \tag{3.13}$$

The numerical solution of this problem was obtained using the spectral method described in Chapter 2. Here the geometry of the domain is taken to be $r_o = 10$ and $d = 2$. The results of the computed wave elevation $\eta_c(r,t)$ were compared with the corresponding analytical solution $\eta_a(r,t)$ given by Eqn. (3.9). Excellent agreement was found at every value of non-dimensional time t. Fig. 3.2a shows the free-surface elevation for one such simulation at $t = 100.0$. The RMS error in free-surface elevation as a function of time is defined as

$$E_{RMS}(t) = \sqrt{\frac{\int_S \{[\eta_c(r,t) - \eta_a(r,t)]/\eta_0\}^2 dS}{S}} \tag{3.14}$$

where η_o is the elevation for the initial free-surface pulse, and S the planform area of the free surface. A plot of $E_{RMS}(t)$ versus time-step index n is given in Fig. 3.2b. For $L = 100$, $M = 24$ and $N = 24$, the error is found to be bounded by 0.5% when a nondimensional time step Δt of 0.1 is used, but reduced drastically to a mere 0.05% if the time step is halved to 0.05. These results lend credence to the accuracy of the method in solving free-surface problems.

Reproduced with permission of the copyright owner. Further reproduction prohibited without permission. www.manaraa.com

3.2 A non-axisymmetric Cauchy-Poisson problem

From this section, we will study several inviscid free-surface flow problems of significant practical interests using the spectral method developed earlier. First, we solve here a Cauchy-Poisson problem with a non-axisymmetric initial wave elevation (see Fig. 3.3a). This resembles the situation of waves, excited by a sudden disturbance, impinging on a circular structure. The initial wave form is taken to be the following:

$$\eta(r,\theta,t=0) = \exp\left\{-[r\cos\theta - (r_i + r_o)/2]^2 - [r\sin\theta]^2\right\}. \tag{3.15}$$

The dimensions of domain are chosen to be $r_o = 10$ and $d = 10$ while the time step $\Delta t = 0.1$. Grid resolution of $L \times M \times N = 72 \times 128 \times 24$ is used.

Because of the reflection of waves from the outer wall and their interference with the inner cylinder, the wave surface evolves in a complicated manner. Figs. 3.3 and 3.4 reveal some of these interaction features at 12 instants of time. The outward-moving "ring waves" of the pulse (Fig. 3.3c) first hit the outer cylinder and rebound, interestingly, almost as a plane wave system (Figs. 3.3e and f). The inward-moving ring waves are diffracted around the inner cylinder and eventually bounce off the far side of the outer cylinder to interact with the "plane waves" which somewhat encircle around the inner cylinder to reach the far side (Figs. 3.4a and b). When all these waves meet at the far end, they evolve into waves of much shorter lengths, moving at much lower spatial velocities (Figs. 3.4c to f). All these flow features are well captured by a radial grid dimension of merely 72 points.

The horizontal force F_x on the cylinder and overturning moment M_y are computed using Eqns. (2.8) and (2.9), and their time histories are shown is Fig. 3.5. It is interesting to notice that the maximum force does *not* occur during the initial wave impingement, but appears around $t = 65.0$, due to the wave "focusing effect" of the outer wall. This is confirmed by the wave perspective plot in Fig. 3.4b, where a large wave elevation is observed at the far side of the cylinder.

It is important to validate the accuracy of the solution. As a measure of the accuracy of this type of computation, we will demonstrate that the flow retains the same total energy as the initial wave pulse. We define the following energy quantities

Reproduced with permission of the copyright owner. Further reproduction prohibited without permission. www.manaraa.com

following Yeung (1982): the total energy (T.E.) in the fluid domain as the sum of its kinetic and potential parts

$$\begin{aligned} T.E.(t) &= K.E.(t) + P.E.(t) \\ &= \int_{\mathcal{S}\cup\mathcal{F}\cup\Sigma\cup\mathcal{B}} \frac{1}{2}\phi\phi_n dS + \int_{\mathcal{F}} \frac{1}{2}\eta^2 dS \\ &= \int_{\mathcal{F}} \frac{1}{2}\phi\phi_n dS + \int_{\mathcal{F}} \frac{1}{2}\eta^2 dS \end{aligned} \tag{3.16}$$

where the contributions to the first integral from $\mathcal{S}$, Σ and $\mathcal{B}$ vanish because $\phi_n = 0$. Clearly, in the absence of any energy source, T.E. must stay constant. Fig. 3.6 shows that the error in the total energy is no more than 0.2% of the the initial potential energy of the wave form even after 10,000 steps of simulation. Of course, by the principle of equal energy distribution, one observes that P.E. and K.E. each hovers around and converges to the value of 0.5. This confirms that the wave motion would never vanish completely, which is to be expected in the absence of viscosity.

3.3 Flow around a swaying cylinder: A radiation problem

In this section, we solve a wave radiation problem, in which the otherwise still fluid is disturbed by a body undergoing forced motion. Radiation problem and diffraction problem (to be discussed in Section 3.4) are key elements in the hydrodynamic theory of body motion in waves.

Consider a vertical cylinder of radius r_i' moving with periodic velocity $U'(t')$ along the x-axis, starting from $t' = 0$ in otherwise still water of depth d'. This is a well-known problem in hydrodynamics for which a closed form solution for the case of a laterally unbounded fluid can be obtained (Yeung, 1981). The hydrodynamic properties of the circular cylinder is characterized by force coefficients that are dependent on the frequency of the oscillation.

We choose to non-dimensionalize fluid quantities by body radius a', gravitational acceleration g' and fluid density ρ'. Specifically, we let non-dimensional velocity

Reproduced with permission of the copyright owner. Further reproduction prohibited without permission. www.manaraa.com

Computational Methods	$\omega\sqrt{r_i/g} = \pi/4$		$\omega\sqrt{r_i/g} = \pi/2$	
	$\mu_{xx}/\rho\pi r_i^2 d$	$\lambda_{xx}/\omega\rho\pi r_i^2 d$	$\nu_{xx}/\rho\pi r_i^2 d$	$\lambda_{xx}/\omega\rho\pi r_i^2 d$
Yeung (1981)	0.40159	0.45051	0.46771	0.04650
Present Method	0.41047	0.44689	0.47149	0.04198

Table 3.1: Comparison of added mass and damping coefficient computed by the present method and those in Yeung (1981).

$\mathbf{V}(t)$ on the right-hand side of Eqn. (2.4) be given by:

$$V(t) = \begin{cases} 0 & \text{when } t < 0 \\ a\omega \sin(\omega t) & \text{when } t \geq 0 \end{cases} \tag{3.17}$$

where a denotes the amplitude of the body motion, and ω the angular frequency. If a steady state solution is reached, the force can be simply expressed in terms of an added mass coefficient μ_{xx} and a damping coefficient λ_{xx} defined below (Wehausen and Laitone, 1960):

$$F_x(t) = -\mu_{xx}\frac{dU(t)}{dt} - \lambda_{xx}U(t) \tag{3.18}$$

The solution of this problem is sought by choosing $r_o = 30$ for two frequencies of oscillation $\omega = \pi/2$ and $\pi/4$. Here the frequency of oscillation is non-dimensionalized by $\sqrt{g'/r_i'}$. Fig. 3.7 shows the free-surface elevation for a complete cycle of body motion at one-quarter period intervals for $a = 0.055$ and $\omega = \pi/2$ after the body has oscillated for 9 periods. The hydrodynamic force acting on the cylinder for this case is shown in Fig. 3.8 as a function of time. It is evident that a harmonic steady state is reached after the body has undergone only 2 or 3 periods.

From the force time history, it is possible to evaluate the added-mass and damping coefficients and compare them with known analytical results (Yeung, 1981). Table 1 shows such a comparison for a grid density of $L = 150$, $M = 48$, and $N = 24$, when solved as a transient three-dimensional problem. The agreement is seen to be excellent since no symmetry assumptions are made. The envelope of the force curve in Fig. 3.8 confirms the method has excellent stability characteristics.

Reproduced with permission of the copyright owner. Further reproduction prohibited without permission. www.manaraa.com

3.4 Cylinder in progressive wave: A second-order diffraction problem

In this section, we study a wave diffraction problem, which concerns the flow around a body held stationary in incoming waves. When the free-surface boundary conditions are linearized, the wave diffraction by a vertical cylinder was first solved by Havelock (1940) for infinite water depth, and extended by McCamy and Fuch (1954) to the case of finite water depth. Development of the tension leg platforms aroused the interest for the second-order wave diffraction theory. The so-called "springing" loads predicted by such theory are important for the fatigue life of marine structures. After the pioneering works of Lighthill (1979) and Molin (1979), second-order diffraction loads on vertical cylinders were given by Molin and Marion (1986).

Consider a vertical cylinder of radius r_i' and depth of d' standing in a progressive plane wave system of frequency ω' and amplitude A'. Again, we choose to non-dimensionalize fluid quantities by cylinder radius r_i', gravitational acceleration g' and fluid density ρ'.

Under the assumption of incompressible fluid and irrotational flow, the first order and second order potentials, $\phi^{(1)}$ and $\phi^{(1)}$, both satisfy the Laplace equation:

$$\nabla^2\phi^{(1)} = 0, \tag{3.19}$$

and

$$\nabla^2\phi^{(2)} = 0. \tag{3.20}$$

Assuming moderate wave heights, we derive free-surface conditions in Appendix D as:

$O(\epsilon)$:

$$\eta_t^{(1)} - \phi_z^{(1)} = 0, \tag{3.21}$$

$$\eta^{(1)} + \phi_t^{(1)} = 0; \tag{3.22}$$

$O(\epsilon^2)$:

$$\eta_t^{(2)} - \phi_z^{(2)} = -\eta_r^{(1)}\phi_r^{(1)} - \frac{1}{r^2}\eta_\theta^{(1)}\phi_\theta^{(1)} + \eta^{(1)}\phi_{zz}^{(1)} \equiv K^{(2)}, \tag{3.23}$$

Reproduced with permission of the copyright owner. Further reproduction prohibited without permission. www.manaraa.com

$$\eta^{(2)} + \phi_t^{(2)} = -\eta^{(1)}\phi_{tz}^{(1)} - \frac{1}{2}\left[\phi_r^{(1)^2} + \frac{1}{r^2}\phi_\theta^{(1)^2} + \phi_z^{(1)^2}\right] \equiv D^{(2)}. \qquad (3.24)$$

Following Chapter 2, we may derive mixed boundary conditions for $\phi^{(1)}$ and $\phi^{(2)}$, similar to Eqn. (2.40):

$$\phi^{(1)^{k+1}} + (\frac{\Delta t}{2})^2 \phi^{(1)^{k+1}}_z = \phi^{(1)^k} - \Delta t \eta^{(1)^k} - (\frac{\Delta t}{2})^2 \phi^{(1)^k}_z, \qquad (3.25)$$

$$\phi^{(2)^{k+1}} + (\frac{\Delta t}{2})^2 \phi^{(2)^{k+1}}_z = \left[\phi^{(2)^k} - \Delta t \eta^{(2)^k} - (\frac{\Delta t}{2})^2 \phi^{(2)^k}_z\right] + (\frac{\Delta t}{2})\left[(D^{k+1} + D^k) - (\frac{\Delta t}{2})(K^{k+1} + K^k)\right], \qquad (3.26)$$

where k again denotes time step.

The incident wave system in this case is a second-order Stokes wave train, which is specified on the outer boundary $r = r_o$ using its velocity potentials (see Mei, 1989),

$$\begin{aligned} \phi^{(1)} &= \frac{A\omega}{k}\frac{\cosh k(z+d)}{\sinh kd}\sin(kx - \omega t), \qquad \text{at } x = r_o\cos\theta, \\ \phi^{(2)} &= \frac{3A^2\omega}{8}\frac{\cosh 2k(z+d)}{\sinh^4 kd}\sin 2(kx - \omega t), \qquad \text{at } x = r_o\cos\theta. \end{aligned} \qquad (3.27)$$

To solve this second-order diffraction problem as a time dependent problem, we also need to specify potentials and their vertical derivatives on the free surface as initial conditions

$$\begin{aligned} \phi^{(1)}(r,\theta,0,0) &= \frac{A\omega}{k}\frac{\cosh kd}{\sinh kd}\sin kx, \\ \phi_z^{(1)}(r,\theta,0,0) &= A\omega\sin kx, \\ \phi^{(2)}(r,\theta,0,0) &= \frac{3A^2\omega}{8}\frac{\cosh 2kd}{\sinh^4 kd}\sin 2kx, \\ \phi_z^{(2)}(r,\theta,0,0) &= \frac{3A^2\omega k}{4}\frac{\sinh 2kd}{\sinh^4 kd}\sin 2kx. \end{aligned} \qquad (3.28)$$

These initial conditions in Eqn. (3.28) are consistent with boundary conditions given in Eqn. (3.27); both correspond to a regular second-order Stokes wave train in the $x-$direction.

The wave diffraction for both solutions are obtained by imposing the no-leak body conditions. However, numerical tests show that if these body conditions were

Reproduced with permission of the copyright owner. Further reproduction prohibited without permission. www.manaraa.com

abruptly imposed at $t = 0$, a splash would occur near the body surface and plague the numerical solution. In order to avoid this difficulty, we use the following Neumann conditions, which correspond to a *gradual* imposition of the body surface in the wave field:

$$\phi_r^{(1)} = f(t)A\omega\frac{\cosh k(z+d)}{\sinh kd}\cos(kx-\omega t)\cos\theta, \qquad \text{at } x = r_i\cos\theta,$$
$$\phi_r^{(2)} = f(t)\frac{3A^2\omega k}{4}\frac{\cosh 2k(z+d)}{\sinh^4 kd}\cos 2(kx-\omega t)\cos\theta, \quad \text{at } x = r_i\cos\theta, \tag{3.29}$$

where $f(t)$ is defined by

$$f(t) = \begin{cases} \frac{1}{2}\left[1+\cos\left(\frac{\pi t}{T_m}\right)\right] & \text{when } t < T_m \\ 0 & \text{when } t \geq T_m \end{cases} \tag{3.30}$$

with T_m being a modulation time.

After the velocity potentials $\phi^{(1)}$ and $\phi^{(2)}$ are solved, the $x-$forces acting on the body can be computed using the Bernoulli equation (Molin, 1979). The final expressions for non-dimensional first-order force F_{1x} and second-order force F_{2x} are given as

$$F_{1x} = \int_S -\phi^{(1)}{}_t n_x dS, \tag{3.31}$$

and

$$F_{2x} = F_{2x}^{(1)} + F_{2x}^{(2)}, \tag{3.32}$$

where $F_{2x}^{(1)}$ depends on $\phi^{(1)}$,

$$F_{2x}^{(1)} = \int_S -\frac{1}{2}(\nabla\phi^{(1)})^2 n_x dS + \int_\Gamma \frac{1}{2}(\phi^{(1)}{}_t)^2 n_x d\Gamma, \tag{3.33}$$

while

$$F_{2x}^{(2)} = \int_S -\phi^{(2)}{}_t n_x dS \tag{3.34}$$

depends on $\phi^{(2)}$. Here $\mathcal{S}$ denotes the mean wetted body surface, and Γ the intersection of $\mathcal{S}$ at $z = 0$.

3.4.1 A test case

Before proceeding to the wave diffraction problem, we choose to check the procedure presented above by a test problem, in which the inner cylinder is assumed

Reproduced with permission of the copyright owner. Further reproduction prohibited without permission. www.manaraa.com

to be a perfectly permeable surface, instead of a solid one. To do that, we hold $f(t)$ in Eqn. (3.29) to be unity at all time. Eqn. (3.27) is imposed as a boundary condition on the outer boundary, and initial conditions in Eqn. (3.28) are used on free surface. It is expected that, in this test case, a second-order Stokes wave as given in Eqn. (3.27) should propagate through the domain without being disturbed.

For this test, we choose the domain sizes to be $r_o = 11$ and $d = 2$. The wave amplitude A is taken to be 0.3, and wave number k is set to be 1.0, which corresponds to a wave period of $T = 6.39934$. Grid resolution of $L \times M \times N = 96 \times 64 \times 16$ and a time step of $\Delta t = 0.1$ are used. The numerical results are presented in Fig. 3.9, which shows the propagation of the first and second-order waves along the $x-$axis for $t = 0$ to 2.4. The results between $x = -1$ and 1 are wave elevations on the cylinder surface projected into the vertical plane of symmetry $y = 0$. No wave modulation is visible from the plot. A further look at the numerical date confirms that the maximum difference of total wave elevation (up to 2nd order) is less than 0.1% in first five wave periods.

3.4.2 Diffraction about a cylinder

Numerical results presented here are obtained by a mesh size of $L \times M \times N = 72 \times 128 \times 16$, and a time step $\Delta t = 0.05$ is used. The dimensions of the computational domain are set to be $r_o = 16$ and $d = 2$. The incident wave is a second-order Stokes wave train with $A = 0.3$ and $k = 1.0$, which again corresponds to a wave period of $T = 6.39934$. The modulation time T_m in Eqn. (3.30) is set equal to wave period T.

Free-surface elevations and runups

Fig. 3.10 shows a perspective view of free-surface elevation to second order at a large time $t = 32.00$. Complex wave patterns are observed near the cylinder. Fig. 3.11 presents the development of the wave profiles and wave runup with time to first and second orders. The wave profiles in the vertical plane of symmetry $y = 0$ are shown on both upstream side ($x < -1$) and downstream side ($x > 1$) of the cylinder while the wave runup on half of the cylinder surface ($-\pi < \theta < \pi$) are plotted between

Reproduced with permission of the copyright owner. Further reproduction prohibited without permission. www.manaraa.com

$-1 < x < 1$. The flow immediately adjacent to the cylinder appears to repeat itself soon after the first cycle, while the flow further away from the cylinder takes longer time to reach a steady state. The scattered waves of first and second orders propagate steadily away from the cylinder at their corresponding group velocities. It is also observed from Fig. 3.11 that the second-order effects contribute significantly to the total wave runup on the cylinder .

Velocity vectors

Figs. 3.12 to 3.14 show velocity vectors in the vertical plane of symmetry for six instants of time. Specifically, Fig. 3.12 corresponds the initial modulation period ($t \leq T_m$), and Figs. 3.13 and 3.14 correspond to four instants of time during a steady state. The velocity vectors near the cylinder clearly indicate that the no-leak boundary condition is satisfied in all cases except in Fig. 3.12a, where the cylinder has a permeability of 0.5. During the steady state (Figs. 3.13 and 3.14), velocity fields to first and second orders differ substantially, especially on the downstream side of the cylinder.

Wave forces

The second-order horizontal ($x-$ direction) forces on the cylinder are computed using Eqns. (3.31) to (3.34). The time history of these forces are plotted in Fig. 3.15. It is evident from this plot that a harmonic state has been reached. In this case, the maximum horizontal force based on the second-order theory is about 6% larger than that predicted by the linear theory. The second-order component $F_{2x}^{(1)}$ has a non-zero mean value, representing a drift force.

Reproduced with permission of the copyright owner. Further reproduction prohibited without permission. www.manaraa.com

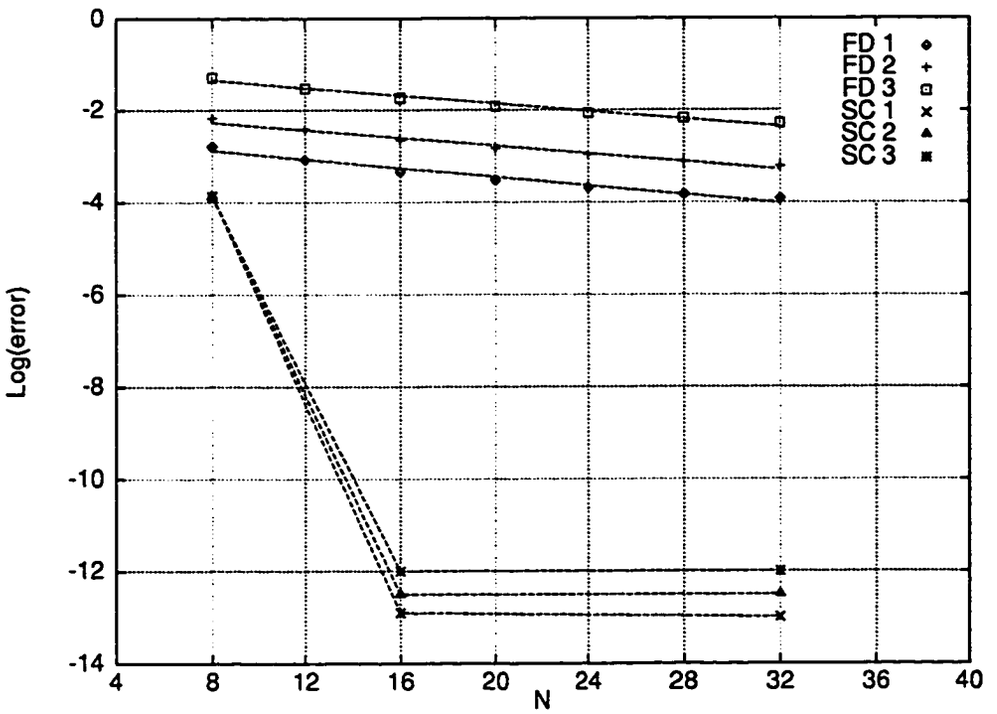

Figure 3.1: Logarithmic maximum pointwise errors vs. grid resolution for various boundary conditions (FD: Finite difference method; SC: Spectral collocation method. Case 1: Dirichlet Conditions on R and Z directions; Case 2: Neumann Conditions on R and Dirichlet on Z; Case 3: Mixed Conditions on R and Z).

Reproduced with permission of the copyright owner. Further reproduction prohibited without permission. www.manaraa.com

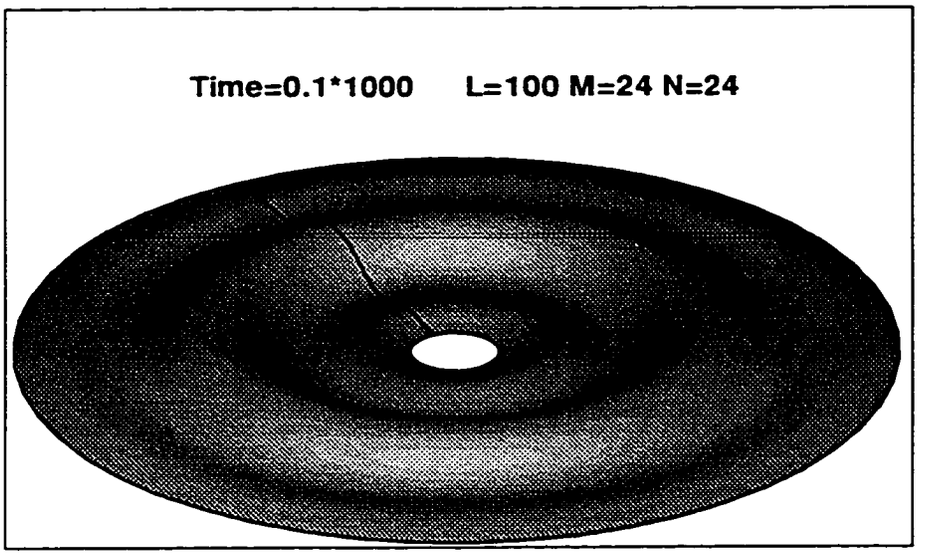

(a)

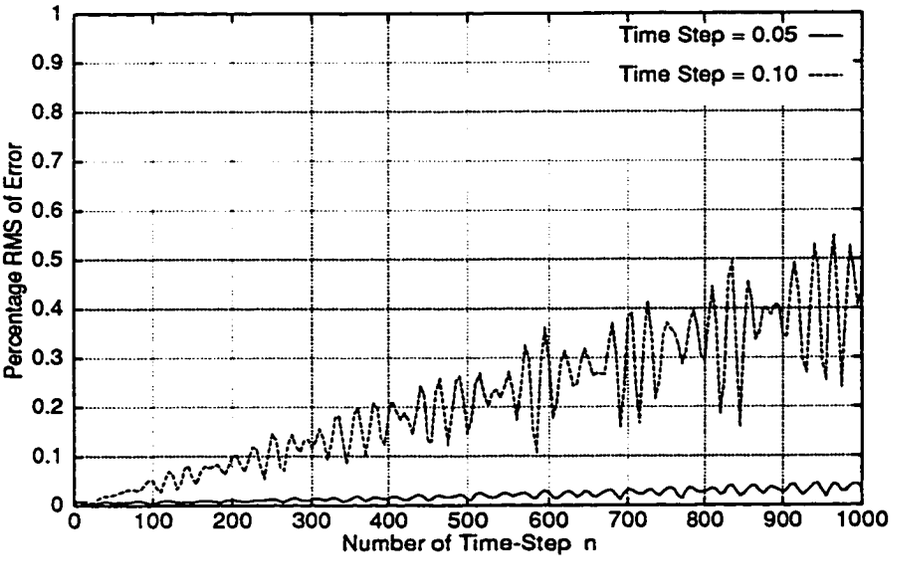

(b)

Figure 3.2: Free-surface elevation at $t = 100.0$ (top) and the root mean square of errors of free-surface elevation as a function of time-steps (bottom) in the axisymmetric Cauchy-Poisson wave problem.

Reproduced with permission of the copyright owner. Further reproduction prohibited without permission. www.manaraa.com

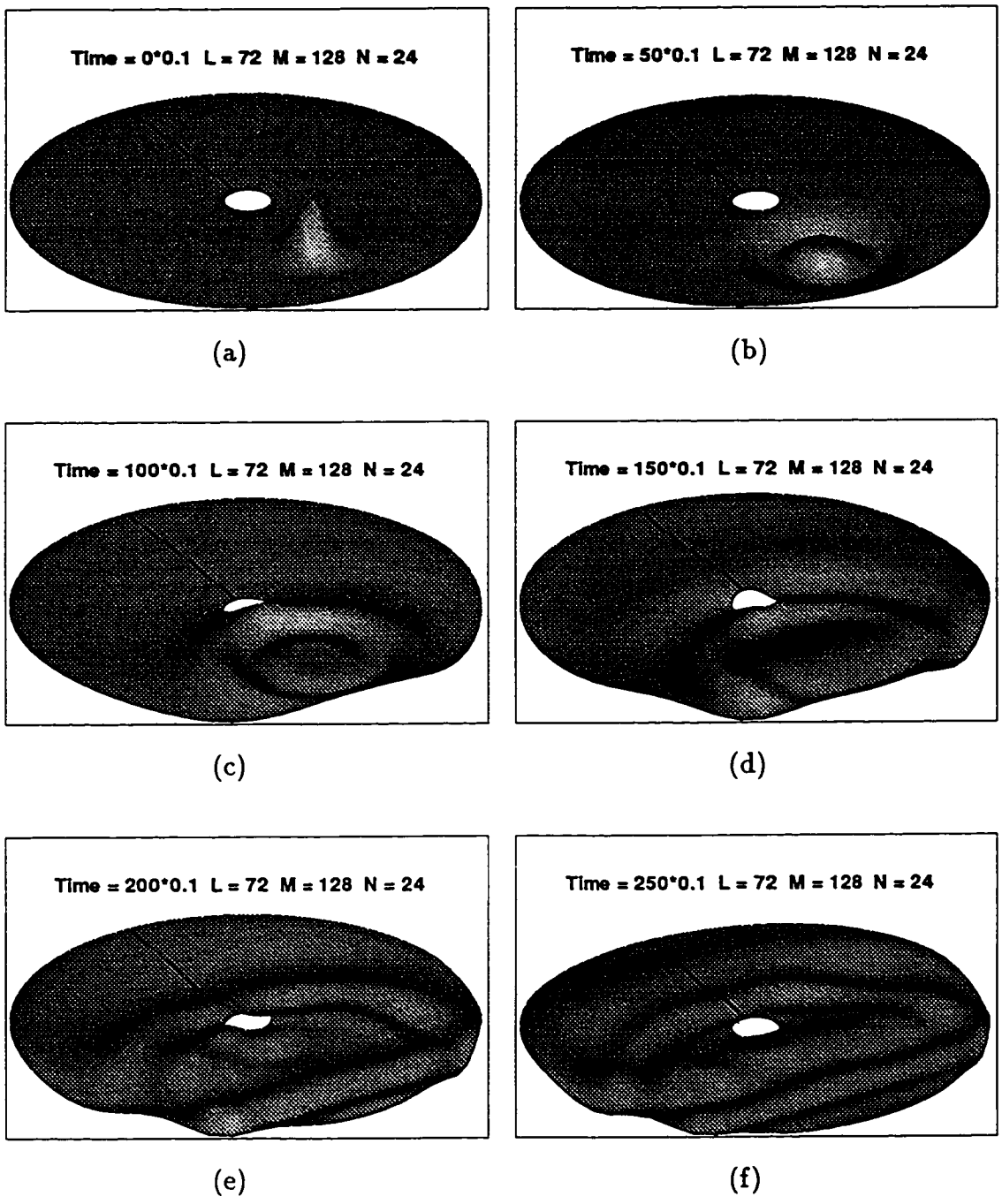

Figure 3.3: Instantaneous free-surface elevation plots for the Cauchy-Poisson wave problem, L, M, N representing resolution in the radial, circumferential, and vertical directions.

Reproduced with permission of the copyright owner. Further reproduction prohibited without permission. www.manaraa.com

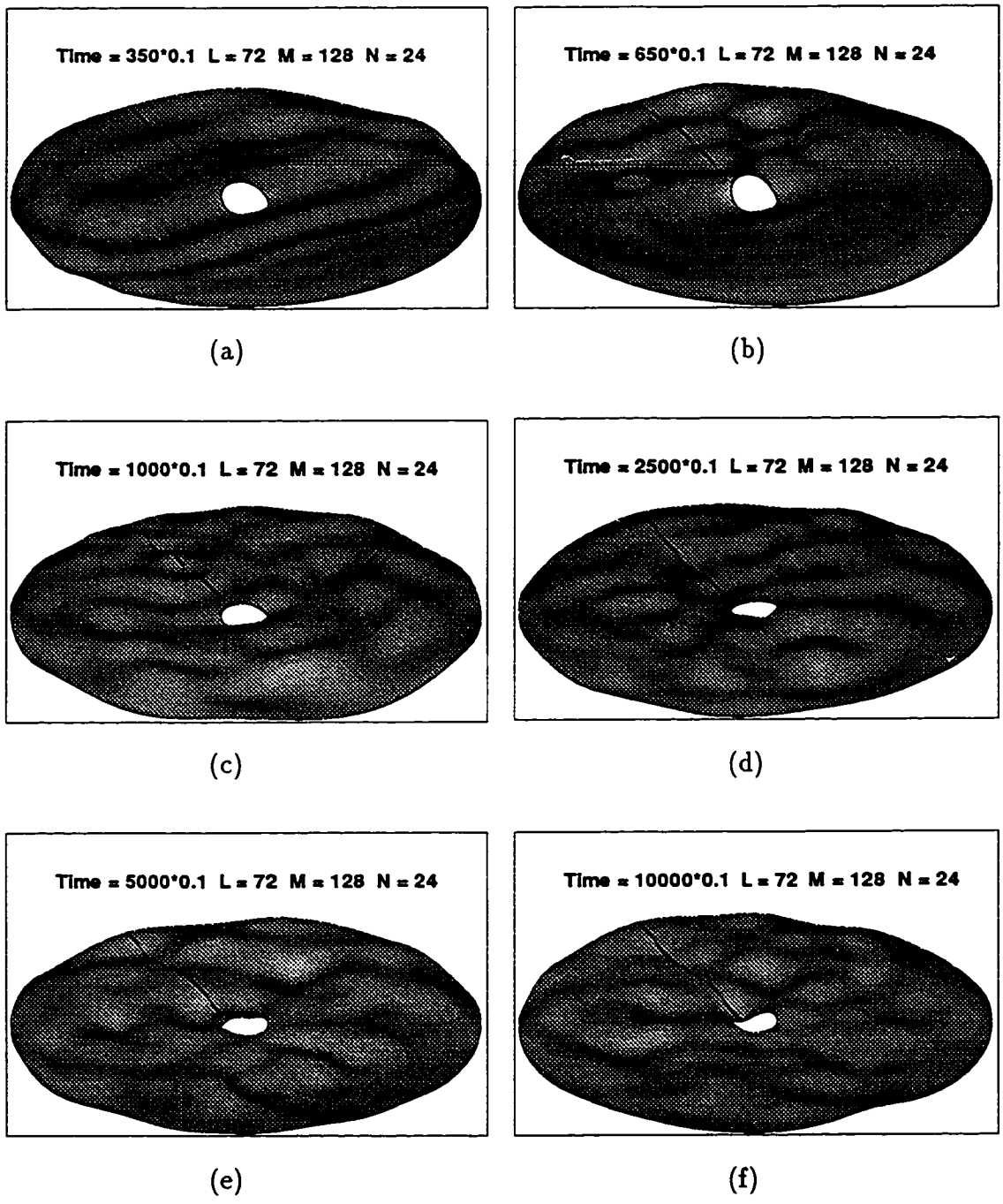

Figure 3.4: Instantaneous free-surface elevation plots for the Cauchy-Poisson wave problem, L, M, N representing resolution in the radial, circumferential, and vertical directions.

Reproduced with permission of the copyright owner. Further reproduction prohibited without permission. www.manaraa.com

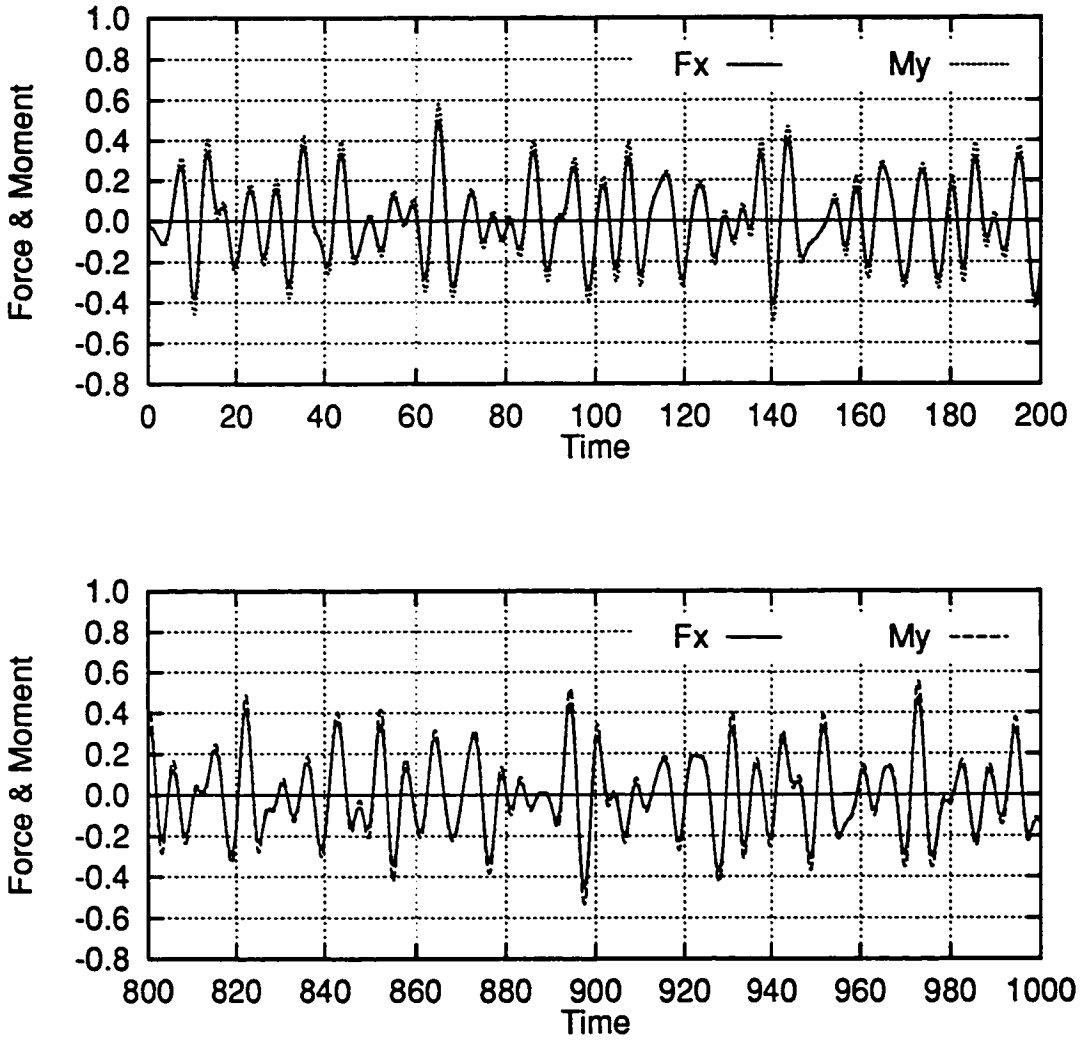

Figure 3.5: Horizontal force and overturning moment on the cylinder.

Reproduced with permission of the copyright owner. Further reproduction prohibited without permission. www.manaraa.com

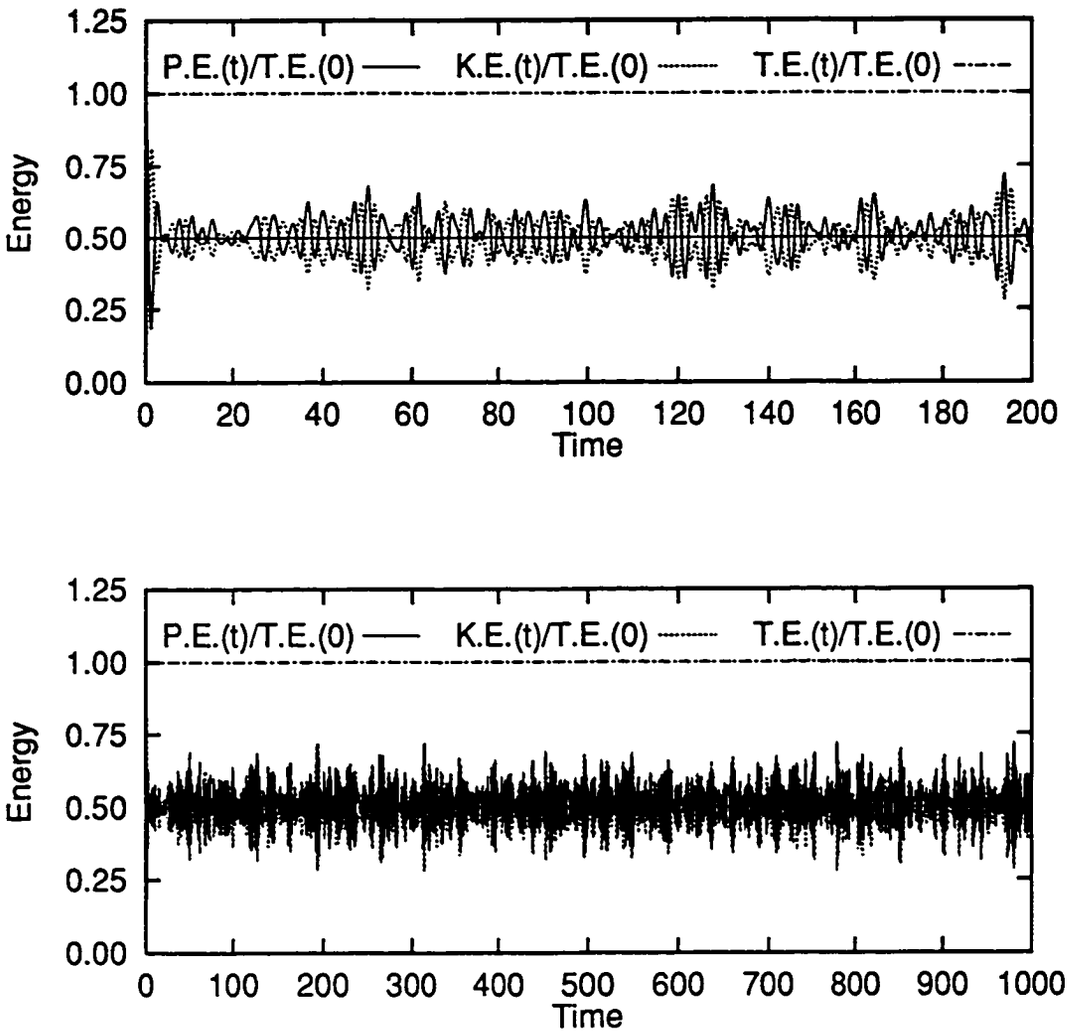

Figure 3.6: Energy balance in the Cauchy-Poisson wave problem.

Reproduced with permission of the copyright owner. Further reproduction prohibited without permission. www.manaraa.com

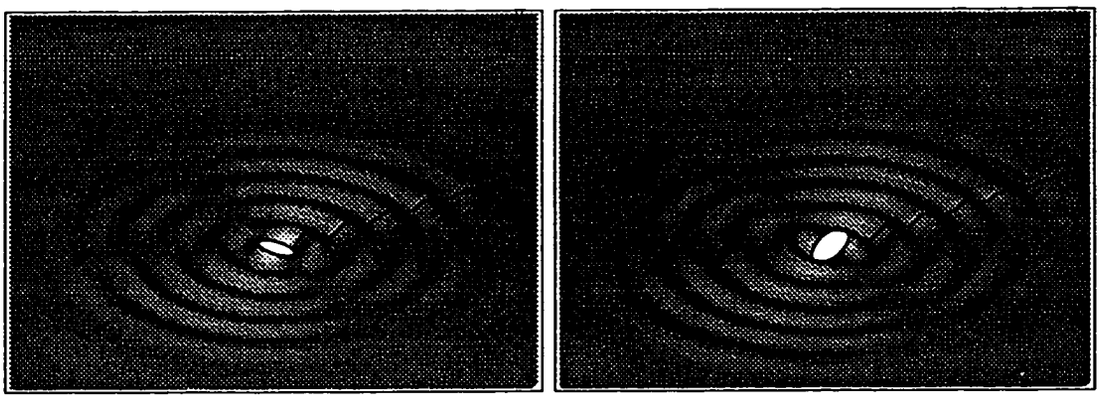

(a) (b)

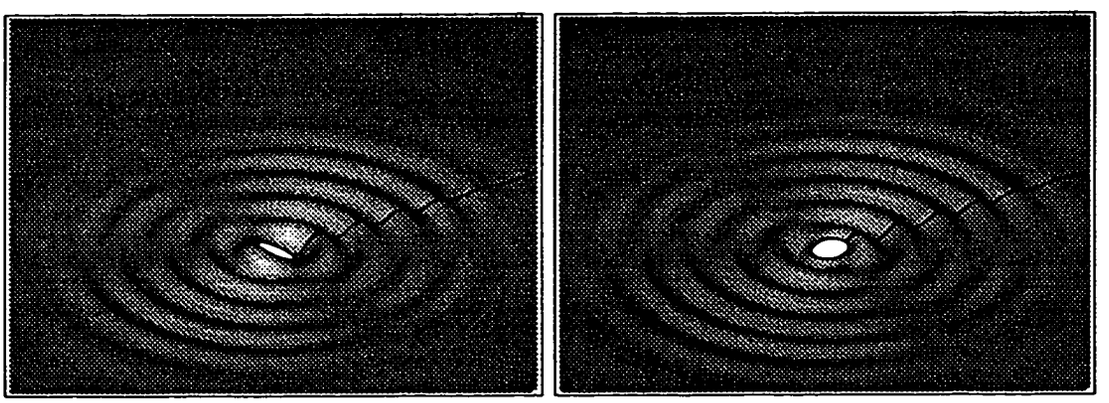

(c) (d)

Figure 3.7: Instantaneous free-surface elevation plots for the swaying cylinder problem in one cycle of motion with $\omega = \pi/2$, and $t = 32.5, 35.0, 37.5$ and 40.0.

Reproduced with permission of the copyright owner. Further reproduction prohibited without permission. www.manaraa.com

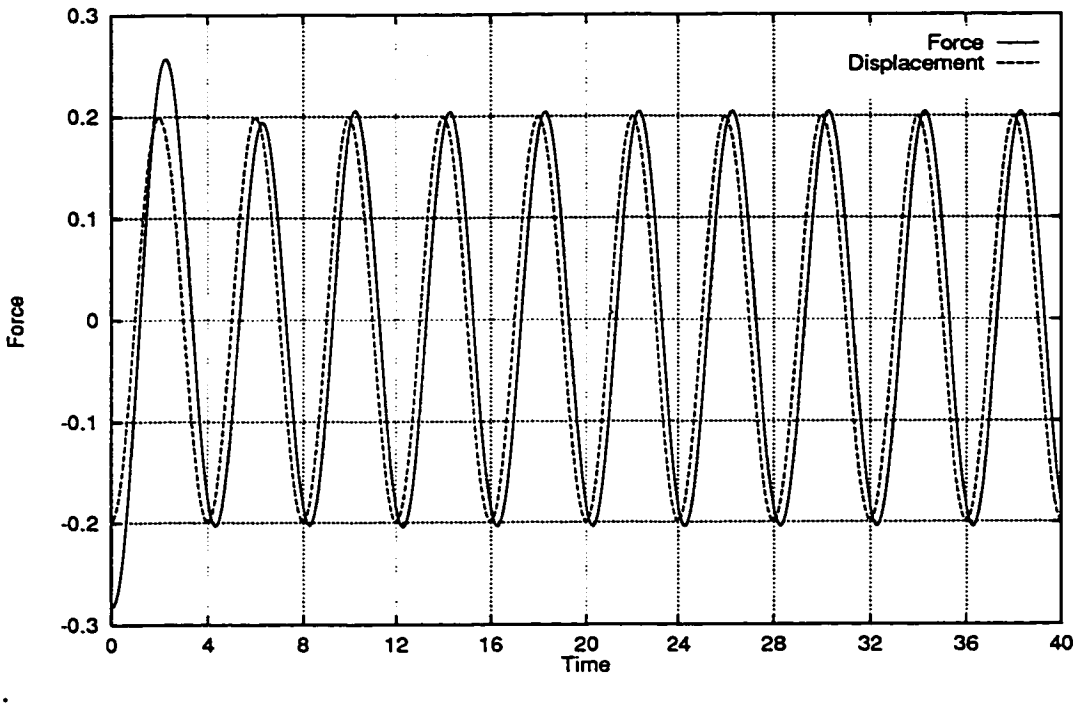

Figure 3.8: Horizontal force on the cylinder as a function of time.

Reproduced with permission of the copyright owner. Further reproduction prohibited without permission. www.manaraa.com

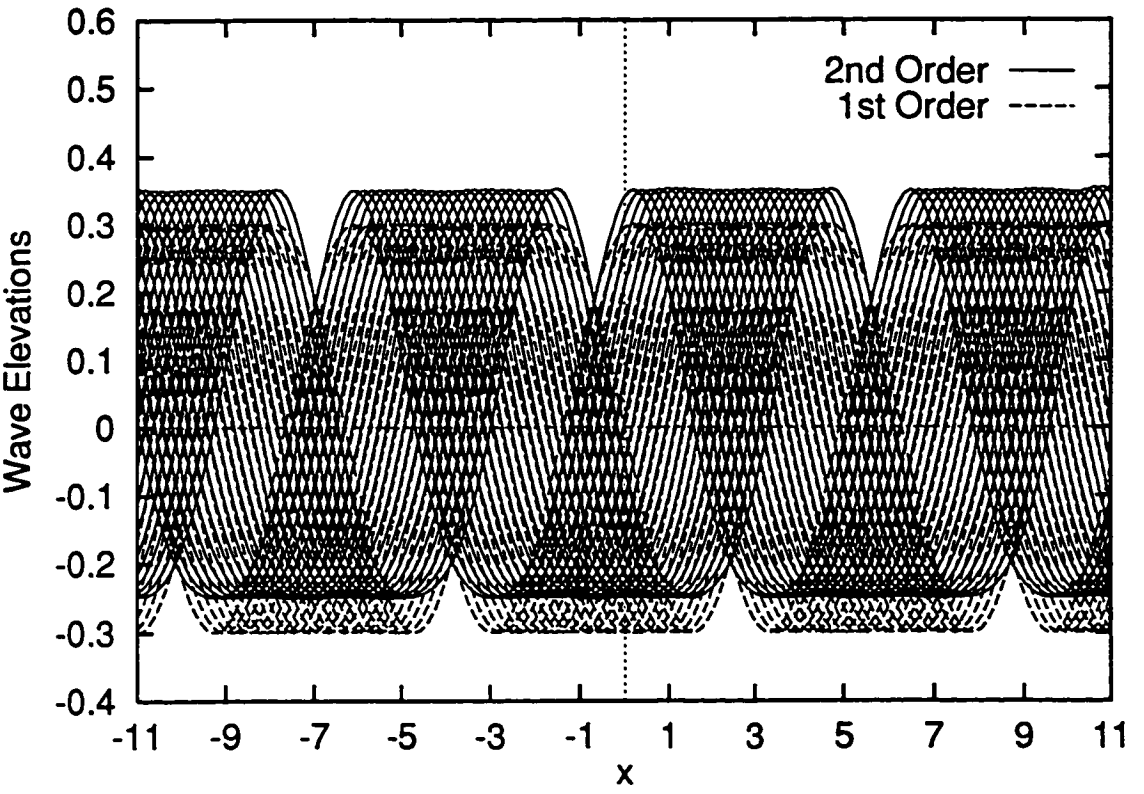

Figure 3.9: Wave elevations in the vertical plane of symmetry for the test case. Time $t = 0(0.1)2.4$

Reproduced with permission of the copyright owner. Further reproduction prohibited without permission. www.manaraa.com

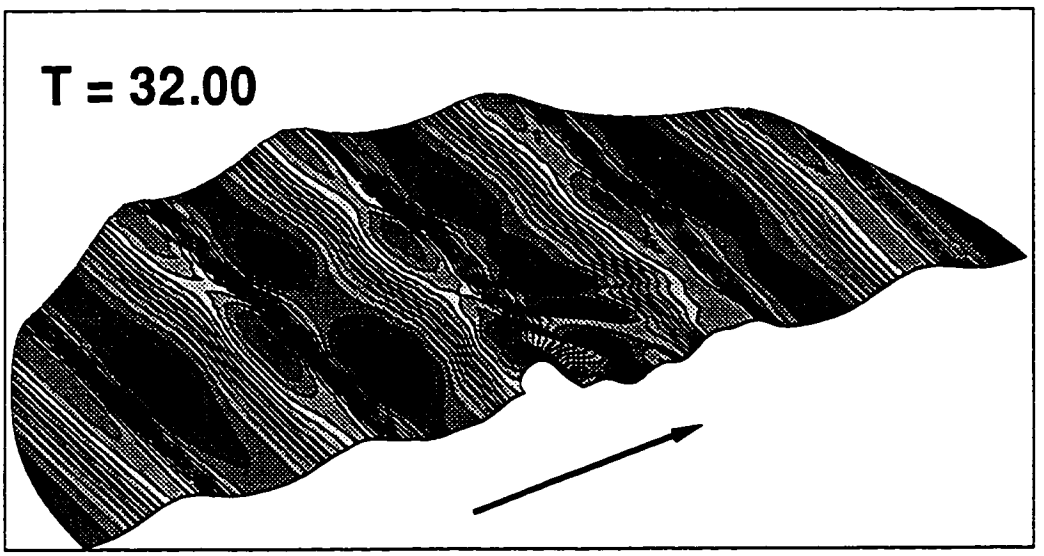

Figure 3.10: Fully developed wave field to second order at $t = 32.00$ for the second-order wave diffraction problem. Arrow represents direction of wave propagation.

Reproduced with permission of the copyright owner. Further reproduction prohibited without permission. www.manaraa.com

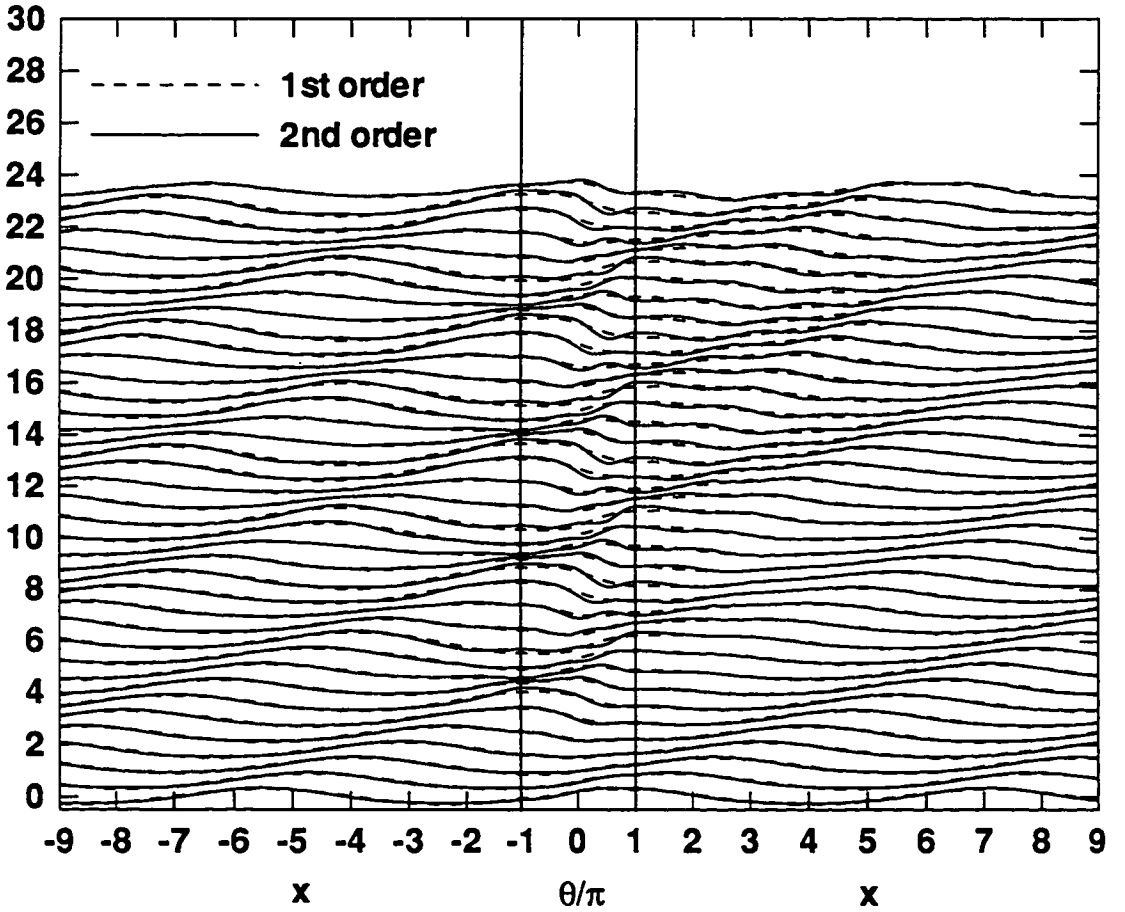

Figure 3.11: Time history of wave elevations (to first and second orders) in plane $y = 0$ ($x < -1$ and $x > 1$) and time history of wave runups (again to first and second orders) on the cylinder ($-1 < \theta/\pi < 1$). Time $t = 0(0.80)32.00$.

Reproduced with permission of the copyright owner. Further reproduction prohibited without permission. www.manaraa.com

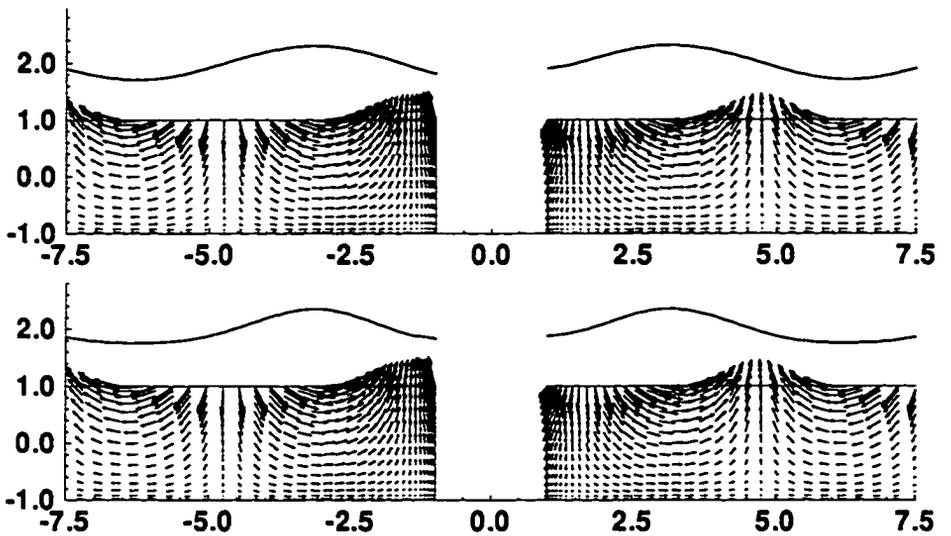

(a)

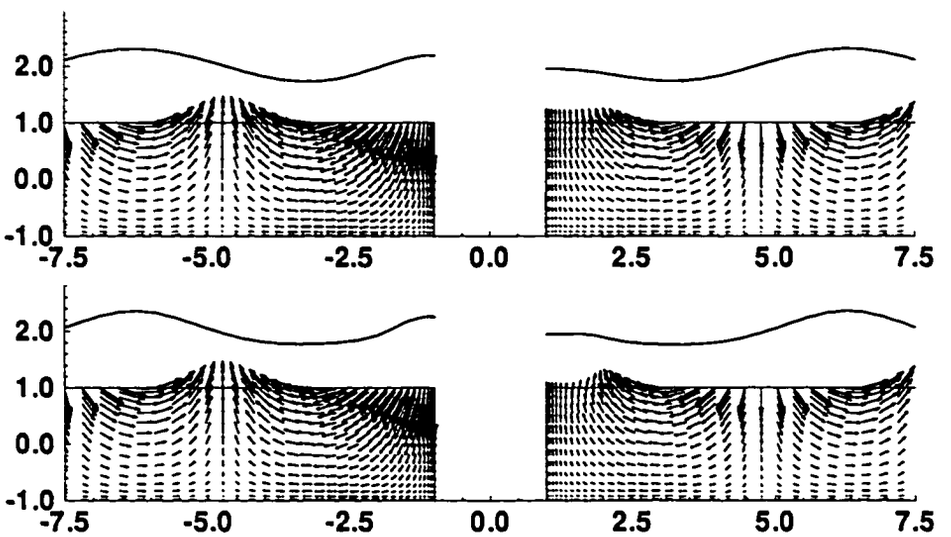

(b)

Figure 3.12: Velocity Vectors and free-surface elevations in the vertical plane of symmetry during modulation ($t \leq T_m$). Top: solution to first order; bottom: solution to second order. (a) Permeability $f(t) = 0.5$ at $t = T_m/2$; (b) Permeability $f(t) = 0$ at $t = T_m$.

Reproduced with permission of the copyright owner. Further reproduction prohibited without permission. www.manaraa.com

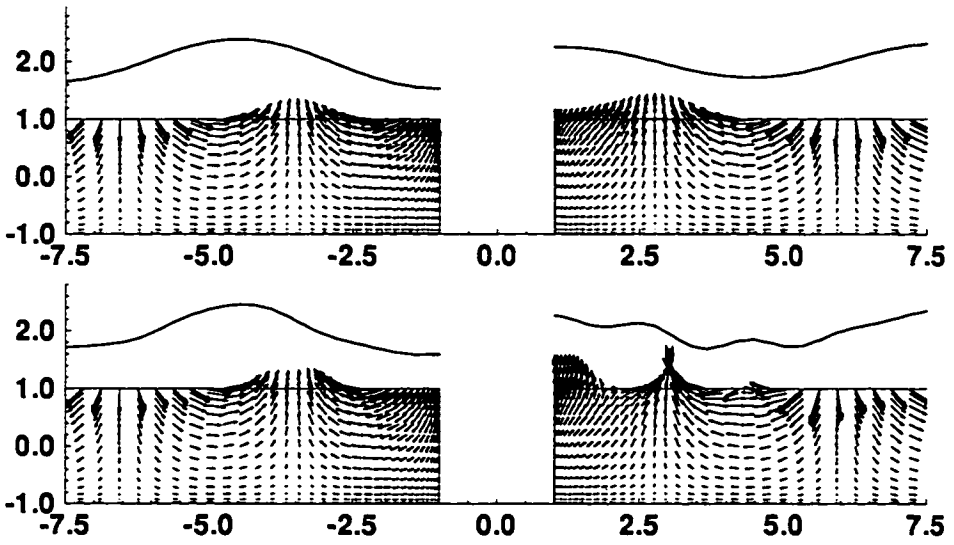

(a)

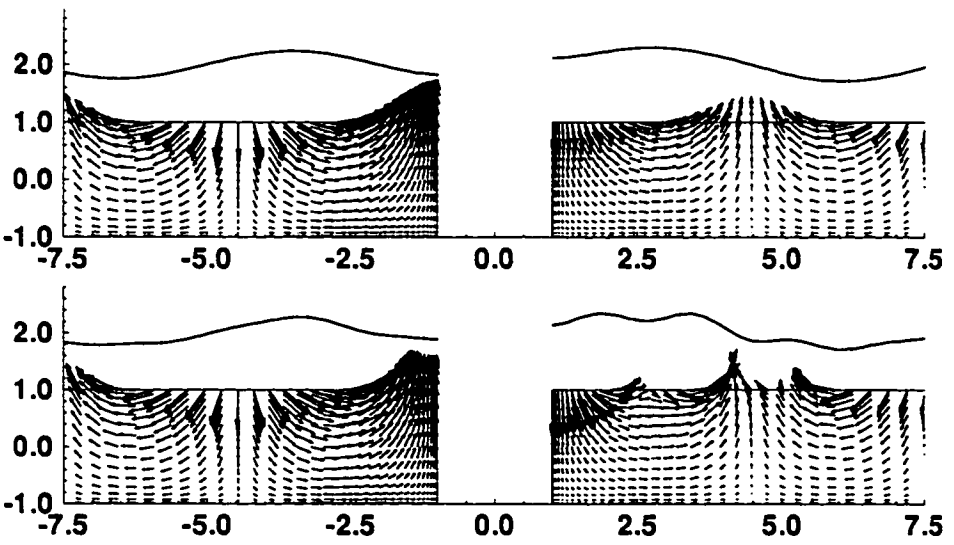

(b)

Figure 3.13: Velocity Vectors and free-surface elevations in the vertical plane of symmetry during steady state. Top: solution to first order; bottom: solution to second order. (a) Time $t = 27.20$; (b) Time $t = 28.80$.

Reproduced with permission of the copyright owner. Further reproduction prohibited without permission. www.manaraa.com

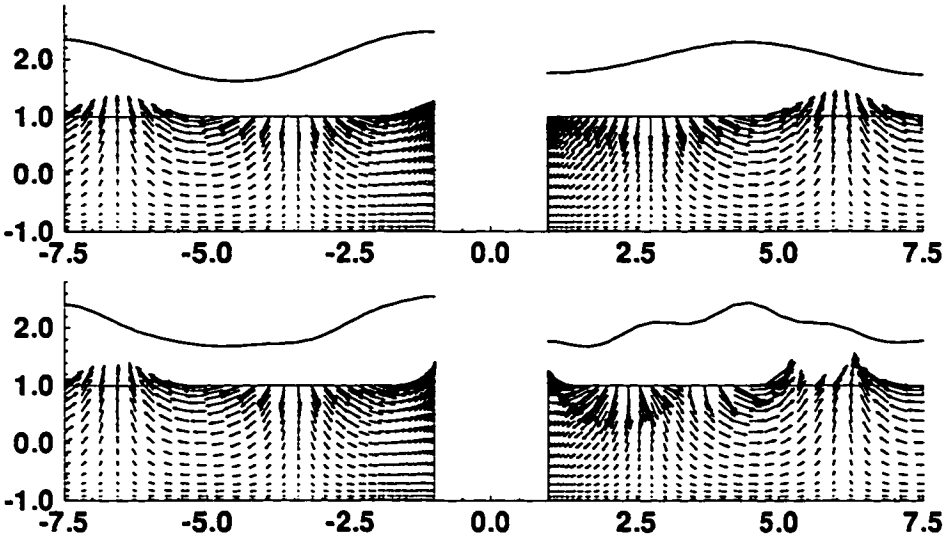

(a)

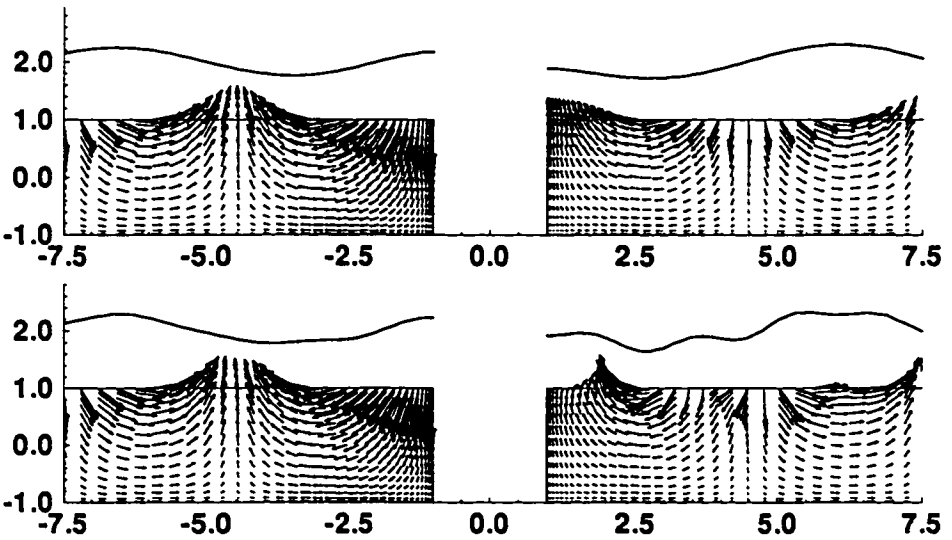

(b)

Figure 3.14: Velocity Vectors and free-surface elevations in the vertical plane of symmetry during steady state. Top: solution to first order; bottom: solution to second order. (a) Time $t = 30.40$; (b) Time $t = 32.00$.

Reproduced with permission of the copyright owner. Further reproduction prohibited without permission. www.manaraa.com

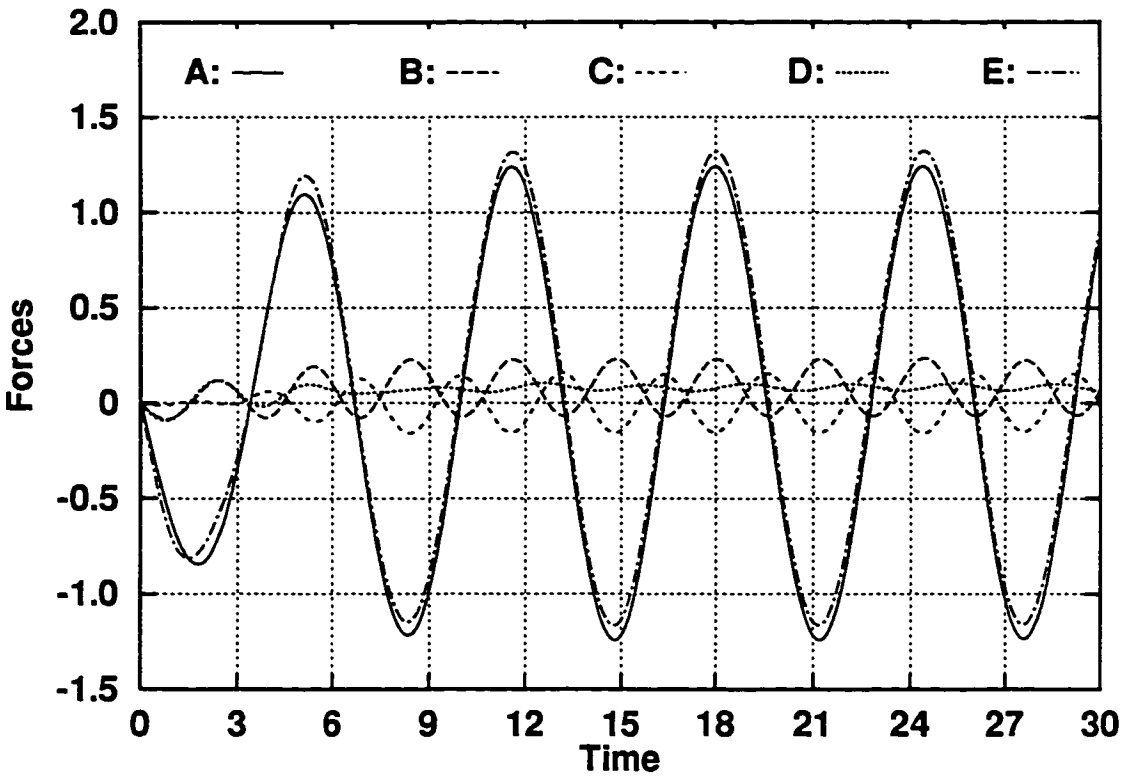

Figure 3.15: Time history of first and second-order horizontal forces on the cylinder. A: F_{1x}; B: $F_{2x}^{(1)}$; C: $F_{2x}^{(2)}$; D: $F_{2x} = F_{2x}^{(1)} + F_{2x}^{(2)}$; E: $F_{1x} + F_{2x}$.

Reproduced with permission of the copyright owner. Further reproduction prohibited without permission. www.manaraa.com

Chapter 4

Spectral method for a viscous fluid

The theoretical background for solving transient three-dimensional free-surface *viscous* flow will be described in this chapter. Following the format in Chapter 2, we will present its mathematical formulation first, and describe numerical treatment the second.

4.1 Problem formulation

4.1.1 Field equations

Consider the same cylindrical coordinate system (r, θ, z) described in Chapter 2 (see Fig. 2.1). If again we take U' as a characteristic velocity, r_i' as a characteristic length, the non-dimensional Navier-Stokes equations for incompressible viscous flow in cylindrical coordinates can be written as

$$\frac{\partial u}{\partial t} + u\frac{\partial u}{\partial r} + \frac{v}{r}\frac{\partial u}{\partial \theta} + w\frac{\partial u}{\partial z} - \frac{v^2}{r} = \frac{1}{Re}\left[\nabla^2 u - \frac{u}{r^2} - \frac{2}{r^2}\frac{\partial v}{\partial \theta}\right] - \frac{\partial P}{\partial r},$$

$$\frac{\partial v}{\partial t} + u\frac{\partial v}{\partial r} + \frac{v}{r}\frac{\partial v}{\partial \theta} + w\frac{\partial v}{\partial z} - \frac{uv}{r} = \frac{1}{Re}\left[\nabla^2 v - \frac{v}{r^2} - \frac{2}{r^2}\frac{\partial u}{\partial \theta}\right] - \frac{1}{r}\frac{\partial P}{\partial \theta},$$

$$\frac{\partial w}{\partial t} + u\frac{\partial w}{\partial r} + \frac{v}{r}\frac{\partial w}{\partial \theta} + w\frac{\partial w}{\partial z} = \frac{1}{Re}\left[\nabla^2 w\right] - \frac{\partial P}{\partial z}. \tag{4.1}$$

Reproduced with permission of the copyright owner. Further reproduction prohibited without permission. www.manaraa.com

Here, u, v and w are velocity components in the radial r, circumferential θ, and vertical z directions, respectively, and Re is a Reynolds number defined by $U'r_i'/\nu'$ with ν' being kinematic viscosity. $\nabla^2 = \frac{\partial^2}{\partial r^2} + \frac{1}{r}\frac{\partial}{\partial r} + \frac{1}{r^2}\frac{\partial^2}{\partial \theta^2} + \frac{\partial^2}{\partial z^2}$ in Eqn. (4.1) is the Laplacian operator in cylindrical coordinates. Eqn. (4.1) is complemented by the continuity equation

$$\frac{1}{r}\frac{\partial (ru)}{\partial r} + \frac{1}{r}\frac{\partial v}{\partial \theta} + \frac{\partial w}{\partial z} = 0. \tag{4.2}$$

The quantity P represents the non-dimensional dynamic pressure, which is related to the total pressure p by

$$P = p + \frac{z}{F_r^2}, \tag{4.3}$$

where F_r is a Froude number defined by $U'/\sqrt{g'r_i'}$. Here P and p are both non-dimensionalized by $\rho' U'^2$ with ρ being the density of fluid.

4.1.2 Boundary conditions

Next, the boundary conditions that govern the viscous-wave problem are defined:

On the body $\mathcal{S}$, the following no-slip conditions are used:

$$u = 0, \quad v = 0, \quad w = 0, \qquad \text{at } r = r_i. \tag{4.4}$$

On the free surface $\mathcal{F}$, the boundary conditions can be linearized from the exact kinematic and stress-continuity relations (see e.g., Wehausen and Laitone, 1960). The linearized dynamic boundary conditions are

$$\begin{aligned} \frac{\partial u}{\partial z} + \frac{\partial w}{\partial r} &= 0, \\ -P + \frac{\eta}{F_r^2} + \frac{2}{Re}\frac{\partial w}{\partial z} &= 0, \qquad \text{at } z = 0, \\ \frac{\partial v}{\partial z} + \frac{1}{r}\frac{\partial w}{\partial \theta} &= 0. \end{aligned} \tag{4.5}$$

They provide the appropriate boundary conditions for velocities and pressure. The kinematic condition is

$$\frac{\partial \eta}{\partial t} = w, \qquad \text{at } z = 0, \tag{4.6}$$

Reproduced with permission of the copyright owner. Further reproduction prohibited without permission. www.manaraa.com

which determines the free-surface elevation η. Note the boundary conditions in Eqns. (4.5) and (4.6) are satisfied on the mean free-surface $z = 0$, in order to be consistent with the linearization procedure.

It is worthwhile to point out that the general free-surface boundary conditions in Eqns. (4.5) and (4.6) can be simplified if one considers the Froude number to be sufficiently low so that $Fr^2/Re \ll 1$ or $U' \ll r_i'^2 g'/\nu'$. This assumption yields the so called "free-slip boundary condition"

$$\frac{\partial u}{\partial z} = 0, \quad \frac{\partial v}{\partial z} = 0, \quad w = 0, \qquad \text{at } z = 0. \tag{4.7}$$

Physically, this represents a flow symmetry of the velocity field about $z = 0$, with no shear stress and no wave elevation at $z = 0$.

On the outer boundary Σ, it is assumed in the present work that wave disturbance are vanishingly small at Σ for a sufficiently long duration of time. We may impose

$$u = 0, \quad v = 0, \quad w = 0, \quad \text{and} \quad P = 0, \tag{4.8}$$

This approximation is asymptotically correct for a boundary sufficiently far away.

Treatment of the free-surface-body contact lines is another important issue, and the development of proper boundary conditions continues to be an active field of research. Yet, no definitive model has evolved. Nevertheless, several empirical remedies have been proposed in order to avoid the contact-line singularity problem. The most common one is the slippage model which allows a slip proportional to the shear stress. Huh and Mason (1977) have proposed a *local-slippage* model according to which it is assumed that fluid slips freely (the shear stress being zero) over a small length at the contact line.

The treatment applied in this work is based on Huh and Mason's model. On the contact line, for shear-stress to vanish,

$$\frac{\partial w}{\partial z} = 0, \quad \text{at } r = 1 \text{ and } z = 0. \tag{4.9}$$

We use Eqn. (4.9) to determine velocity w at the contact line. Velocities u and v are obtained from the no-slip condition.

Reproduced with permission of the copyright owner. Further reproduction prohibited without permission. www.manaraa.com

4.1.3 Calculation of force and moment

After the above hydrodynamic problem for u, v, w and P is solved, the non-dimensional forces and moment acting on the circular cylinder $\mathcal{S}$ can be obtained by integrating the stress using the constitutive relations

$$\begin{aligned}
F_x &= \int_{\mathcal{S}} [\tau_{rr}\cos\theta - \tau_{r\theta}\sin\theta]\, dS \\
&= -r_i \int_{-d}^{0} dz \int_0^{2\pi} d\theta P\cos\theta + \frac{r_i}{Re}\int_{-d}^{0} dz \int_0^{2\pi} d\theta \left[2\frac{\partial u}{\partial r}\cos\theta - \frac{\partial v}{\partial r}\sin\theta\right], \\
F_z &= \int_{\mathcal{S}} \tau_{rz} dS \\
&= \frac{r_i}{Re}\int_{-d}^{0} dz \int_0^{2\pi} d\theta \frac{\partial w}{\partial r}, \\
M_y &= \int_{\mathcal{S}} [\tau_{rr}\cos\theta - \tau_{r\theta}\sin\theta]\, z dS \\
&= -r_i \int_{-d}^{0} z dz \int_0^{2\pi} d\theta P\cos\theta + \frac{r_i}{Re}\int_{-d}^{0} z dz \int_0^{2\pi} d\theta \left[2\frac{\partial u}{\partial r}\cos\theta - \frac{\partial v}{\partial r}\sin\theta\right],
\end{aligned} \tag{4.10}$$

where τ_{ij} is the stress tensor. These forces are non-dimensionalized here by $\rho' U'^2 r_i'^2$, moment by $\rho' U'^2 r_i'^3$. Note that F_x and M_y consist of two double integrals, one due to pressure and the other due to viscous stress.

4.2 A spectral method of solution

The Numerical solution for Eqns. (4.1) and (4.2) are sought at each time step $t = k\Delta t, (k = 1, 2...)$, for a given time increment Δt. Consider the following difference schemes of Eqns. (4.1) and (4.2):

$$\frac{1}{\Delta t}(\mathbf{u}^{k+1} - \mathbf{u}^k) = \mathcal{Q}\left[-(\mathbf{u}\cdot\nabla)\mathbf{u} + \frac{1}{Re}\tilde{\nabla}^2\mathbf{u}\right] - \nabla P^{k+1}, \tag{4.11}$$

$$\nabla\cdot\mathbf{u}^{k+1} = 0, \tag{4.12}$$

where $\mathcal{Q}$ is a suitable difference operator (to be defined in Section 4.2.1), and $\tilde{\nabla}^2$ is the differential operator inside the brackets of Eqn. (4.1). The numerical algorithm for solving Eqns. (4.11) and (4.12) is given as follows. We first introduce an auxiliary

Reproduced with permission of the copyright owner. Further reproduction prohibited without permission. www.manaraa.com

velocity field $\hat{\mathbf{u}}$, satisfying

$$\frac{1}{\Delta t}(\hat{\mathbf{u}} - \mathbf{u}^k) = \mathcal{Q}\left[-(\mathbf{u}\cdot\nabla)\mathbf{u} + \frac{1}{Re}\tilde{\nabla}^2\mathbf{u}\right], \tag{4.13}$$

and we subtract Eqn. (4.13) from Eqn. (4.11) to obtain

$$\frac{1}{\Delta t}(\mathbf{u}^{k+1} - \hat{\mathbf{u}}) = -\nabla P^{k+1}. \tag{4.14}$$

If we apply divergence operator onto Eqn. (4.14), we obtain a Poisson equation at each discrete time instant for P^{k+1}

$$\nabla^2 P^{k+1} = \frac{1}{\Delta t}\nabla\cdot\hat{\mathbf{u}}, \tag{4.15}$$

Note that Eqn. (4.12) has been used to derive Eqn. (4.15); thus mass conservation is assured.

After the P^{k+1} has been calculated from Eqn. (4.15), it is substituted into Eqn. (4.14) to obtain $\mathbf{u}^{k+1}$. This formulation is based on Chorin's method (Chorin, 1968), and was implemented by Yeung and Ananthakrishnan (1992) with additional boundary conditions arisen from the body and the free surface.

In summary, we first evaluate an intermediate auxiliary velocity field using Eqn (4.13). The pressure field is solved next based on Eqn. (4.15). A pressure correction step concludes the procedure using Eqn. (4.14). The detailed implementation of this procedure will be presented in the next three sections.

4.2.1 Calculation of auxiliary velocity

The difference operator $\mathcal{Q}$ in Eqn. (4.13) requires elaboration. The idea is similar to Goda (1977). To calculate the auxiliary velocity $\hat{\mathbf{u}}$, two additional auxiliary velocities $\mathbf{u}^*$ and $\mathbf{u}^{**}$ are introduced into Eqn. (4.13) to simplify the computations For $\hat{u}$:

$$\begin{aligned}
&\frac{1}{\Delta t}(u^* - u^k) = -u^k u^*_r + \frac{1}{Re}[u^*_{rr} + \frac{1}{r}u^*_r - \frac{u^*}{r^2}],\\
&\frac{1}{\Delta t}(u^{**} - u^*) = -\frac{v^*}{r}u^{**}_\theta + \frac{v^{k^2}}{r} + \frac{1}{Re}[\frac{1}{r^2}u^{**}_{\theta\theta} - \frac{2}{r^2}v^k_\theta],\\
&\frac{1}{\Delta t}(\hat{u} - u^{**}) = -w^{**}\hat{u}_z + \frac{1}{Re}[\hat{u}_{zz}];
\end{aligned} \tag{4.16}$$

Reproduced with permission of the copyright owner. Further reproduction prohibited without permission. www.manaraa.com

For $\hat{v}$:

$$\begin{aligned}
&\frac{1}{\Delta t}(v^* - v^k) = -u^k v^*_r + \frac{1}{Re}[v^*_{rr} + \frac{1}{r}v^*_r - \frac{v^*}{r^2}],\\
&\frac{1}{\Delta t}(v^{**} - v^*) = -\frac{v^*}{r}v^{**}_\theta - \frac{u^k v^k}{r} + \frac{1}{Re}[\frac{1}{r^2}v^{**}_{\theta\theta} + \frac{2}{r^2}u^k_\theta],\\
&\frac{1}{\Delta t}(\hat{v} - v^{**}) = -w^{**}\hat{v}_z + \frac{1}{Re}[\hat{v}_{zz}];
\end{aligned} \tag{4.17}$$

For $\hat{w}$:

$$\begin{aligned}
&\frac{1}{\Delta t}(w^* - w^k) = -u^k w^*_r + \frac{1}{Re}[w^*_{rr} + \frac{1}{r}w^*_r],\\
&\frac{1}{\Delta t}(w^{**} - w^*) = -\frac{v^*}{r}w^{**}_\theta + \frac{1}{Re}[\frac{1}{r^2}w^{**}_{\theta\theta}],\\
&\frac{1}{\Delta t}(\hat{w} - w^{**}) = -w^{**}\hat{w}_z + \frac{1}{Re}[\hat{w}_{zz}].
\end{aligned} \tag{4.18}$$

It is worthwhile to note that these variables do not require extra storage, because $\mathbf{u}^*$ and $\mathbf{u}^{**}$ can share the same storage with $\hat{\mathbf{u}}$. If we introduce the following four difference operators $\mathcal{Q}'_r$, $\mathcal{Q}_r$, $\mathcal{Q}_\theta$ and $\mathcal{Q}_z$ as

$$\begin{aligned}
&\mathcal{Q}'_r \equiv -u^k\frac{\partial}{\partial r} + \frac{1}{Re}[\frac{\partial^2}{\partial r^2} + \frac{1}{r}\frac{\partial}{\partial r} - \frac{1}{r^2}],\\
&\mathcal{Q}_r \equiv -u^k\frac{\partial}{\partial r} + \frac{1}{Re}[\frac{\partial^2}{\partial r^2} + \frac{1}{r}\frac{\partial}{\partial r}],\\
&\mathcal{Q}_\theta \equiv -\frac{v^*}{r}\frac{\partial}{\partial \theta} + \frac{1}{Re}[\frac{1}{\theta^2}\frac{\partial^2}{\partial r^2}],\\
&\mathcal{Q}_z \equiv -w^{**} + \frac{1}{Re}[\frac{\partial^2}{\partial z^2}],
\end{aligned} \tag{4.19}$$

Eqns. (4.16) to (4.17) can be rewritten as

For $\hat{u}$:

$$\begin{aligned}
&\frac{1}{\Delta t}(u^* - u^k) = \mathcal{Q}'_r u^*,\\
&\frac{1}{\Delta t}(u^{**} - u^*) = \mathcal{Q}_\theta u^{**} + A^k_1,\\
&\frac{1}{\Delta t}(\hat{u} - u^{**}) = \mathcal{Q}_z\hat{u};
\end{aligned} \tag{4.20}$$

Reproduced with permission of the copyright owner. Further reproduction prohibited without permission. www.manaraa.com

For $\hat{v}$:

$$\begin{aligned}
\frac{1}{\Delta t}(v^* - v^k) &= \mathcal{Q}_r' v^*, \\
\frac{1}{\Delta t}(v^{**} - v^*) &= \mathcal{Q}_\theta v^{**} + A_2^k, \\
\frac{1}{\Delta t}(\hat{v} - v^{**}) &= \mathcal{Q}_z \hat{v};
\end{aligned} \tag{4.21}$$

For $\hat{w}$:

$$\begin{aligned}
\frac{1}{\Delta t}(w^* - w^k) &= \mathcal{Q}_r w^*, \\
\frac{1}{\Delta t}(w^{**} - w^*) &= \mathcal{Q}_\theta w^{**}, \\
\frac{1}{\Delta t}(\hat{w} - w^{**}) &= \mathcal{Q}_z \hat{w},
\end{aligned} \tag{4.22}$$

where A_1^k are A_2^k are known functions defined by:

$$A_1^k = \frac{v^{k2}}{r} - \frac{2}{Rer^2} v_\theta^k, \qquad A_2^k = -\frac{u^k v^k}{r} + \frac{2}{Rer^2} u_\theta^k. \tag{4.23}$$

The scheme in Eqns. (4.16) - (4.18) is a variation of the ADI method (see e.g. Sod, 1985). Consistency of the above procedure can be easily shown. If we take Eqn. (4.20) for example, it can be rewritten as:

$$\begin{aligned}
u^* &= (1 - \Delta t \mathcal{Q}_r')^{-1} u^k, \\
u^{**} &= (1 - \Delta t \mathcal{Q}_\theta)^{-1} [u^* + \Delta t A_1^k], \\
\hat{u} &= (1 - \Delta t \mathcal{Q}_z)^{-1} u^{**}.
\end{aligned} \tag{4.24}$$

Elimination of the intermediate velocities u^* and u^{**} yields

$$\begin{aligned}
\hat{u} &= (1 - \Delta t \mathcal{Q}_r')^{-1} (1 - \Delta t \mathcal{Q}_\theta)^{-1} [(1 - \Delta t \mathcal{Q}_z)^{-1} u^k + \Delta t A_1^k] \\
&= (1 + \Delta t \mathcal{Q}_r' + \Delta t \mathcal{Q} + \Delta t \mathcal{Q}_z) u^k + \Delta t A_1^k + O(\Delta t^2)
\end{aligned} \tag{4.25}$$

It is evident that the present procedure is an approximation of Eqn. (4.13).

Note that Eqns. (4.16) - (4.18) are of implicit forms for each intermediate velocity $\mathbf{u}^*$, $\mathbf{u}^{**}$ and $\hat{\mathbf{u}}$. Thus, by von Neumann's linear stability theory (see e.g. Sod, 1985), each of these schemes is unconditionally stable, assuming that the each coefficient of nonlinear terms is a local constant. Although each of Eqns. (4.16) - (4.18) is independently stable, the total stability condition of Eqns. (4.16) - (4.18) and Eqn. (4.14) is not strictly established.

Reproduced with permission of the copyright owner. Further reproduction prohibited without permission. www.manaraa.com

The above Eqns. (4.16)-(4.18) can be further rearranged and regrouped into the following three sets of ordinary differential equations (ODEs):

For $\mathbf{u}^*$:

$$\begin{aligned} u^*_{rr} + (\frac{1}{r} - Reu^k)u^*_r + (-\frac{1}{r^2} - \frac{Re}{\Delta t})u^* &= -\frac{Re}{\Delta t}u^k, \\ v^*_{rr} + (\frac{1}{r} - Reu^k)v^*_r + (-\frac{1}{r^2} - \frac{Re}{\Delta t})v^* &= -\frac{Re}{\Delta t}v^k, \\ w^*_{rr} + (\frac{1}{r} - Reu^k)w^*_r - \frac{Re}{\Delta t}w^* &= -\frac{Re}{\Delta t}w^k; \end{aligned} \tag{4.26}$$

For $\mathbf{u}^{**}$:

$$\begin{aligned} u^{**}_{\theta\theta} - Rerv^*u^{**}_\theta - \frac{Rer}{\Delta t}u^{**} &= -\frac{Rer^2}{\Delta t}u^* - Rer^2A^k_1, \\ v^{**}_{\theta\theta} - Rerv^*v^{**}_\theta - \frac{Rer}{\Delta t}v^{**} &= -\frac{Rer^2}{\Delta t}v^* - Rer^2A^k_2, \\ w^{**}_{\theta\theta} - Rerv^*w^{**}_\theta - \frac{Rer}{\Delta t}w^{**} &= -\frac{Rer^2}{\Delta t}w^*; \end{aligned} \tag{4.27}$$

For $\hat{\mathbf{u}}$:

$$\begin{aligned} \hat{u}_{zz} - Rew^{**}\hat{u}_z - \frac{Re}{\Delta t}\hat{u} &= -\frac{Re}{\Delta t}u^{**}, \\ \hat{v}_{zz} - Rew^{**}\hat{v}_z - \frac{Re}{\Delta t}\hat{v} &= -\frac{Re}{\Delta t}v^{**}, \\ \hat{w}_{zz} - Rew^{**}\hat{w}_z - \frac{Re}{\Delta t}\hat{w} &= -\frac{Re}{\Delta t}w^{**}. \end{aligned} \tag{4.28}$$

Eqns. (4.26) and (4.28) are ODEs in radial r and vertical z directions respectively, and are solved by a Chebyshev spectral collocation method, with Chebyshev grid spacings in these two directions (see Appendix B.2). Eqns. (4.27) are ODEs in circumferential θ direction, and are solved by Fourier spectral collocation method in a uniform grid spacing (see Appendix B.2). It is worthwhile to emphasize that the auxiliary velocities $\mathbf{u}^*$, $\mathbf{u}^{**}$ and $\hat{\mathbf{u}}$ are not physical and the boundary conditions for solving them need to be derived with care and consistency. The boundary conditions for auxiliary velocities and pressure are developed next for various types of surfaces.

4.2.2 Implementation of boundary conditions

To illustrate the treatment of the velocity boundary condition, we take the case of u^*, u^{**} and $\hat{u}$ in Eqn. (4.16) as an example. The boundary conditions for

Reproduced with permission of the copyright owner. Further reproduction prohibited without permission. www.manaraa.com

solving u^*, u^{**} and $\hat{u}$ in Eqns. (4.26) to (4.28) can be formally written as

$$\begin{aligned} u^* &= u^{k+1} - \Delta t(\mathcal{Q}_\theta u^{k+1} + A_1^{k+1} + \mathcal{Q}_z u^{k+1} - \mathcal{G}_r P^{k+1}), \\ u^{**} &= u^{k+1} - \Delta t(\mathcal{Q}_z u^{k+1} - \mathcal{G}_r P^{k+1}), \\ \hat{u} &= u^{k+1} - \Delta t(-\mathcal{G}_r P^{k+1}), \end{aligned} \tag{4.29}$$

where $\mathcal{G}_r$ denotes the gradient difference operator in r direction. Each of Eqns. (4.29) above is derived by subtracting each of Eqns. (4.16) from the $u-$component equation in Eqn. (4.11). In Eqns. (4.29), if either P^{k+1} or u^{k+1} are not known, we can replace P^{k+1} by P^k and u^{k+1} by u^k respectively. Specifically, the first equation of Eqns. (4.29) provides boundary conditions for u^* (in the first equation of Eqns. 4.26) at $r = r_i$ and r_o; the third equation of Eqns. (4.29) yields boundary conditions for $\hat{u}$ (in the first equation of Eqns. 4.28) at $z = -d$ and 0. Since u^{**} (in the first equation of Eqns. 4.27) is solved in the *periodic* circumferential θ direction; no boundary conditions is thus needed, the second equation of Eqns. (4.29) can be dropped. Thus, in summary, we have

$$\begin{aligned} u^* &= u^k - \Delta t(\mathcal{Q}_\theta u^k + A_1^k + \mathcal{Q}_z u^k - \mathcal{G}_r P^k), && \text{at } r = r_i \text{ or } r_o, \\ \hat{u} &= u^k - \Delta t(-\mathcal{G}_r P^k), && \text{at } z = -d \text{ or } 0. \end{aligned} \tag{4.30}$$

The boundary conditions for $v-$ and $w-$ components can be derived similarly and are given by

$$\begin{aligned} v^* &= v^k - \Delta t(\mathcal{Q}_\theta v^k + A_2^k + \mathcal{Q}_z v^k - \mathcal{G}_\theta P^k), && \text{at } r = r_i \text{ or } r_o, \\ \hat{v} &= v^k - \Delta t(-\mathcal{G}_\theta P^k), && \text{at } z = -d \text{ or } 0, \end{aligned} \tag{4.31}$$

and

$$\begin{aligned} w^* &= w^k - \Delta t(\mathcal{Q}_\theta w^k + \mathcal{Q}_z w^k - \mathcal{G}_z P^k), && \text{at } r = r_i \text{ or } r_o, \\ \hat{w} &= w^k - \Delta t(-\mathcal{G}_z P^k), && \text{at } z = -d \text{ or } 0, \end{aligned} \tag{4.32}$$

where $\mathcal{G}_\theta$ and $\mathcal{G}_z$, similarly, denote gradient difference operators in θ and z directions.

Reproduced with permission of the copyright owner. Further reproduction prohibited without permission. www.manaraa.com

Free-Slip or No-Slip Surfaces

For the case of no-slip wall or free-slip boundary, the boundary conditions in Eqns. (4.30) to (4.32) can be further simplified. In normal and tangential coordinates, such conditions fall into one of the following forms: (a) The no-slip wall condition

$$u_n = u_{\tau_1} = u_{\tau_2} = 0, \tag{4.33}$$

or (b) The free-slip boundary condition

$$u_n = 0, \qquad \frac{\partial u_{\tau_1}}{\partial n} = \frac{\partial u_{\tau_2}}{\partial n} = 0, \tag{4.34}$$

where u_n, u_{τ_1} and u_{τ_2} denote the velocity components along the normal (n) and two tangential (τ_1 and τ_2) directions of the boundary surface, respectively.

For numerical implementation of the above two boundary conditions (Eqns. 4.33 and 4.34), we set the normal component of the auxiliary velocity $\hat{u}_n$ to be the same as the actual normal velocity ${u_n}^{k+1}$

$$\hat{u}_n = {u_n}^{k+1}. \tag{4.35}$$

Then Eqn. (4.35) together with Eqn. (4.14) implies the following homogeneous Neumann condition for P^{k+1} on these boundaries:

$$\frac{\partial P^{k+1}}{\partial n} = 0. \tag{4.36}$$

Using Eqns. (4.33), (4.34) and (4.36), we reduce the general boundary conditions for auxiliary velocities $\mathbf{u}^*$ and $\hat{\mathbf{u}}$ (Eqns. 4.30 to 4.32) to

$$\begin{aligned} &u^* = 0, \quad v^* = \Delta t \frac{1}{r}\frac{\partial P^k}{\partial \theta}, \quad w^* = \Delta t \frac{\partial P^k}{\partial z}, && \text{at } r = r_i \text{ or } r_o, \\ &\hat{u} = \Delta t \frac{\partial P^k}{\partial r}, \quad \hat{v} = \Delta t \frac{1}{r}\frac{\partial P^k}{\partial \theta}, \quad \hat{w} = 0, && \text{at } z = -d \text{ or } 0, \end{aligned} \tag{4.37}$$

for the case of no-slip wall, and

$$\begin{aligned} &u^* = -\Delta t A_1^k, \quad \frac{\partial v^*}{\partial r} = -\Delta t \frac{\partial A_2^k}{\partial r}, \quad \frac{\partial w^*}{\partial r} = 0, && \text{at } r = r_i \text{ or } r_o, \\ &\frac{\partial \hat{u}}{\partial z} = 0, \quad \frac{\partial \hat{v}}{\partial z} = 0, \quad \hat{w} = 0, && \text{at } z = -d \text{ or } 0, \end{aligned} \tag{4.38}$$

for the case of free-slip wall.

Reproduced with permission of the copyright owner. Further reproduction prohibited without permission. www.manaraa.com

Free-surface conditions

The situation is somewhat more involved for the case of a free-surface boundary. Thus we choose first to illustrate its implementation by a simple one-step explicit time-marching scheme. The boundary conditions at $z = 0$ in Eqns. (4.30) to (4.32) are used in their original forms as Dirichlet conditions for solving the ODEs for the auxiliary velocities in Eqn. (4.28). The second equation of Eqns. (4.5) yields a Dirichlet boundary condition for solving the Poisson equation for pressure in Eqn. (4.15)

$$P^{k+1} = \frac{\eta^k}{F_r^2} + \frac{2}{Re}\frac{\partial w^k}{\partial z}, \qquad \text{at} \quad z = 0. \tag{4.39}$$

The stress relation in Eqn. (4.5) based on current values are used to update values of velocity on free surface

$$\begin{aligned} \frac{\partial w^{k+1}}{\partial z} &= \frac{Re}{2}(P^{k+1} - \frac{\eta^k}{F_r^2}), \\ \frac{\partial u^{k+1}}{\partial z} &= -\frac{\partial w^{k+1}}{\partial r}, \\ \frac{\partial v^{k+1}}{\partial z} &= -\frac{1}{r}\frac{\partial w^{k+1}}{\partial \theta}, \qquad \text{at} \quad z = 0. \end{aligned} \tag{4.40}$$

The kinematic free-surface condition in Eqn. (4.6) is integrated to update the free-surface elevation η

$$\eta^{k+1} = \eta^k + \Delta t w^{k+1}. \tag{4.41}$$

If it is found that the above explicit treatment of the free-surface conditions does not guarantee required accuracy, we will use the following two-step predictor-corrector type scheme:

Predictor Step:

$$P^{\overline{k+1}} = \frac{\eta^k}{F_r^2} + \frac{2}{Re}\frac{\partial w^k}{\partial z}, \qquad \text{at} \quad z = 0. \tag{4.42}$$

Reproduced with permission of the copyright owner. Further reproduction prohibited without permission. www.manaraa.com

$$\frac{\partial w^{\overline{k+1}}}{\partial z} = \frac{Re}{2}(P^{\overline{k+1}} - \frac{\eta^k}{F_r^2}),$$
$$\frac{\partial u^{\overline{k+1}}}{\partial z} = -\frac{\partial w^{\overline{k+1}}}{\partial r}, \tag{4.43}$$
$$\frac{\partial v^{\overline{k+1}}}{\partial z} = -\frac{1}{r}\frac{\partial w^{\overline{k+1}}}{\partial \theta}, \qquad \text{at} \quad z = 0.$$

$$\eta^{\overline{k+1}} = \eta^k + \Delta t w^{\overline{k+1}}. \tag{4.44}$$

Corrector Step:

$$P^{k+1} = \frac{\eta^{\overline{k+1}}}{F_r^2} + \frac{2}{Re}\frac{\partial w^{\overline{k+1}}}{\partial z}, \qquad \text{at} \quad z = 0. \tag{4.45}$$

$$\frac{\partial w^{k+1}}{\partial z} = \frac{Re}{2}(P^{k+1} - \frac{\eta^{\overline{k+1}}}{F_r^2}),$$
$$\frac{\partial u^{k+1}}{\partial z} = -\frac{\partial w^{k+1}}{\partial r}, \tag{4.46}$$
$$\frac{\partial v^{k+1}}{\partial z} = -\frac{1}{r}\frac{\partial w^{k+1}}{\partial \theta}, \qquad \text{at} \quad z = 0.$$

$$\eta^{k+1} = \eta^k + \frac{\Delta t}{2}(w^{\overline{k+1}} + w^{k+1}). \tag{4.47}$$

Note that this predictor-corrector algorithm requires solution of the Poisson equation twice at each instant of time.

4.2.3 Solution of the pressure equation

In cylindrical coordinates, Eqn. (4.15) can be rewritten more explicitly as

$$\nabla^2 P = \frac{1}{\Delta t}\left[\frac{1}{r}\frac{\partial(r\hat{u})}{\partial r} + \frac{1}{r}\frac{\partial \hat{v}}{\partial \theta} + \frac{\partial \hat{w}}{\partial z}\right], \tag{4.48}$$

subject to a Neumann condition (Eqn. 4.36 on a slip or a no-slip boundary surface) or a Dirichlet condition (Eqn. 4.39 for the case of a free surface). This fits precisely into a form that was discussed in Chapter 2, and can be treated by the spectral method detailed therein.

Reproduced with permission of the copyright owner. Further reproduction prohibited without permission. www.manaraa.com

Chapter 5

Results for viscous flow

In this chapter, we will apply the numerical method presented in the previous chapter to several fluid dynamics problems involving a vertical cylinder in a viscous fluid. These problems include: (1) cylindrical cavity flows, (2) a Cauchy-Poisson wave problem for viscous fluid, (3) a sheared current past cylinder under a free-slip surface, and (4) a uniform current past a cylinder under a free surface. Test cases for each will also be presented when appropriate.

5.1 Rotating cylinder in a viscous fluid: A test

As a test of the method's ability to handle large-time simulations, we solve a cylindrical version of the Stokes's second problem for a viscous flow driven by an oscillating wall. Consider in Fig. 2.1, a solid cylinder S of radius r_i' rotating back and forth about its axis z with angular frequency ω' in an initially still and unbounded viscous fluid. If we choose to non-dimensionalize the variables of the problem by r_i' and ω', the non-dimensional circumferential velocity at the cylinder surface is specified as

$$v(1,t) = \begin{cases} 0 & \text{when } t < 0 \\ \sin(t) & \text{when } t \geq 0. \end{cases} \tag{5.1}$$

The momentum equation in the θ direction governing such a flow can be written as

$$\frac{\partial v}{\partial t} = \frac{1}{Re}\left(\frac{\partial^2 v}{\partial r^2} + \frac{1}{r}\frac{\partial v}{\partial r} - \frac{v}{r^2}\right), \tag{5.2}$$

Reproduced with permission of the copyright owner. Further reproduction prohibited without permission. www.manaraa.com

where the Reynolds number Re is defined as $\omega r_i^2/\nu$. A steady-state solution of the above equation is of the form

$$v(r,t) = Im[f(r)e^{\mathrm{i}t}]. \tag{5.3}$$

where $\mathrm{i} = \sqrt{-1}$ and t is nondimensionalized by $1/\omega$. It is not difficult to derive that

$$f(r) = \frac{K_1(\frac{1+\mathrm{i}}{2}\sqrt{Re}r)}{K_1(\frac{1+\mathrm{i}}{2}\sqrt{Re})}, \tag{5.4}$$

where K_1 denotes the first order modified Bessel function of the second kind.

To test our code, we solve this problem as a fully three-dimensional problem. Specifically, free-slip boundary conditions (Eqn. 4.34) are used on the top surface $\mathcal{F}$, the bottom surface $\mathcal{B}$ and the far-field boundary Σ . The far-field boundary Σ is taken to be at a distance of 10. Grid resolution of $L = 48$, $M = 16$ and $N = 24$, and Reynolds number $Re = 100$ are chosen for this study. Fig. 5.1 shows a sample of the velocity profiles $v(r,t)$ at eight instants of time during the first period of oscillation and the corresponding profile during the $7th$ cycle, which may be taken as the steady-state limit. Numerical results show that the transients are only significant during the first couple of cycles of oscillation. To establish the accuracy of our numerical solution, we further plot in Fig. 5.2 a comparison of the real and imaginary parts of function $f(r)$ (Eqn. 5.3) with the numerical values. Excellent agreement is observed.

5.2 Flows in a cylindrical cavity

In this section, we proceed to solve a series of cylindrical cavity flow problems, in which the fluid is entirely enclosed by solid boundaries, and the flow is driven by an impulsively-started sliding motion of one of the boundaries. The two-dimensional version of this problem is well known (see e.g. Sherman, 1990). It has often served as a testing ground for competing numerical methods, the objective of the competition being to prove that one's favorite method reveals accurately more realistic details of the flow than other methods with comparable computation efforts. There is little literature for the (three-dimensional) cylindrical cavity case, however.

Reproduced with permission of the copyright owner. Further reproduction prohibited without permission. www.manaraa.com

5.2.1 A Cavity driven by the steady motion of wall

Imagine a three-dimensional flow enclosed in a cylindrical region (see Fig. 2.1) where boundaries $\mathcal{F}$, $\mathcal{B}$ and $\mathcal{S}$ are stationary walls, while the remaining boundary Σ slides upwards with a constant speed W starting at $t = 0$. To solve this problem, we first non-dimensionalize the flow parameters by the following natural choice of primary variables: the height of domain d' and wall velocity W'. The Reynolds number Re is defined by $W'd'/\nu'$. No-slip boundary conditions (Eqn. 4.33) are applied at all these boundaries.

The possibility of a steady-state solution in this problem is investigated. The three-dimensional code was run for t as large as 4.0, using a time step $\Delta t = 0.01$, for a grid resolution of $L \times M \times N = 24 \times 16 \times 24$ until less than 0.01 percentage change in the velocity field was observed. It was found that steady-state solution is approached as early as $t = 3.0$ for the case of $Re = 200$, and a somewhat larger value for higher Reynolds numbers. To accentuate the vortical patterns, only results for up to a value of $Re = 200$ are shown here.

In Fig. 5.3, we show the velocity-vector plots for four different Reynolds numbers on a plane of constant circumferential angle θ. Also plotted are the streamline patterns. Since the cavity is driven axi-symmetrically (which is not a restriction in our method), the solution is axi-symmetric. It is of interest to observe that at Reynolds number smaller than 10 (see Fig. 5.3a, b), the core of the characteristic ring vortex is located at the mid-height of the cavity ($z = -d/2$). Considerable "symmetry" of the streamline patterns about the mid-height plane is observed. As the Reynolds number increases, the core of the primary vortex is driven towards the top wall and the sliding surface.

As mentioned earlier, the free-slip boundary condition corresponds to a special limit of the free-surface boundary condition. It is of interest to note that a steady-state configuration is also reached when the top surface $\mathcal{F}$ is replaced by a free-slip wall (defined by Eqn. 4.7). Fig. 5.4 contrasts the steady-state flow patterns of the no-slip $\mathcal{F}$ with that of the a free-slip $\mathcal{F}$. In this run, the inner cylinder $\mathcal{S}$ is given the steady vertical velocity while the outer cylinder has a no-slip wall condition.

Reproduced with permission of the copyright owner. Further reproduction prohibited without permission. www.manaraa.com

From this figure, we notice a larger vortical structure in the free-slip case. This is consistent with the expectation that a free-slip wall is less restrictive to horizontal flow motion than a no-slip wall, thus allowing vortex to move more freely.

5.2.2 An oscillating cavity with free-slip boundary condition

In this section, we study the time-evolution of the cylindrical cavity flow driven by an oscillatory inner wall in the presence of either a free-slip $\mathcal{F}$ or a no-slip $\mathcal{F}$. This flow, with minor modifications in the boundary conditions on some of the boundary surfaces, can mimic the vorticity structures generated by a hull surface of a ship in heaving motion.

Consider again the flow configuration in Fig. 2.1, where the bottom boundary $\mathcal{B}$ and outer cylinder Σ are stationary walls, and upper boundary $\mathcal{F}$ is assumed to be a free-slip wall. The flow is driven by the motion of a no-slip inner cylinder $\mathcal{S}$, which oscillates periodically along the $z-$axis with prescribed velocity

$$W(t) = \begin{cases} 0 & \text{when } t < 0 \\ W_0 \sin(\omega t) & \text{when } t \geq 0 \end{cases}, \tag{5.5}$$

where W_0 is the amplitude of the vertical velocity, and ω the angular frequency of oscillation.

Nondimensionalization is carried out in the same manner as Section 5.2.1. For convenience, the distance between the inner and outer cylinders is chosen to be the same as the height of domain d'. The Reynolds number, defined in this case by $W_0' d'/\nu'$, is set to 100. The non-dimensional period of oscillation T is defined by $2\pi W_0'/\omega' d'$, and is taken to be 0.8.

Numerical results are obtained by a mesh size of $L \times M \times N = 24 \times 16 \times 24$, and time steps $\Delta t = 0.01$ and 0.02 have been used to check convergence, which is excellent. Because of the non-linear nature of the Navier-Stokes equations, a periodic solution is not expected. However, the flow is found to display an "almost" periodic behavior with a "steady streaming" effect (see Schlichting, 1968).

Reproduced with permission of the copyright owner. Further reproduction prohibited without permission. www.manaraa.com

Fig. 5.5 shows the velocity vectors and pathlines corresponding to four instants of time $t = 4T$, $4\frac{5}{40}T$, $4\frac{7}{40}T$, and $4\frac{10}{40}T$ during the first quarter cycle of the fifth period of oscillation. It is interesting to study the vortex evolution in this case. In Fig. 5.5b, the inner cylinder has just reversed its direction of motion and is in the process of picking up some velocity. A thin shear layer is formed next to the cylinder while a small clockwise (ring) vortex is generated under the top surface, but above the counter-clockwise vortex, a residue of the earlier quarter cycle of motion (Fig. 5.5a). This clockwise vortex later becomes dominant in the flow region while the counter-clockwise vortex shrinks to the lower corner (Fig. 5.5c). In Fig. 5.5d, the clockwise ring vortex has replaced the counter-clockwise vortex of Fig. 5.5a, and becomes the only visible vortex. The flow pattern in the second quarter of oscillation varies relatively slowly, while the pattern for the last two quarters represents a change of flow direction relative to the first two quarters.

5.3 Transient wave field near a cylinder

The Cauchy-Poisson wave problem solved in Chapter 3 for an inviscid fluid is re-examined here for a *viscous* fluid. In order to understand the influence of viscosity on the solution, results of viscous flows with different Reynolds numbers are obtained, and are compared with their inviscid counterparts whenever appropriate.

We first non-dimensionalize the flow parameters by the following primary variables: the radius of inner cylinder r_i', and gravitational acceleration g'. The characteristic velocity $\tilde{U}'$ is thus defined by $\sqrt{g'r_i'}$. The Reynolds number Re is defined by $\sqrt{g'r_i'}r_i'/\nu'$, and Froude number F_r is equal to unity. Linearized free-surface boundary conditions (4.5) are applied on free surface $\mathcal{F}$, while no-slip boundary conditions (4.33) are chosen on the inner cylinder $\mathcal{S}$, the outer cylinder Σ, and the bottom $\mathcal{B}$. The initial wave form is taken to be

$$\eta(r,\theta,t=0) = A\exp\left\{-2.651\left[(r\cos\theta - 2.318)^2 + (r\sin\theta)^2\right]\right\}, \qquad (5.6)$$

where A is the initial wave elevation at the center of the hump, which is located at $r = 2.318$. This corresponds to a hump located closer to the cylinder than in

Reproduced with permission of the copyright owner. Further reproduction prohibited without permission. www.manaraa.com

Eqn. (3.15), thus generating a higher velocity as the pulse "impacts" on cylinder (see Fig. 5.7).

Numerical results are obtained by a mesh size of $L \times M \times N = 64 \times 64 \times 32$ and a time step $\Delta t = 0.05$. Two values of Reynolds number of $10,000$ and $50,000$ are chosen to study the comparative effects of viscosity. A is taken to be 0.1 and d to be 2.0 in this computation. The three-dimensional code was run for t as large as 15. It was observed to be sufficiently long to allow the "main wave" to diffract around the cylinder.

During the early stage of the simulation, viscosity is expected to play only a minor role. The early-time flow features of viscous and inviscid flows are therefore expected to be similar. This is evident from Fig. 5.8, in which the free-surface elevations at $r = 1$ (body-free-surface intersection) and $r = 2.318$ (center of initial hump) are plotted as functions of time for (1) inviscid fluid, (2) viscous fluid with $Re = 50,000$ and (3) viscous fluid with $Re = 10,000$. Furthermore, Fig. 5.8 shows that the waves damp out much sooner in the case of $Re = 10,000$ than in the case of $Re = 50,000$ and in the inviscid fluid. The wave fields evolve in a similar way in the case of $Re = 50,000$ and the case of inviscid fluid. This behavior can also be observed from the perspective views of the overall free surface pattern plotted in Fig. 5.9. The similarity between the case of $Re = 50,000$ and the case of inviscid fluid confirms that the numerical method has little "numerical viscosity".

For a closer look at the flow patterns, we include vorticity contour plots for the above three cases in Figs. 5.10. In these figures, the velocity vectors are overlaid onto a vorticity contour plot in the vertical plane of symmetry containing the initial wave peak. The corresponding time is $t = 8.00$. Vortices of opposite signs can be clearly seen near the intersection of the body and the free surface in the two cases of viscous fluids. Boundary layers immediately above the bottom can be clearly seen from the enlarged views in these two cases, which is thicker in the case of $Re = 10,000$. Again, we observe from Figs. 5.10 that the *wave fields* in the case of $Re = 50,000$ and in the case of inviscid fluid are similar, while the case of $Re = 10,000$ displays a significant phase difference with the other two cases.

Finally, in Fig. 5.11, we show the hydrodynamic forces acting on the circular

Reproduced with permission of the copyright owner. Further reproduction prohibited without permission. www.manaraa.com

cylinder for these three cases. It is apparent that, in the case of viscous flow, the only significant component is the horizontal force due to pressure, which varies with time in a similar fashion to its inviscid counterpart. However, there is a difference in the magnitude of the peaks and a phase shift in the case of $Re = 10,000$.

5.4 Separated flows under a free-slip surface

As an illustration of the method's ability to model three-dimensional highly convective flows, we present some results for a sheared current past a vertical circular cylinder under free-slip "free surface". The free-slip surface condition of $\mathcal{F}$ can be easily replaced by a genuine free-surface condition in Eqns. (4.5).

The fluid is again enclosed by a cylindrical wall surface $\mathcal{S}$ at $r' = r'_i$, a free-slip surface $\mathcal{F}$ at $z' = 0$, a wall boundary $\mathcal{B}$ at $z' = -d'$, and an open boundary Σ at $r' = r'_o$. As before, we first proceed to non-dimensionalize the flow parameters. In this case, the obvious choices of primary variables are: the radius of inner cylinder r'_i, and the free-stream velocity U'. The Reynolds number Re is therefore defined by $U'r'_i/\nu'$.

The applied sheared current is a Poiseuille flow in the $x-$direction

$$u(z) = 1 - \left(\frac{z}{d}\right)^2, \tag{5.7}$$

and the pressure field

$$P = \frac{2}{Re}x. \tag{5.8}$$

Eqn. (5.7), together with Eqn. (5.8), is a well-known solution of the Navier-Stokes equations with a free-slip boundary condition at $z = 0$ and a wall boundary condition at $z = -d$.

5.4.1 A test problem

Before we solve the problem of such a uniform current past a circular cylinder, it is of interest first to check whether or not we can reproduce this one-dimensional

Reproduced with permission of the copyright owner. Further reproduction prohibited without permission. www.manaraa.com

flow (Eqn. 5.7) in Cartesian coordinates by using our Navier-Stokes solver as a three-dimensional application in cylindrical coordinates. To do that, we impose the shear current suddenly on *both* inner and outer cylinders at $t = 0$, and hold it constant thereafter. Specifically, the velocity profile in Eqn. (5.7) is imposed as Dirichlet condition for velocity, and the pressure given in Eqn. 5.8 as Dirichlet condition for pressure equation. The otherwise still fluid is driven by this sheared current, and begins to evolve from rest at $t' = 0$.

We choose $Re = 100$, $r_o = 3$ and $d = 1$. The mesh size is $L = 32$, $M = 32$ and $N = 32$, and time step $\Delta t = 0.05$.

The numerical results for such a test are presented in Figs. 5.12 (a) to (d). Velocity vectors and vorticity contours in the vertical plane of symmetry behind the inner cylinder are shown for four instants of time. In Fig. 5.12 (a), at $t = 1.0$, the flow is rather transient, and two vortical structures are observed at the lower corners. Fig. 5.12 (d) shows an almost steady flow, in which the velocity vectors everywhere in this plane have approached the Poiseuille velocity profile prescribed on the two cylindrical boundaries (given by Eqn. 5.7). The vorticity contours in this case are evenly spaced straight lines, corresponding a linearly varied vorticity distribution in the vertical direction. A close examination of the numerical data reveals that a maximum discrepancy between the value of velocity at any point in the domain and its expected steady-state value is less than 1% at $t = 50.0$. Thus both cylinders behave as they were perfectly porous surfaces.

5.4.2 Cylinder in a sheared current

In this section, we consider the flow about a real cylinder in the shear current. This can be modeled by replacing the boundary conditions (Eqns. 5.7 and 5.8) on the inner cylinder by a no-slip boundary condition for velocity (Eqn. 4.4) and a Neumann condition for pressure (Eqn. 4.36). This is again solved as a time-dependent problem, as the cylinder is suddenly put into a fully developed Poiseuille flow at $t = 0$. We also extend outer boundary to $r_o = 11$, so that the wake shed from the inner cylinder will not reach the outer boundary for an extended period of time. $Re = 275$ is chosen

Reproduced with permission of the copyright owner. Further reproduction prohibited without permission. www.manaraa.com

for this preliminary study, which corresponds to $Re_d = 550$, which Re_d is a Reynolds number based on diameter of the cylinder. In order to catch fine flow structures, a rather refined mesh of $L \times M \times N = 72 \times 128 \times 24$ is used. Time step Δt is set to be 0.0025.

Figs. 5.13(a) and (b) show the time evolution of such a flow with velocity vectors and pathlines on the free-slip surface near the circular cylinder. Only half the flow is shown due to its symmetry. In the early stage of the simulation, the flow is seemingly irrotational on the free-slip surface (Fig. 5.13a). As time elapses, vorticity is generated at the cylinder surface and transported to the rear side of the cylinder, inducing a flow reversal. Then, a flow separation appears (Fig. 5.13b), giving rise to a closed recirculating wake zone behind the cylinder, which grows in time until a steady state is reached. To shed some light on the three-dimensional features of this flow, a nearly steady state is plotted in Fig. 5.14. The figure on top shows the pathlines on five horizontal planes from near the bottom wall ($z = -0.991$) to the free-slip boundary ($z = 0$), while the bottom one presents vorticity contours. The time is $t = 3.0000$.

On the free-slip surface $z = 0$, a large clockwise vortical region (dashed lines) is observed behind the cylinder. The size of the closed recirculating zone decreases and its center moves upstream as the horizontal cut approaches the bottom, eventually disappearing on the bottom wall due to no-slip boundary conditions. Counterclockwise secondary vortical structures can also be seen at a short distance behind the cylinder. The flow separation and the formation of a closed recirculating zone behind the cylinder is also seen clearly in Fig. 5.15, in which vorticity contours and pathlines are plotted in two vertical planes at $\theta = 0$ (left) and π (right), a circular surface at $r = 1.02$ and a horizontal plane at $z = -0.99$. (The notations of the vorticity components plotted in this figure are given in the caption.) In the bottom plane of Fig. 5.15, a flow separation also occurs in front of the cylinder, due to a adverse pressure gradient ahead of the cylinder, forming a saddle point on the line of symmetry.

One of the most important flow features found in such a body/bottom juncture is the so called "horseshoe vortex". This phenomenon occurs in many places

Reproduced with permission of the copyright owner. Further reproduction prohibited without permission. www.manaraa.com

including appendage/hull junctures in ships, wing/fuselage junctures in aircrafts, high-rise buildings, and bridge piers in rivers, often leading to negative effects (see e.g. Hawthorne, 1954, Tan, 1989, Deng and Piquet, 1992). An overall picture of the flow is again seen in Figs. 5.15. On the vertical leading-edge plane (at right), the flow encounters an adverse pressure gradient in front of the cylinder, inducing a horseshoe vortex (dash-line). The horseshoe vortex, carried by the outer flow, trails off downstream (showed by solid-line in Fig. 5.16). In Fig. 5.16, an L-shaped end-wall vortex (dash-line) is formed along cylinder and bottom surfaces, displacing the horseshoe vortex away from the cylinder and bottom into the outer flow. A new counter-rotating end-wall vortex (solid-line) is then formed, which, in terms, displaces the former end-wall vortex away from the cylinder-bottom juncture. The formation of horseshoe vortex and its interaction with end-wall vortices can also been seen clearly from Figs. 5.17 and 5.18, which also shows a detailed velocity field near the cylinder. As a supplement to Figs. 5.17 and 5.18, magnified views of the velocity field in two radial planes reveal the existence of a secondary root vortex at the cylinder-bottom juncture. This vortex was also observed by Tan (1989) and Deng and Piquet (1992).

Finally, we show in Fig. 5.20 the hydrodynamic forces on the cylinder. The existence of steady state is again confirmed by this plot. It is interesting to note that the horizontal force due to shear stress constitutes nearly 1/10 of the total horizontal force, even though this is not a surprise at this low Reynolds number $Re = 275$.

It is a common engineering practice to estimate the total horizontal force on the cylinder by assuming that each differential element in the z direction can be modeled by a two-dimensional flow

$$F_x = \int_{-d}^{0} \frac{1}{2} C_d[Re(z)] DU(z)^2 dz = \int_{-d}^{0} C_d[Re(z)] \left[1 - (\frac{z}{d})^2\right]^2 dz, \qquad (5.9)$$

where $D = 2$ is the diameter of cylinder. Here C_d is the drag coefficient for a circular cylinder in two-dimensional flow, depending on the local Reynolds number $Re(z) = 275\,[1 - (z/d)^2]$. Experimental value of C_d as a function of Reynolds number is available from a number of sources (e.g. Schlichting, 1968). F_x estimated by using Eqn. (5.9) has a value of 0.79. Compared with the three-dimensional numerical results of 0.70824 shown in Fig. 5.20, it is overestimated by nearly 12%.

Reproduced with permission of the copyright owner. Further reproduction prohibited without permission. www.manaraa.com

5.5 Two-dimensional uniform flow past circular cylinder

The uniform viscous flow past a circular cylinder in the two-dimensional case is a classic problem in fluid mechanics. Since extensive experimental data exist for this case, it is an ideal problem to validate our numerical method. One of the most detailed experimental studies was conducted by Bouard and Contanceau (1980), where the initial development of the flow was carefully recorded and analyzed. These experimental results have been used extensively by numerical workers to validate their computational results. Numerical results obtained using finite-differences (e.g. Ta Phuoc Loc and Bouard, 1983) and by random vortex method (Stansby and Smith, 1991 and Yeung and Vaidhyanathan, 1992) agree fairly with experimental observations.

Before solving this problem numerically, we proceed to non-dimensionalize the flow parameters using primary variables: the radius of cylinder r_i', and the free-stream velocity U'. The Reynolds number Re is therefore defined by $U'r_i'/\nu'$. Numerical results for three Reynolds numbers of $Re = 275$, $1,500$ and 4750 were obtained, which corresponds to the cases of diameter Reynolds numbers of $Re_d = 550$, $3,000$ and 9500, studied in Bouard and Contanceau's experiment. To simulate these two-dimensional flows using our three-dimensional solver, we use free-slip boundary conditions (Eqn. 4.34) on the top surface $\mathcal{F}$ and the bottom surface $\mathcal{B}$. This is solved as a time-dependent problem: at time $t = 0$, the cylinder is put into an otherwise uniform flow, and the flow begins to evolve. A uniform velocity profile in the negative x-direction is imposed as initial condition in the entire computational domain, and is hold constant afterwards on the outer boundary Σ as boundary conditions. Zero pressure is imposed on the outer boundary Σ as boundary condition for pressure. The flow simulated here is kinematically equivalent to the flow around an impulsively started cylinder. For the cases of $Re = 275$ and $1,500$, a grid resolution of $L \times M \times N = 80 \times 128 \times 2$, and a time step of $\Delta t = 0.01$ are used. The radius of the outer boundary r_o is set to be 16.0. A finer grid resolution of $L \times M \times N = 80 \times 256 \times 2$,

Reproduced with permission of the copyright owner. Further reproduction prohibited without permission. www.manaraa.com

and a smaller time step of $\Delta t = 0.005$ are used for the case of $Re = 4750$, with r_o being 11.0.

Flow evolution for the cases of $Re = 275$ and $1,500$ is shown in Figs. 5.21 to 5.24. Flow patterns at $t = 6.0$ for these two cases agree well with Bouard and Contanceau's experimental results at a similar time $t^* = 2.5$, which is equivalent to $t = 5.0$. Bouard and Contanceau observed in their experiment that the secondary phenomena are somewhat different in these two cases. In the case of $Re = 275$ (or $Re_d = 550$), a single secondary eddy exists under a "protruding" flow structure (see Fig. 2(b) in Bouard and Contanceau, 1980), whereas when $Re = 1,500$ ($Re_d = 3,000$), a pair of secondary eddies are present (see Fig. 3(a) in Bouard and Contanceau, 1980). These flow differences are reproduced in the present simulation. For a quantitative comparison between the present numerical results and the experimental ones, we show in Fig. 5.25 the $x-$component velocity in the wake along the line of symmetry for $Re = 275$ and $1,500$. The agreement is excellent for these two cases at each one of the time instants.

The results for a higher Reynolds number of $Re = 4,750$ ($Re_d = 9,500$) are presented in Figs. 5.26 to 5.29. In these figures, the pathline and velocity vector plots are presented alongside with photos by Bouard and Contanceau (1980) at four corresponding time instants. Flow patterns agree excellently at each stage of the flow evolution.

5.6 Wave-induced separation around a circular cylinder

In this last result section on viscous flows, we will study the case of a uniform current past a vertical circular cylinder under a "real" free surface. We use the same annular computational domain as in the previous cases, which is bounded by a free surface $\mathcal{F}$, a bottom $\mathcal{B}$, a cylindrical cylinder $\mathcal{S}$, and an open boundary Σ. As our major interest in this case is the flow structures near the free surface, we use free-slip boundary conditions on the bottom boundary so that the horseshoe vortices (studied

Reproduced with permission of the copyright owner. Further reproduction prohibited without permission. www.manaraa.com

in Section 5.4.2) will not be generated to interfere with the flow near the free-surface. A uniform current, instead of the sheared current in Section 5.4.2, is used in this study, in order to be consistent with the free-slip boundary condition used on the bottom boundary. Similar to the previous cases, we proceed to non-dimensionalize the flow parameters using primary variables r_i' (radius of inner cylinder r_i'), and U' (the free-stream velocity). The Reynolds number Re is consequently defined as $U'r_i'/\nu'$.

The kinematic free-surface boundary condition in this case needs to be modified, in order to accommodate the fact that the $x-$component velocity on the free surface can be of order $O(1)$. This modified condition is written as

$$\frac{\partial \eta}{\partial t} + u_x \frac{\partial \eta}{\partial x} = w, \qquad \text{at } z = 0, \tag{5.10}$$

where u_x is the total $x-$component flow velocity, including the uniform stream. The dynamic conditions remain the same as in Eqns. (4.5).

A uniform flow in the negative $x-$direction

$$u = -\cos\theta, \quad v = \sin\theta, \quad w = 0 \tag{5.11}$$

is applied on the outer boundary Σ at all time, and is also used as initial conditions for the entire flow field. Dynamic pressure P is set to be zero on Σ at all time.

Owing to the presence of the free surface, if the no-slip boundary conditions are suddenly imposed at $t = 0$ on the cylinder surface in the uniform current, a splash will occur on the free surface, and will terminate the numerical simulation. In order to avoid this "initial splash", we use the following "porous" body boundary conditions

$$u = -\cos(\theta) f(t), \quad v = \sin(\theta) f(t), \quad w = 0, \qquad \text{at } r = r_i, \tag{5.12}$$

where $f(t)$ is a function of time t given by

$$f(t) = \begin{cases} \frac{1}{2}\left[1 + \cos\left(\frac{\pi t}{T_m}\right)\right] & \text{when } t < T_m \\ 0 & \text{when } t \geq T_m \end{cases} \tag{5.13}$$

with T_m being a modulation time. It is obvious that when $t \geq T_m$ Eqns. (5.12) acts like a no-slip condition as given by Eqns. (4.4).

Reproduced with permission of the copyright owner. Further reproduction prohibited without permission. www.manaraa.com

Numerical results are obtained here for $Re = 275$ and $Fr = 0.4$. A grid resolution of $L \times M \times N = 80 \times 128 \times 20$ and a time step $\Delta t = 0.01$ are used. Outer boundary Σ locates at $r_o = 16.0$, and the modulation time $T_m = 3.00$.

Fig. 5.30 shows the perspective views of the free-surface elevation at time $t = 6.00$ and $t = 10.00$. A rise in elevation at the bow and a drop in elevation at the stern are seen from these plots. Another depression is seen downstream near the widest position of the cylinder, because of the flow separation occurring near this location. Away from the cylinder, a Kelvin-like wave pattern is observed, which resembles the wave patterns trailing a moving ship.

To illustrate the flow patterns on the free surface near the cylinder, we plot pathlines and velocity vectors in Fig. 5.31, and pathlines and wave elevation contours in Fig. 5.32. The pathline patterns in these plots are similar to these in the two-dimensional cases plotted in Figs. 5.21 and 5.22 for $t = 3.00$. In Fig. 5.32, the deepest wave trough coincides with the center of the prime vortex, indicating the suction effects of vortex. Vorticity contours are plotted in Fig. 5.33 on five horizontal planes at different depths. Vorticity patterns underneath the free surface are shown in Figs. 5.34 and 5.35. The top curves on each section are the free surface elevations, which are enlarged by 10 times for clarity. In Fig. 5.34, the circumferential component of vorticity ω_θ is plotted on five radial planes at $\theta = 0$, $\pi/4$, $\pi/2$, $3\pi/4$ and π. In Fig. 5.35 the $x-$component vorticity ω_x is shown on nine vertical planes perpendicular to the outer flow. These vorticity patterns shows that in this case most of the vortical structures are located behind the cylinder, due to the massive wave-induced separation in this region. It appears in Fig. 5.34 that the vortical flow motion at the leading edge of cylinder is relatively weak. This is consistent with Yeung and Ananthakrishnan's (1992) finding that a clean free surface was unable to generate a strong cross-stream vortex.

To show the three-dimensional features of this flow, we plot in Fig. 5.36 to 5.38 iso-surfaces of vorticity components. Iso-surface for $\sqrt{{\omega_r}^2 + {\omega_\theta}^2} = 1.0$ is presented in Fig. 5.36, which shows some intricate vortical structures trailing from the cylinder surface. In Fig. 5.37, two iso-surfaces for the magnitude of vorticity vector are plotted. This figure confirms that cylinder surface is the major source of

Reproduced with permission of the copyright owner. Further reproduction prohibited without permission. www.manaraa.com

vortex generation in this case. The iso-surfaces for the vertical component of vorticity ω_z are shown in Fig. 5.38, which accentuate the three-dimensional recirculating zone behind the cylinder. The iso-surfaces for the dynamic pressure $P = -0.4, -0.1$ and 0.2 are plotted in Fig. 5.39. Fig. 5.40 shows the trajectories of two particles released in front of the cylinder. The particle released near the free surface moves smoothly downstream, circumventing the recirculating zone behind the cylinder. By contrast, the particle released near the free-slip bottom is trapped into the recirculating zone, circulating and moving upwards in a violent manner.

Reproduced with permission of the copyright owner. Further reproduction prohibited without permission. www.manaraa.com

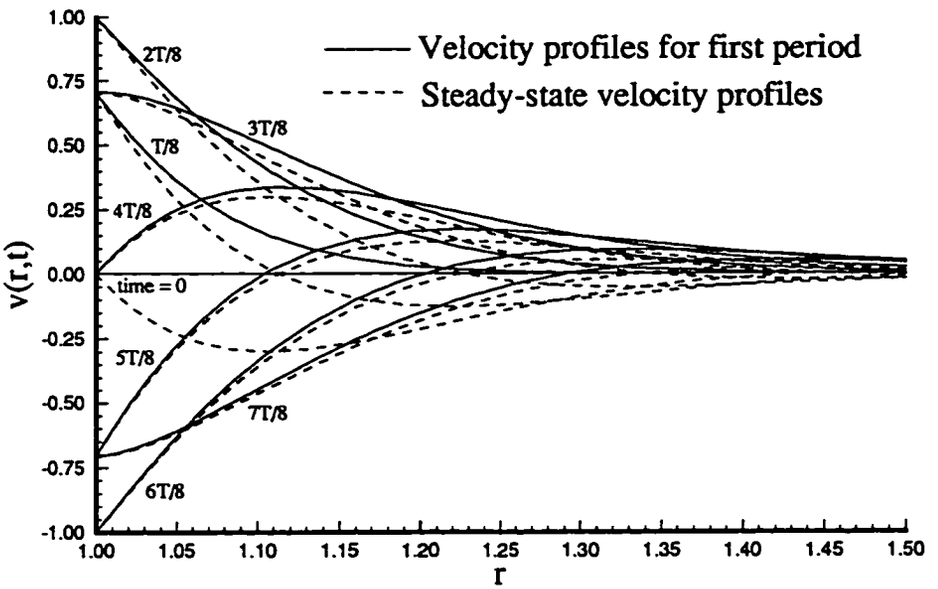

Figure 5.1: Velocity profiles in the first period of motion and in steady-state.

Reproduced with permission of the copyright owner. Further reproduction prohibited without permission. www.manaraa.com

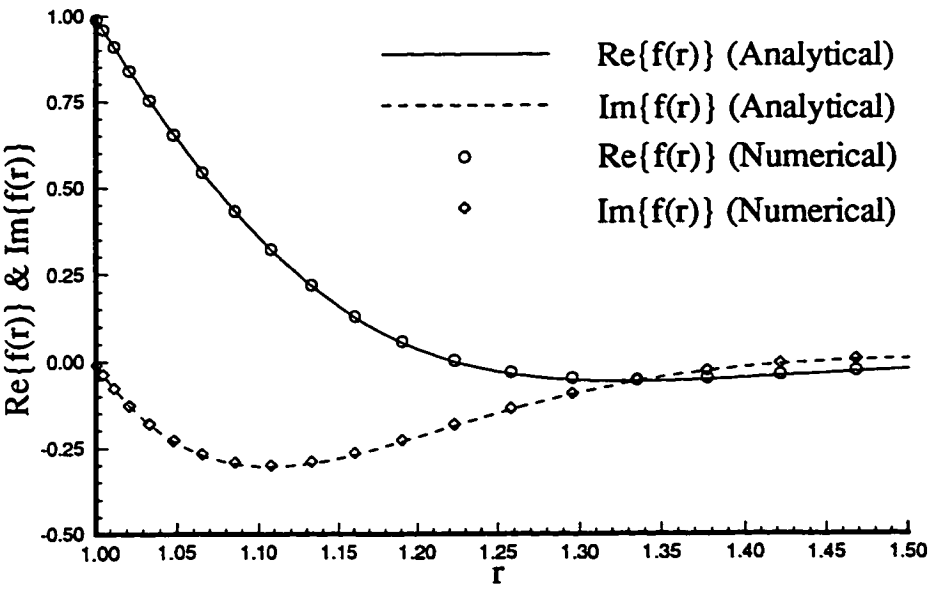

Figure 5.2: Real and imaginary parts of $f(r)$ in Eqn. (5.3).

Reproduced with permission of the copyright owner. Further reproduction prohibited without permission. www.manaraa.com

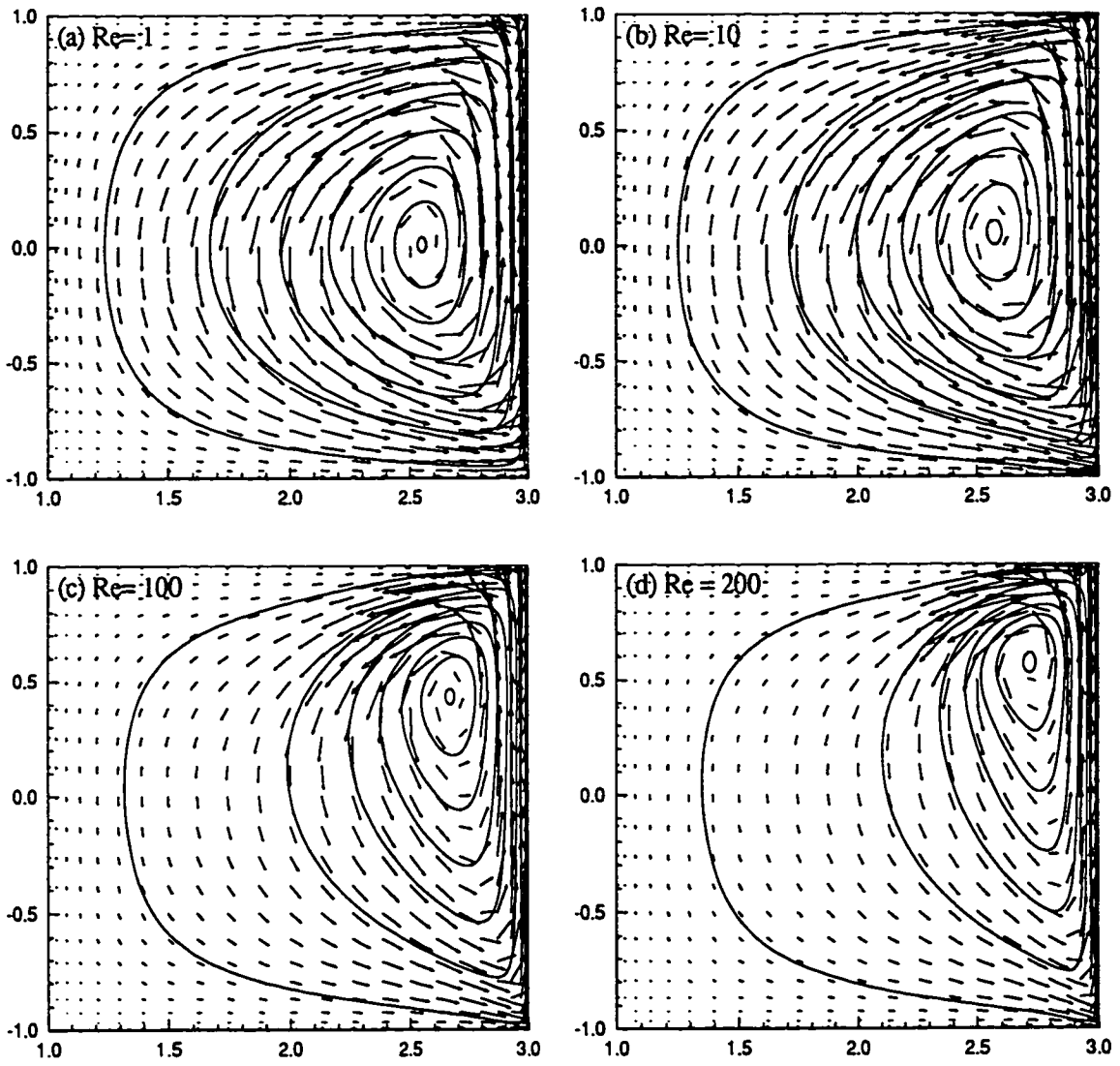

Figure 5.3: Steady-state streamlines in a cylindrical cavity for different Reynolds numbers (driven by outer cylinder): (a) $Re = 1$, $t = 2.0$; (b) $Re = 10$, $t = 2.0$; (c) $Re = 100$, $t = 3.0$; (d) $Re = 200$, $t = 3.0$.

Reproduced with permission of the copyright owner. Further reproduction prohibited without permission. www.manaraa.com

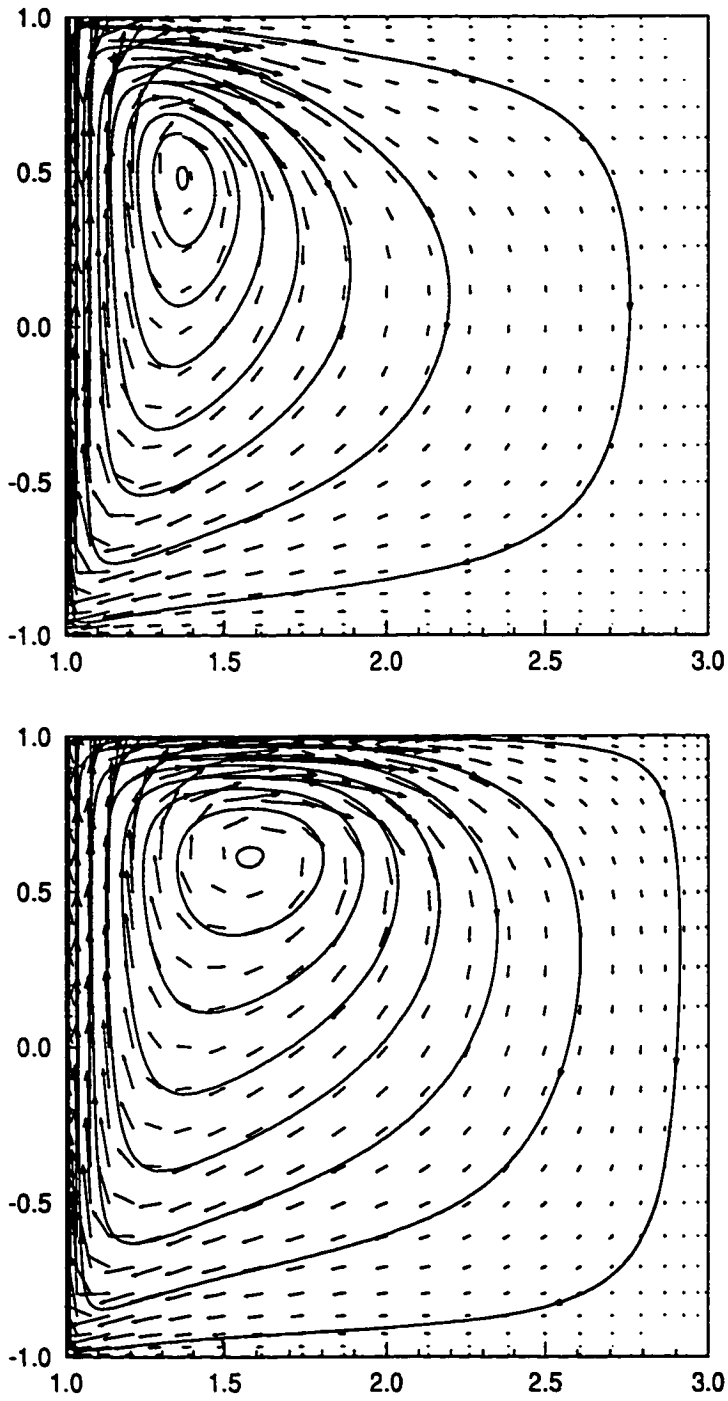

Figure 5.4: Steady-state flow in a cylindrical cavity, driven by inner cylinder: (top) wall at all boundaries; (bottom) *free-slip* wall on top. $Re = 200$ and $t = 3.0$.

Reproduced with permission of the copyright owner. Further reproduction prohibited without permission. www.manaraa.com

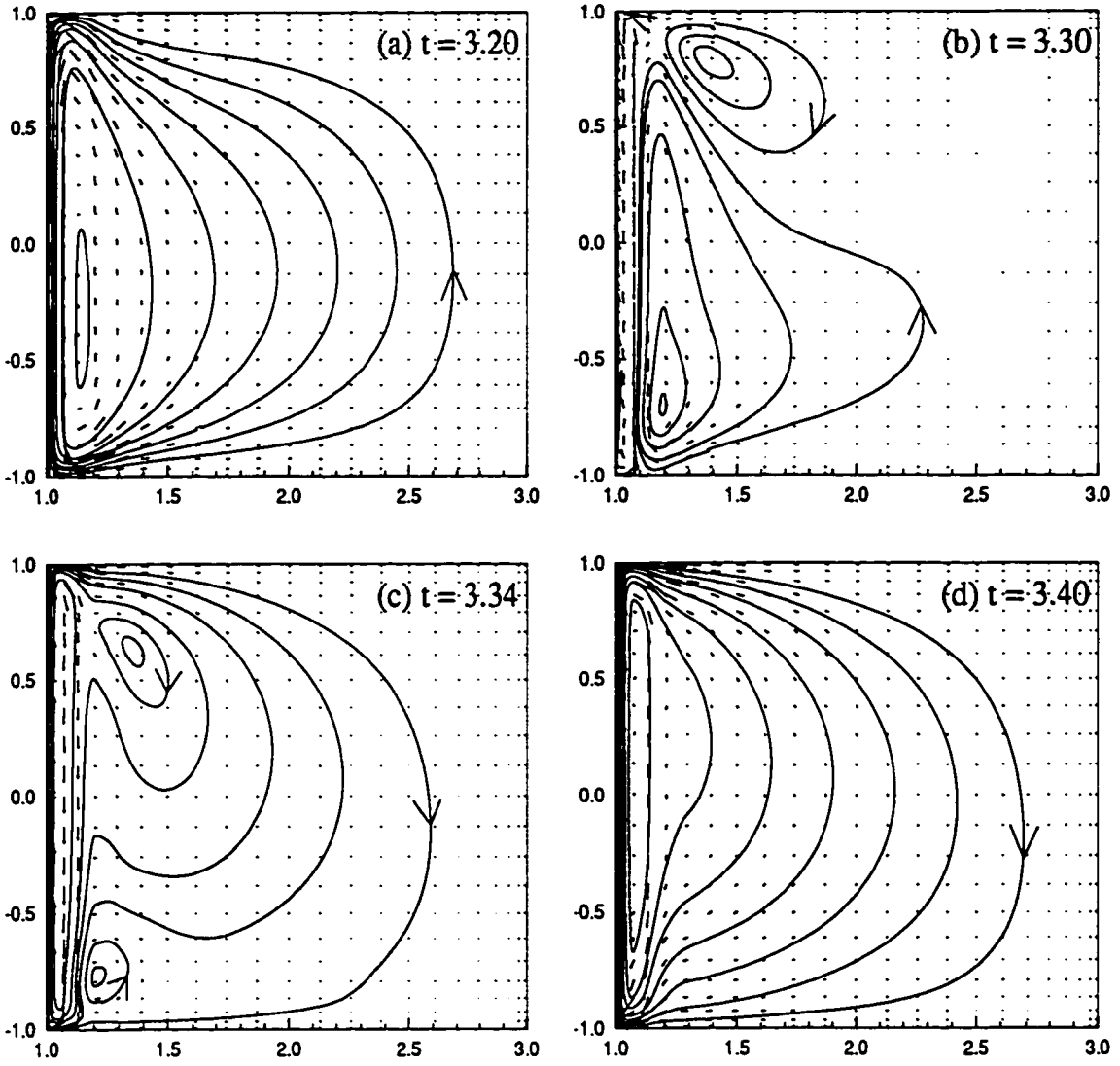

Figure 5.5: Cylindrical cavity flow driven by an oscillatory wall, free-slip wall on top: (a) $t = 4T$; (b) $t = 4\frac{5}{40}T$; (c) $t = 4\frac{7}{40}T$; (d) $t = 4\frac{10}{40}T$, where T is the period of oscillation.

Reproduced with permission of the copyright owner. Further reproduction prohibited without permission. www.manaraa.com

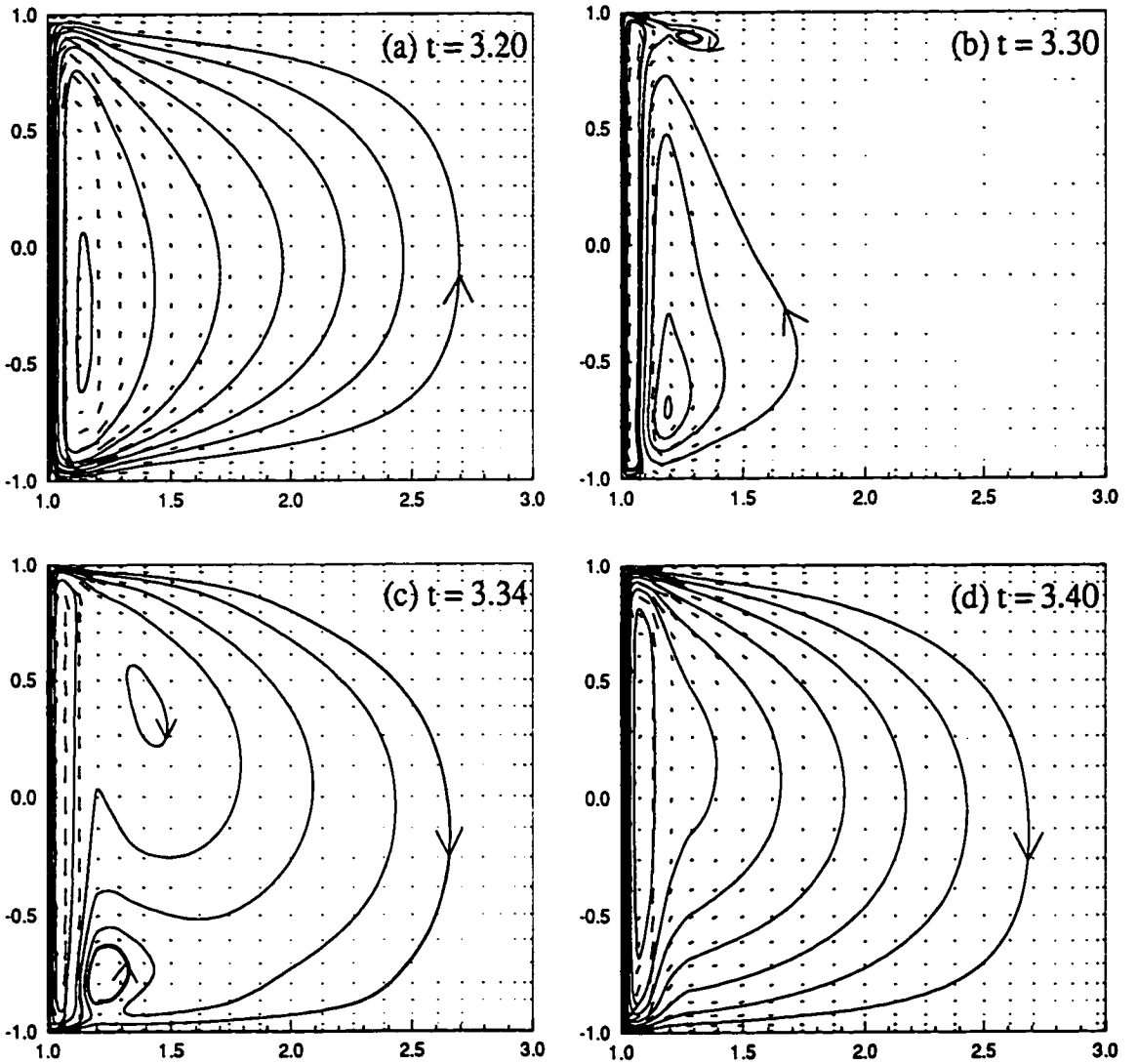

Figure 5.6: Cylindrical cavity flow driven by an oscillatory wall, no-slip walls on all boundaries: (a) $t = 4T$; (b) $t = 4\frac{5}{40}T$; (c) $t = 4\frac{7}{40}T$; (d) $t = 4\frac{10}{40}T$, where T is the period of oscillation.

Reproduced with permission of the copyright owner. Further reproduction prohibited without permission. www.manaraa.com

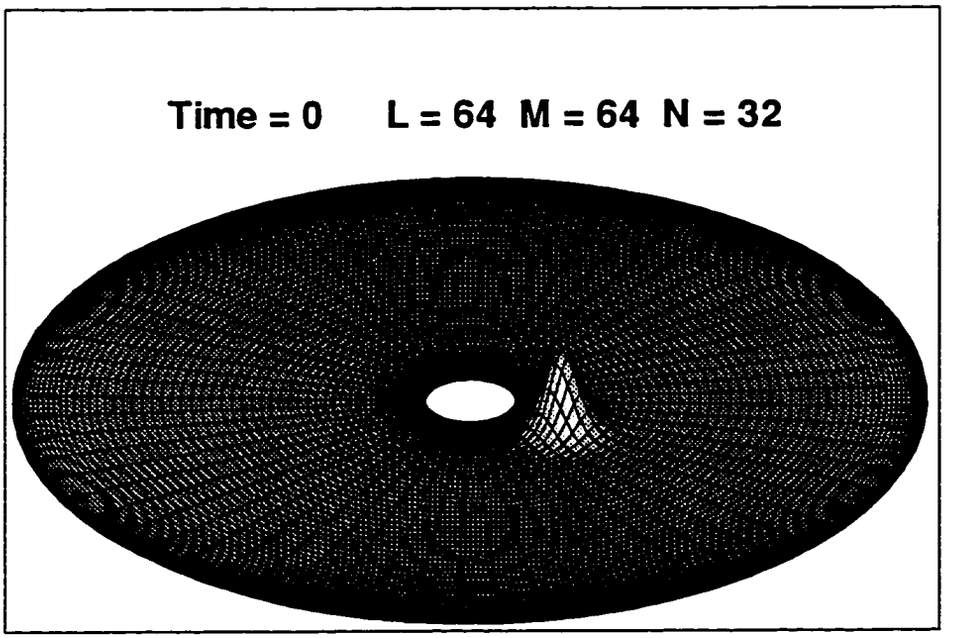

Figure 5.7: The initial free-surface form at $t = 0$. The wave elevation has been enlarged.

Reproduced with permission of the copyright owner. Further reproduction prohibited without permission. www.manaraa.com

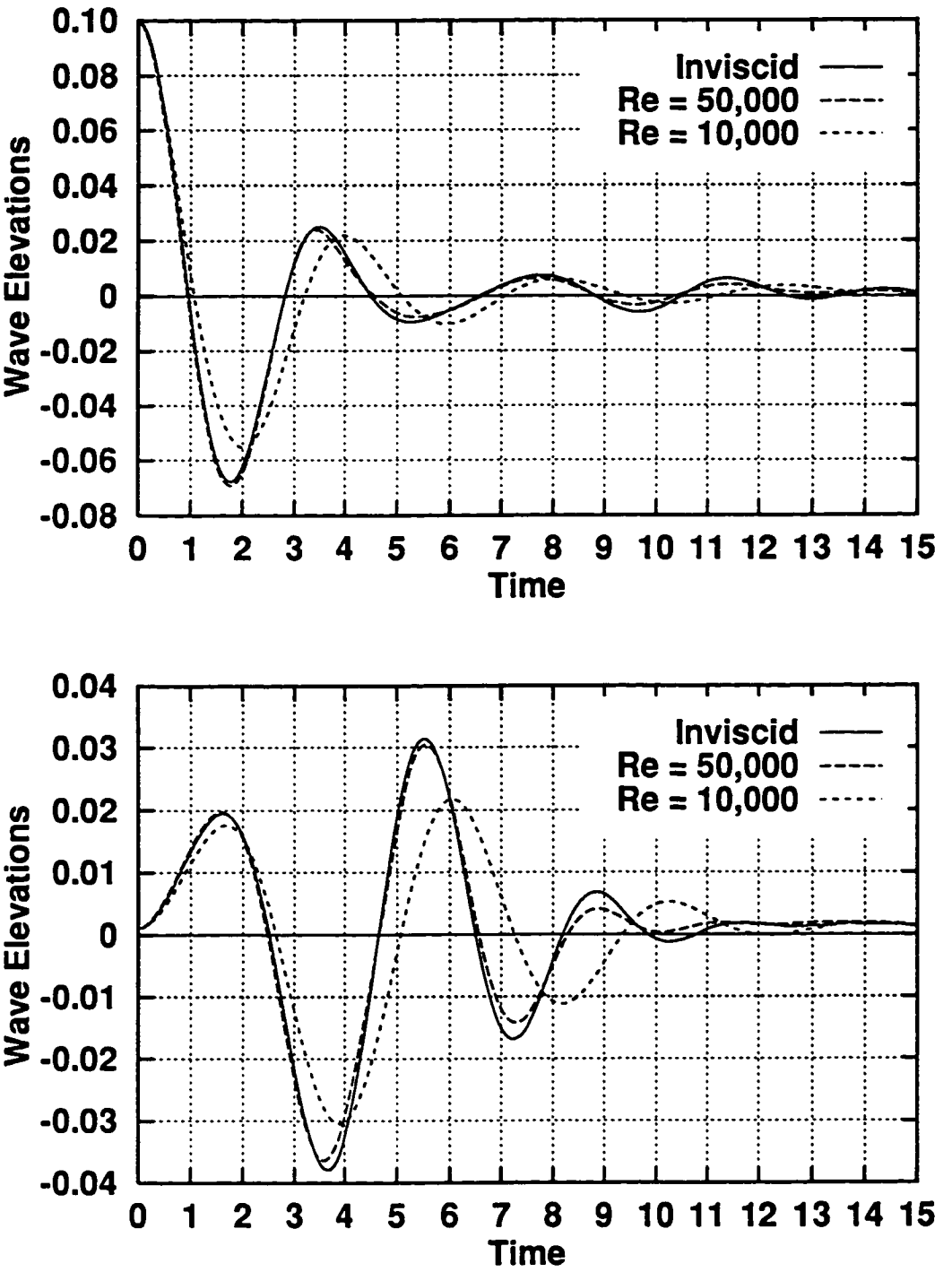

Figure 5.8: Time history of wave elevation at $r = 2.318$ (top) and $r = 1.000$ (bottom), for the plane $\theta = 0$.

Reproduced with permission of the copyright owner. Further reproduction prohibited without permission. www.manaraa.com

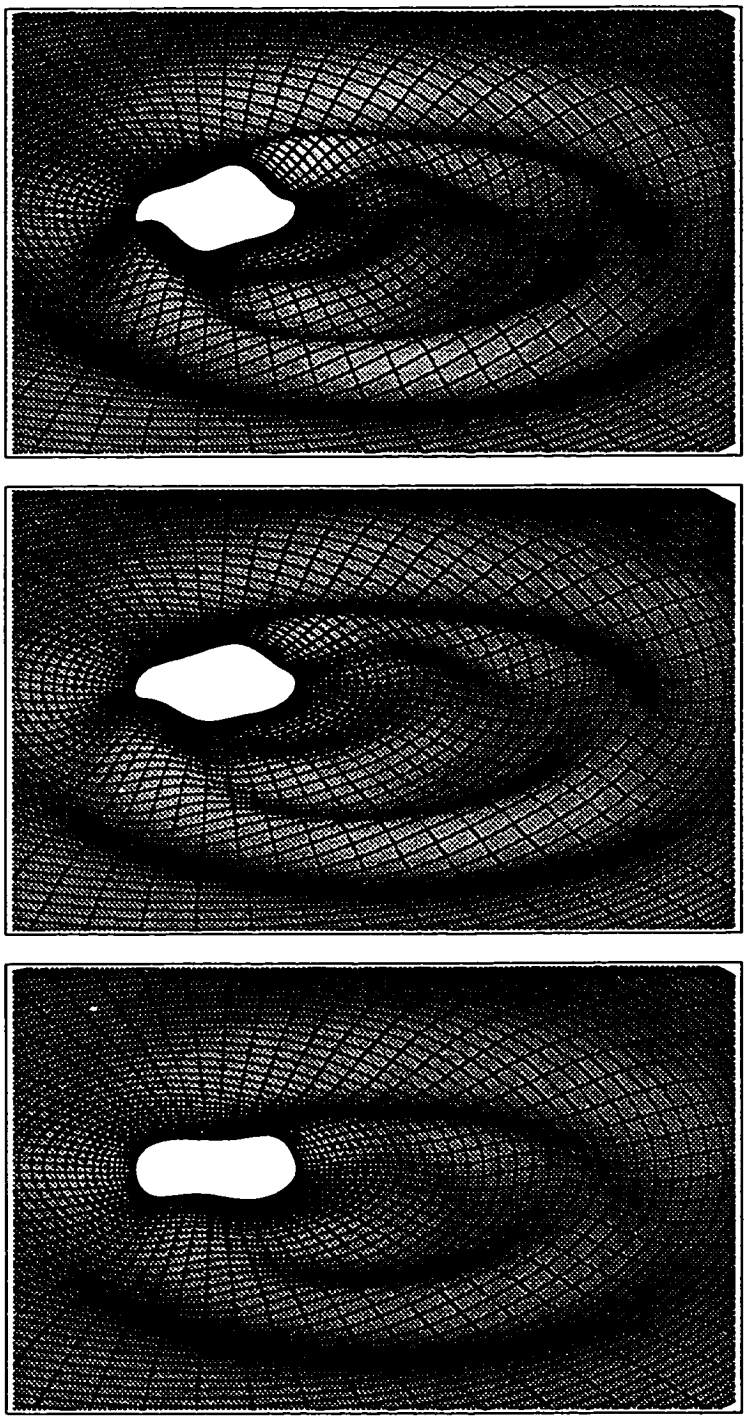

Figure 5.9: Free-surface elevations for the cases of inviscid flow (top), and viscous flows with $Re = 50,000$ (middle) and $Re = 10,000$ (bottom) at $t = 12.000$. The elevations have been enlarged for clarity.

Reproduced with permission of the copyright owner. Further reproduction prohibited without permission. www.manaraa.com

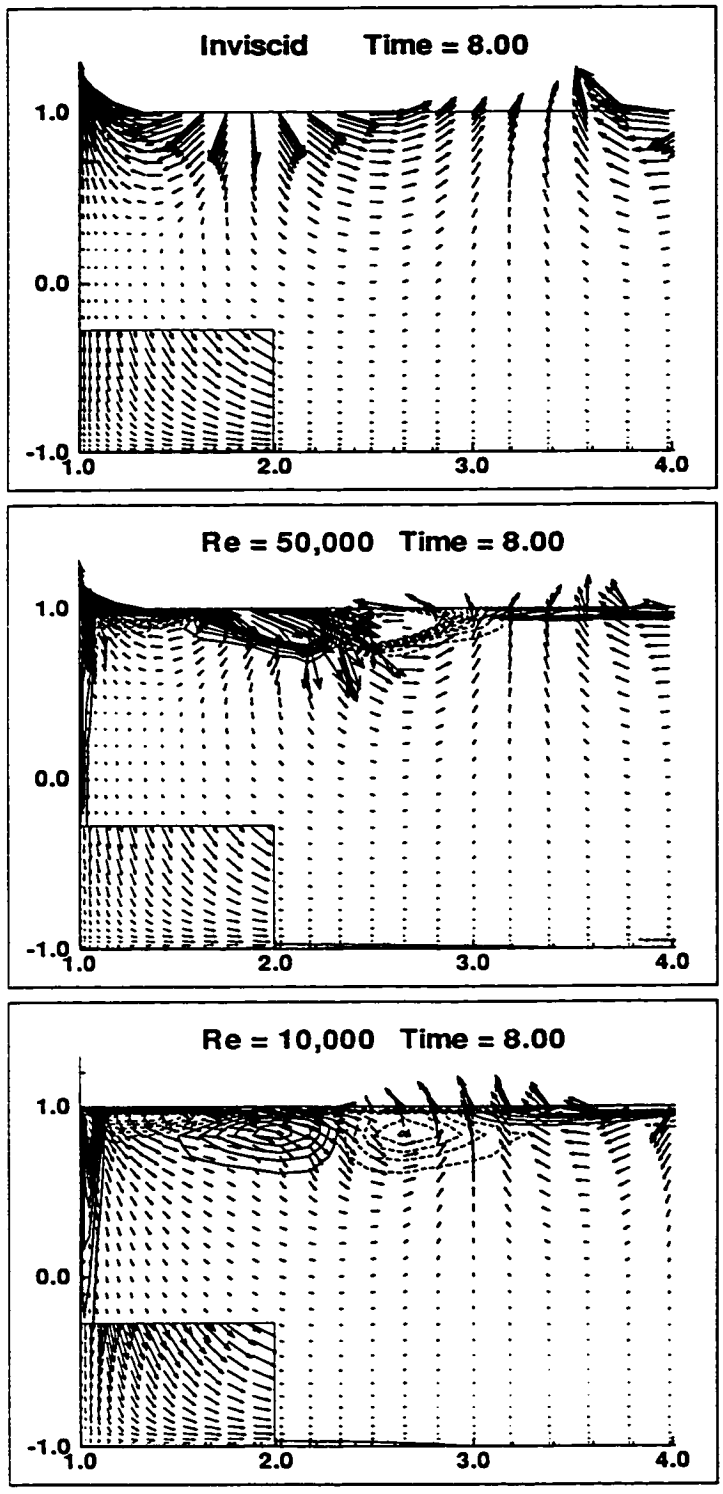

Figure 5.10: Velocity vectors and vorticity contours in the plane $\theta = 0$ for inviscid flow (top), and viscous flows with $Re = 50,000$ (middle) and $Re = 10,000$ (bottom) at $t = 8.000$.

Reproduced with permission of the copyright owner. Further reproduction prohibited without permission. www.manaraa.com

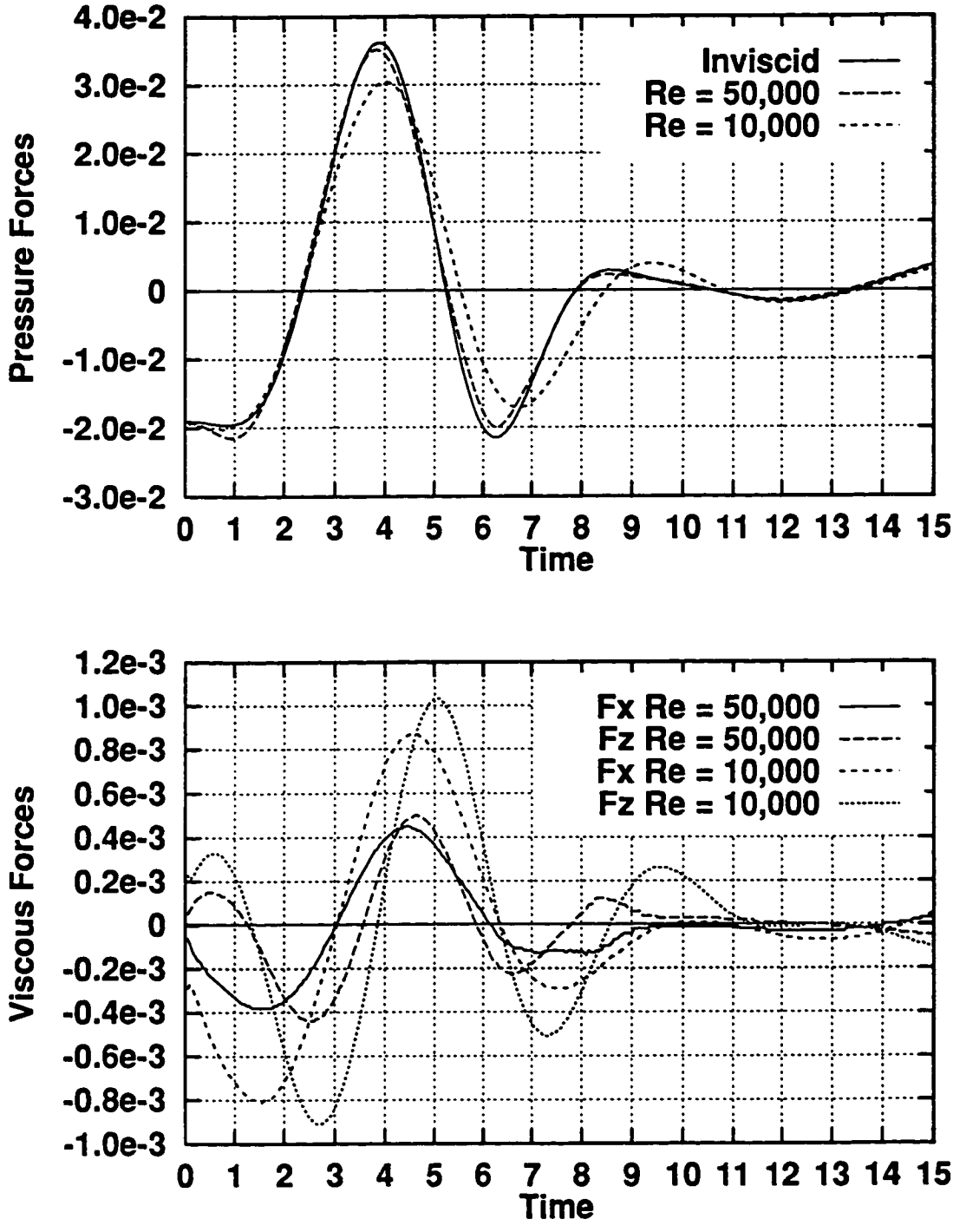

Figure 5.11: Time history of hydrodynamic forces on cylinder.

Reproduced with permission of the copyright owner. Further reproduction prohibited without permission. www.manaraa.com

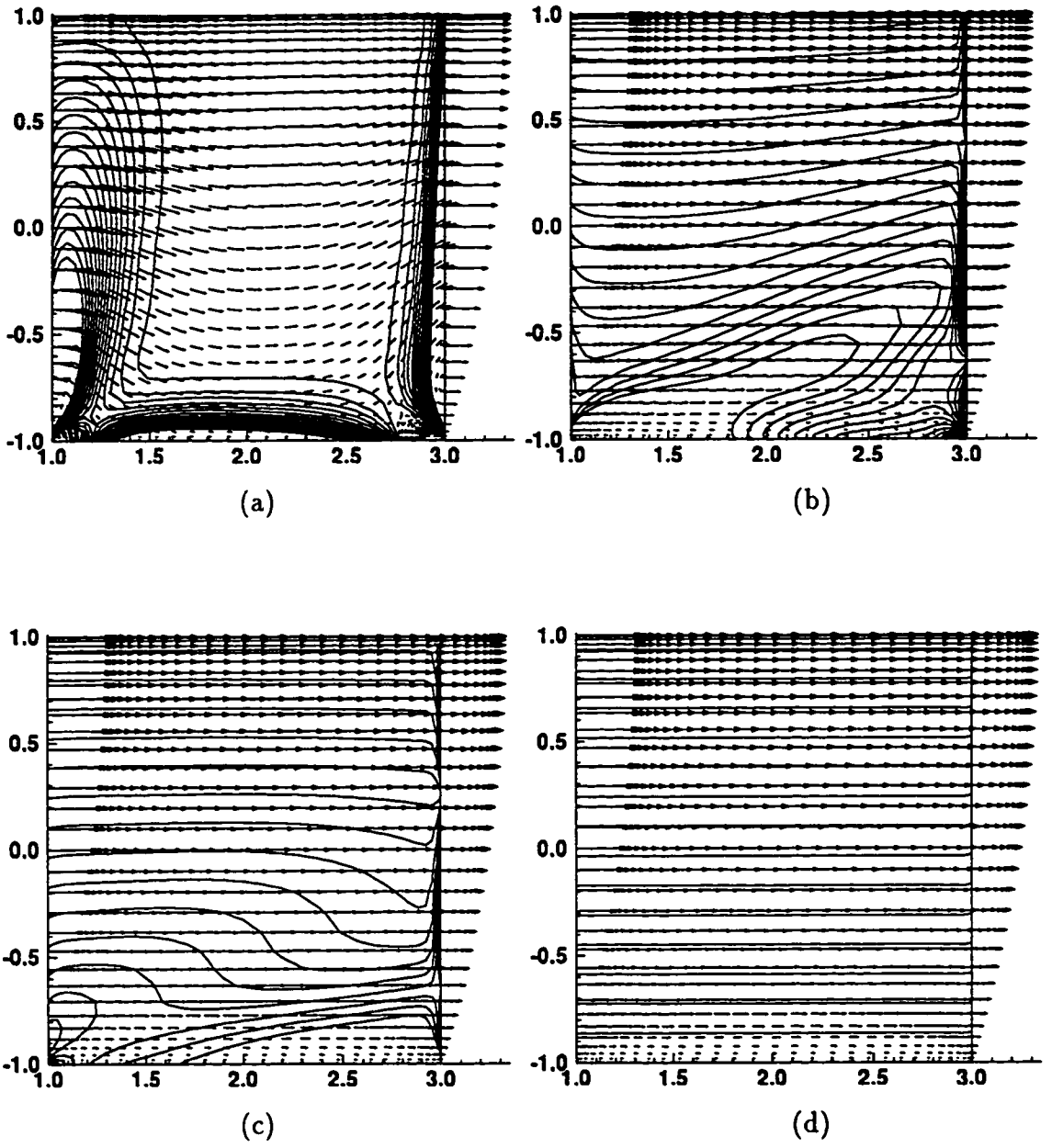

Figure 5.12: Velocity vectors and vorticity contours in the plane $\theta = 0$ at $t = 1.00$ (a), $t = 5.00$ (b), $t = 10.00$ (c) and $t = 25.00$ (d).

Reproduced with permission of the copyright owner. Further reproduction prohibited without permission. www.manaraa.com

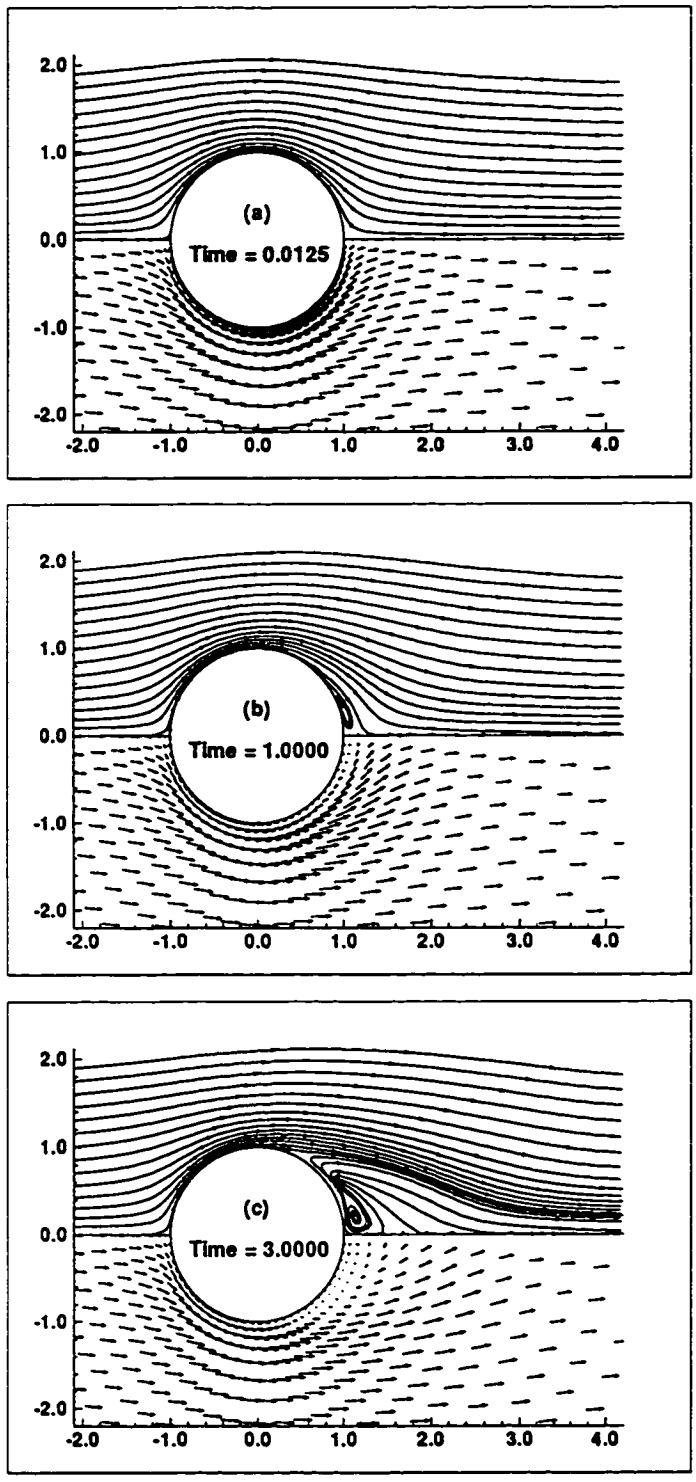

Figure 5.13: Velocity vectors and pathlines on the free-slip surface for $t = 0.0125, 1.0000$ and 3.0000 (only one-fourth of the velocity vectors are shown).

Reproduced with permission of the copyright owner. Further reproduction prohibited without permission. www.manaraa.com

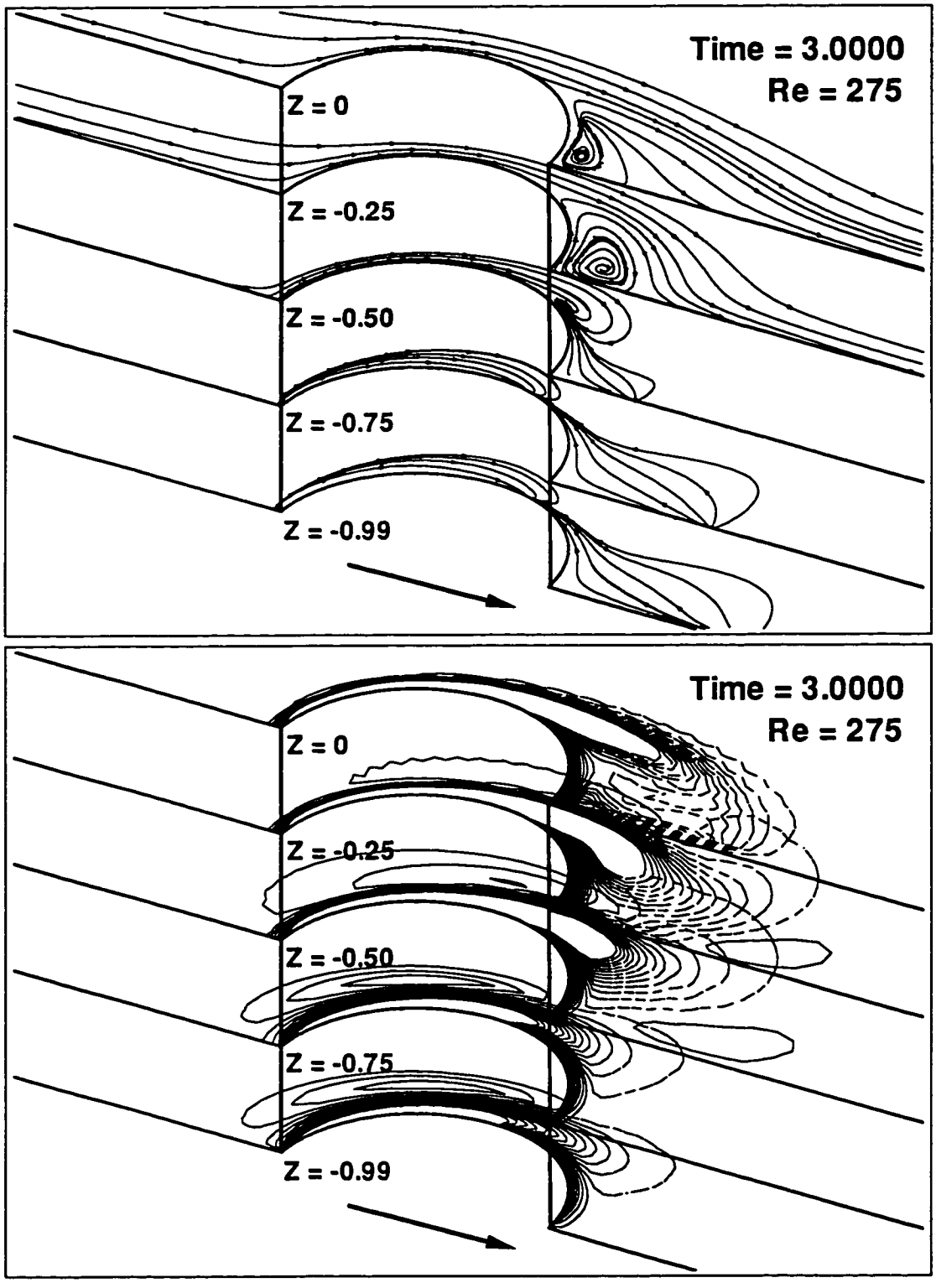

Figure 5.14: Pathlines (top) and vorticity contours (bottom) in horizontal planes for $t = 3.0000$. The z-direction vorticity is shown between -2.5 and 2.5 with increment of 0.2. Dashlines present negative values.

Reproduced with permission of the copyright owner. Further reproduction prohibited without permission. www.manaraa.com

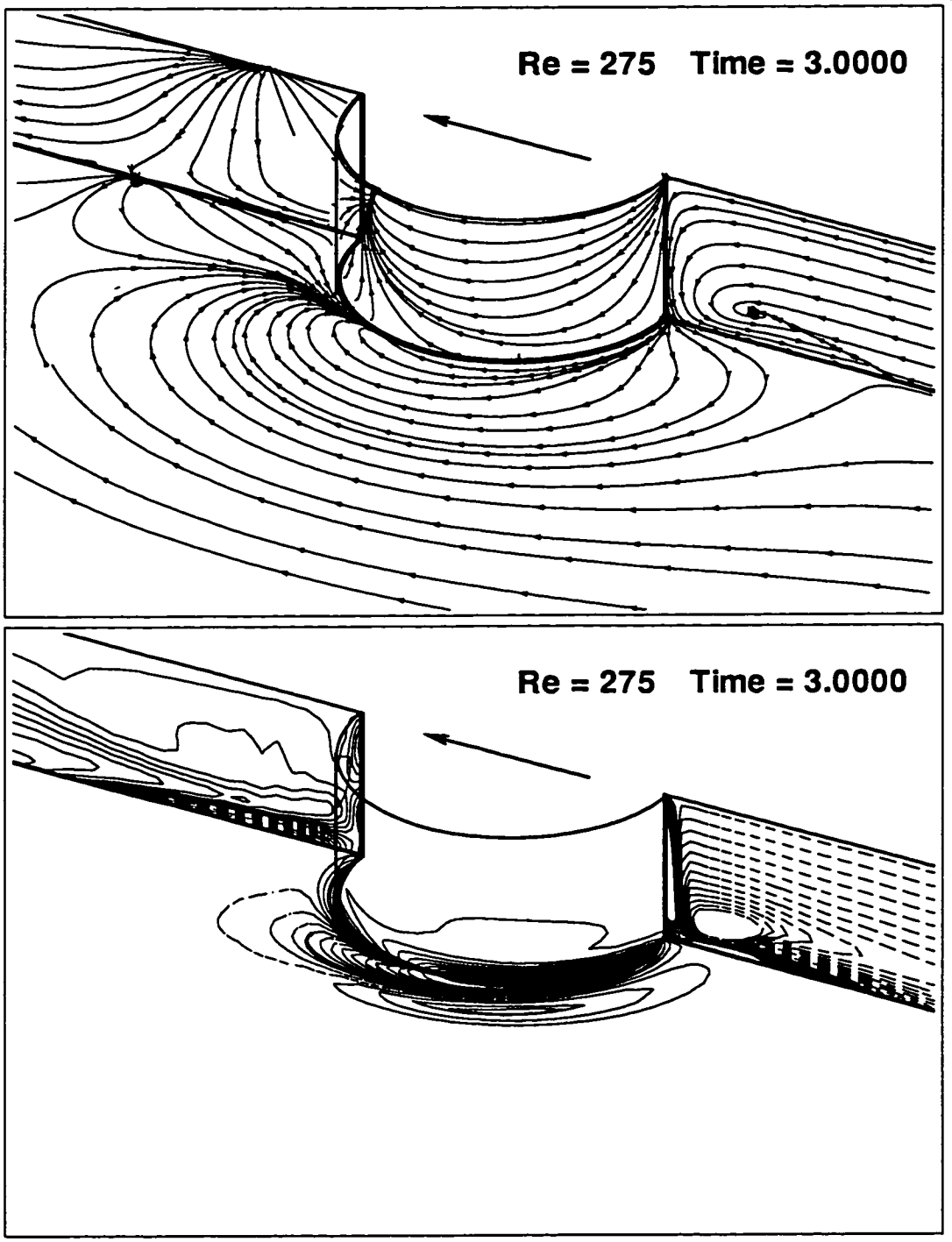

Figure 5.15: Pathlines (top) and vorticity contours (bottom) in vertical planes $\theta = 0$ and π, cylindrical surface $r = 1.019$ and horizontal plane $z = -0.991$. The θ-, r- and z-direction vorticity contoures are shown in vertical plane, on cylindrical surface and in the horizontal plane, respectively. The vorticity contours shown are between -2.5 and 2.5 with increment of 0.2. Dashlines present negative values.

Reproduced with permission of the copyright owner. Further reproduction prohibited without permission. www.manaraa.com

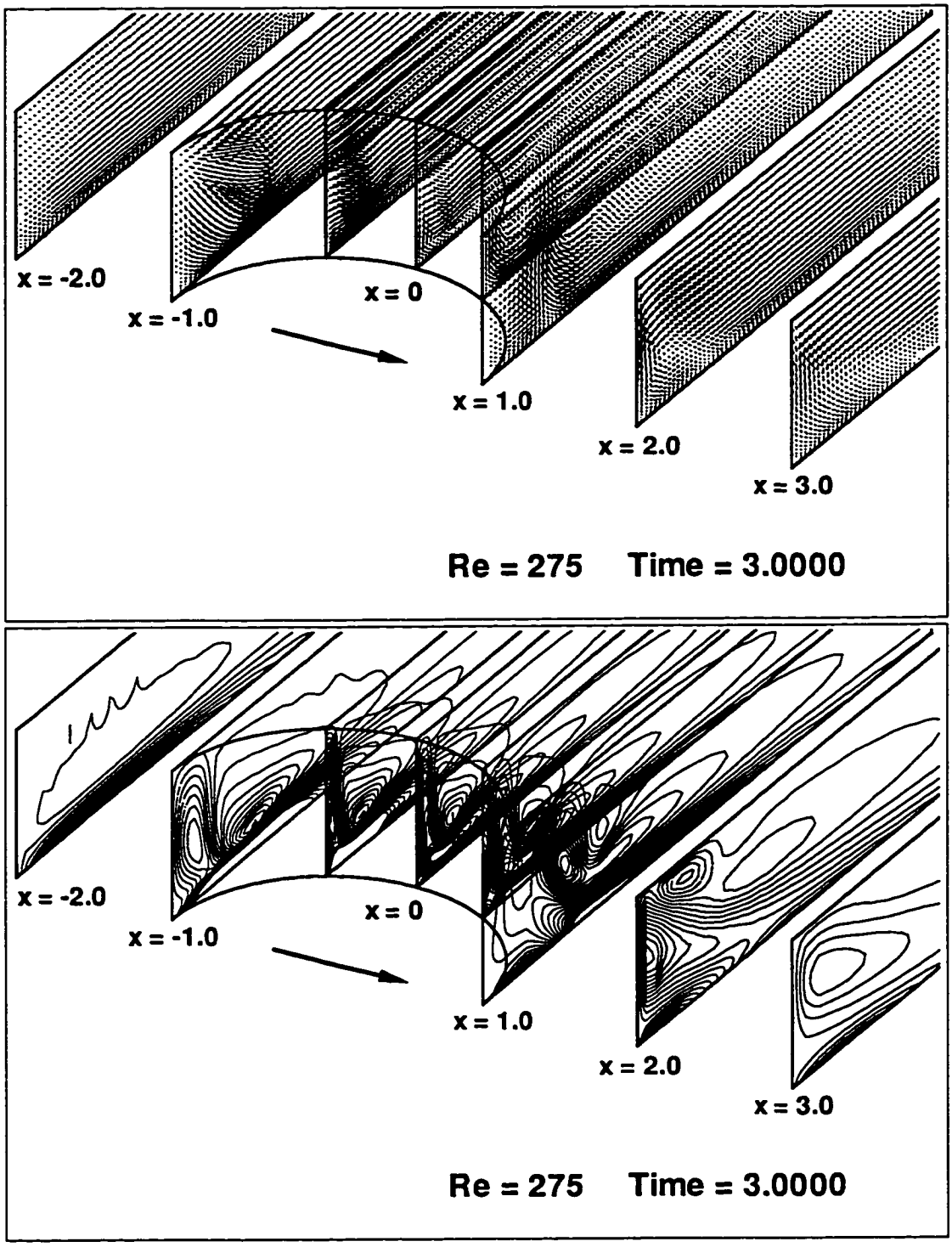

Figure 5.16: Velocity Vectors (top) and vorticity contours (bottom) in transverse planes at $x = -2.0, -1.0, -0.5, 0, 0.5, 1.0, 2.0$ and 3.0. The y-direction velocity and x-direction vorticity are shown. The vorticity contours shown are between -2.5 and 2.5 with increment of 0.2.

Reproduced with permission of the copyright owner. Further reproduction prohibited without permission. www.manaraa.com

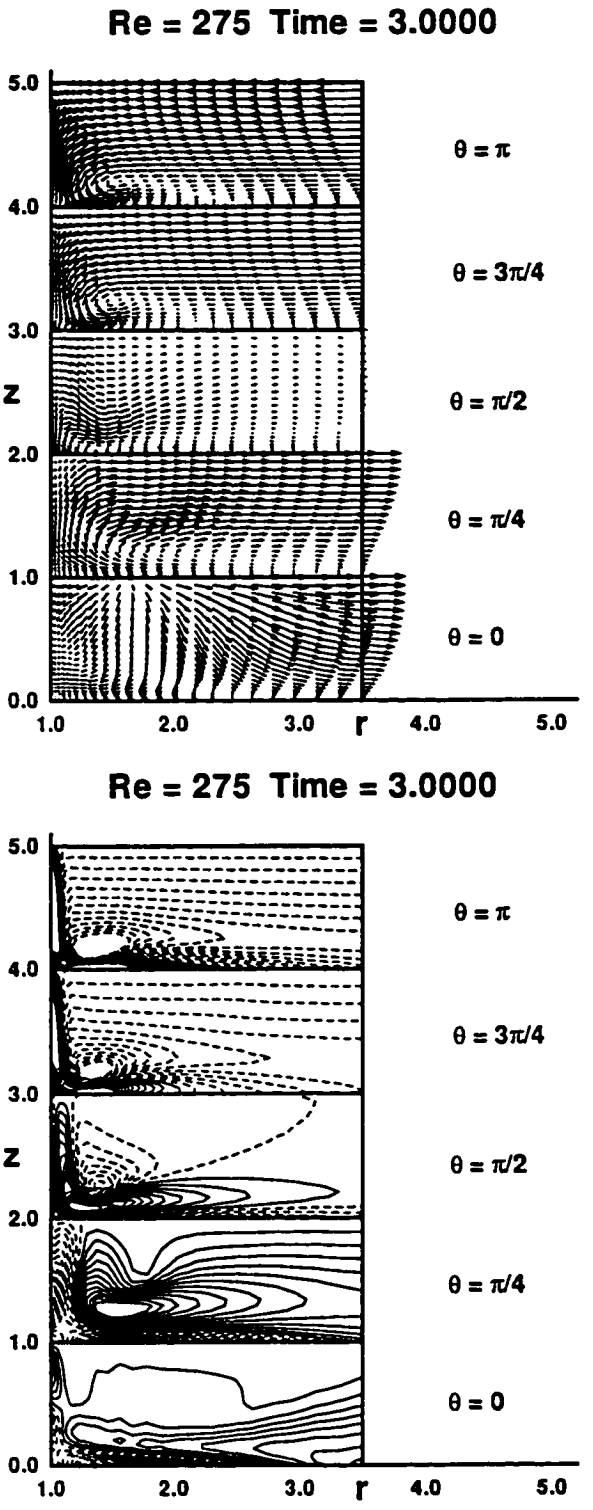

Figure 5.17: Velocity vectors (top) and vorticity contours (bottom) in radial planes. The r-direction velocity and θ-direction vorticity are shown. The vorticity contours shown are between -2.5 and 2.5 with increment of 0.2.

Reproduced with permission of the copyright owner. Further reproduction prohibited without permission. www.manaraa.com

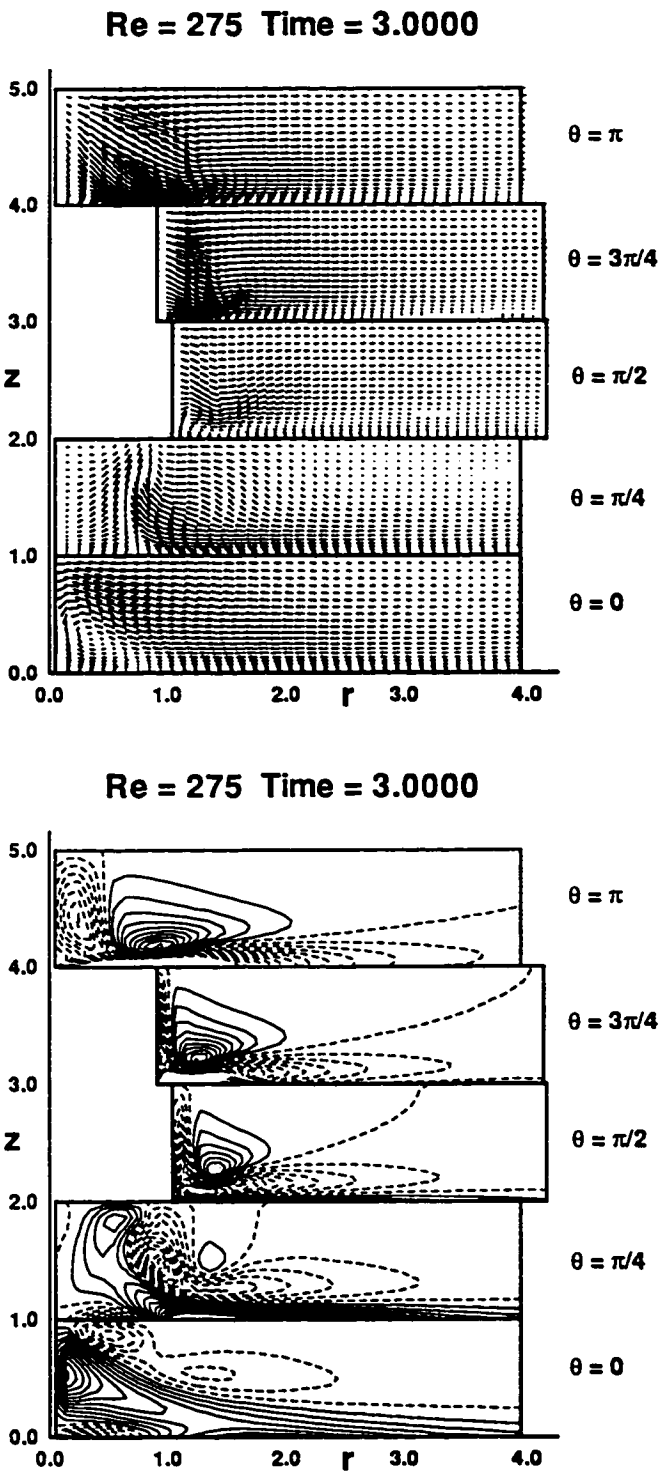

Figure 5.18: Velocity vectors (top) and vorticity contours (bottom) in transverse planes. The y-direction velocity and x-direction vorticity are shown. The vorticity contours shown are between -2.5 and 2.5 with increment of 0.2.

Reproduced with permission of the copyright owner. Further reproduction prohibited without permission. www.manaraa.com

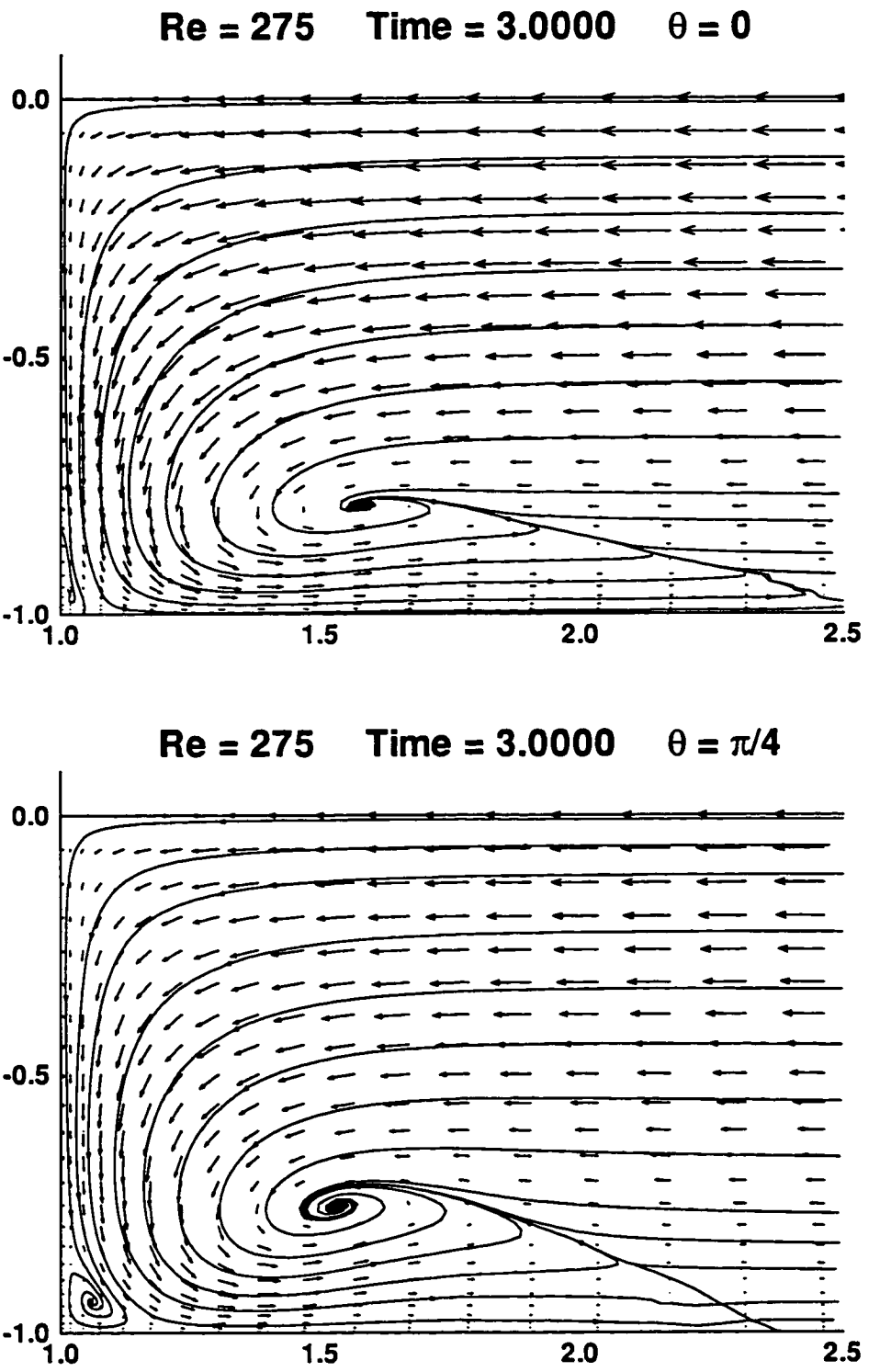

Figure 5.19: Magnified views of velocity vectors and pathlines in two radial planes at $\theta = 0$ (top) and $\pi/4$ (bottom).

Reproduced with permission of the copyright owner. Further reproduction prohibited without permission. www.manaraa.com

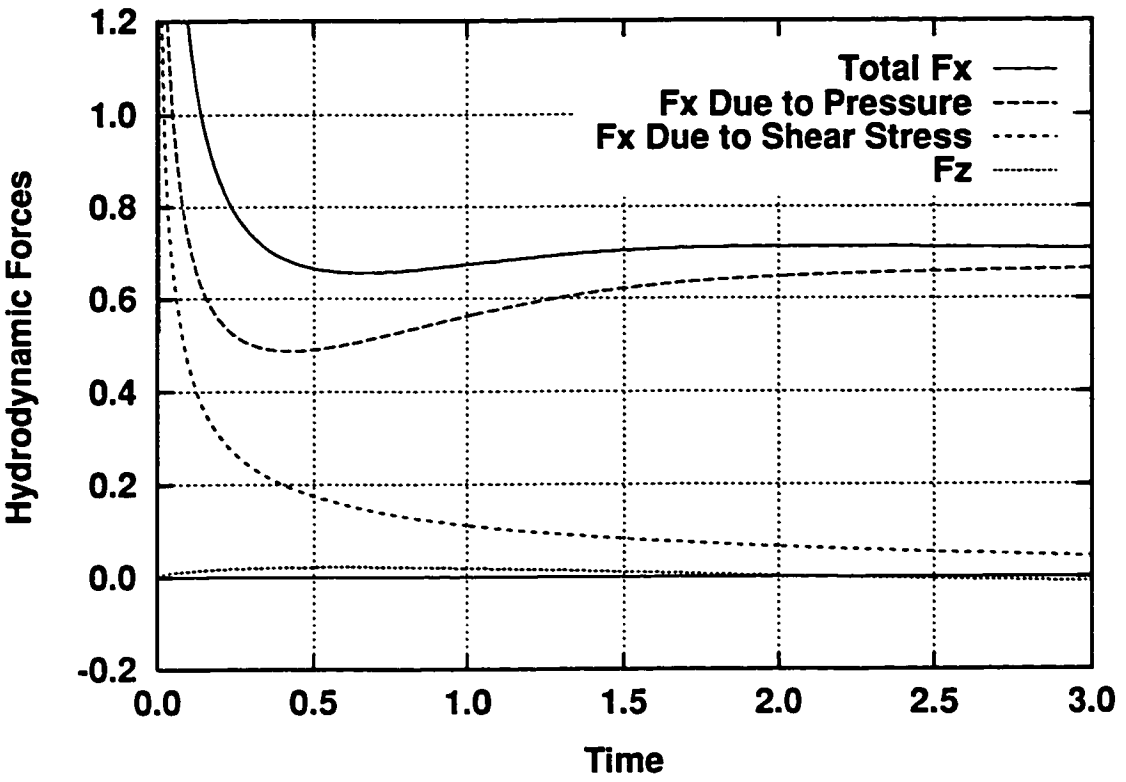

Figure 5.20: Time history of hydrodynamic forces on cylinder.

Reproduced with permission of the copyright owner. Further reproduction prohibited without permission. www.manaraa.com

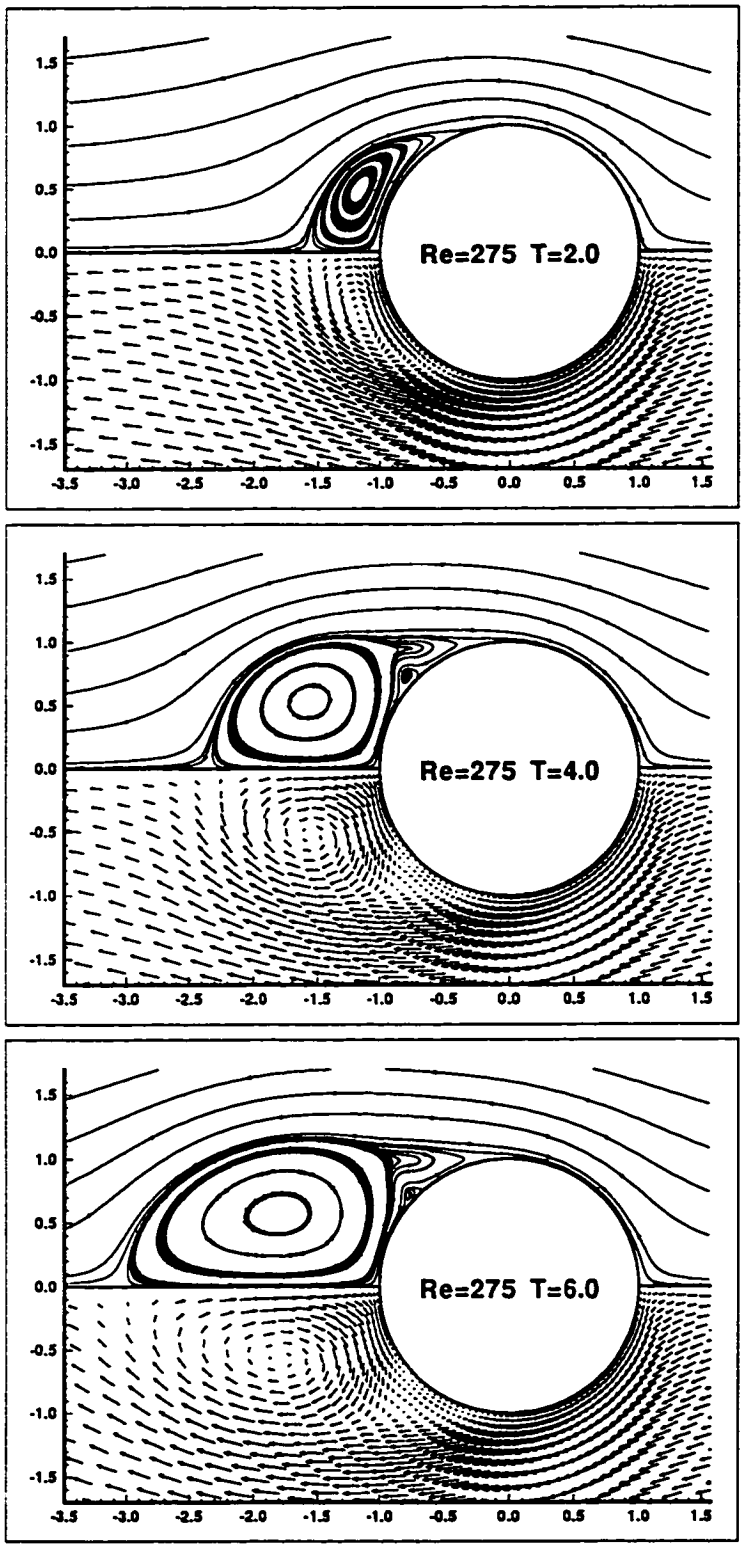

Figure 5.21: Pathlines and velocity vectors for two-dimensional flow around an impulsively started cylinder at $Re = 275$.

Reproduced with permission of the copyright owner. Further reproduction prohibited without permission. www.manaraa.com

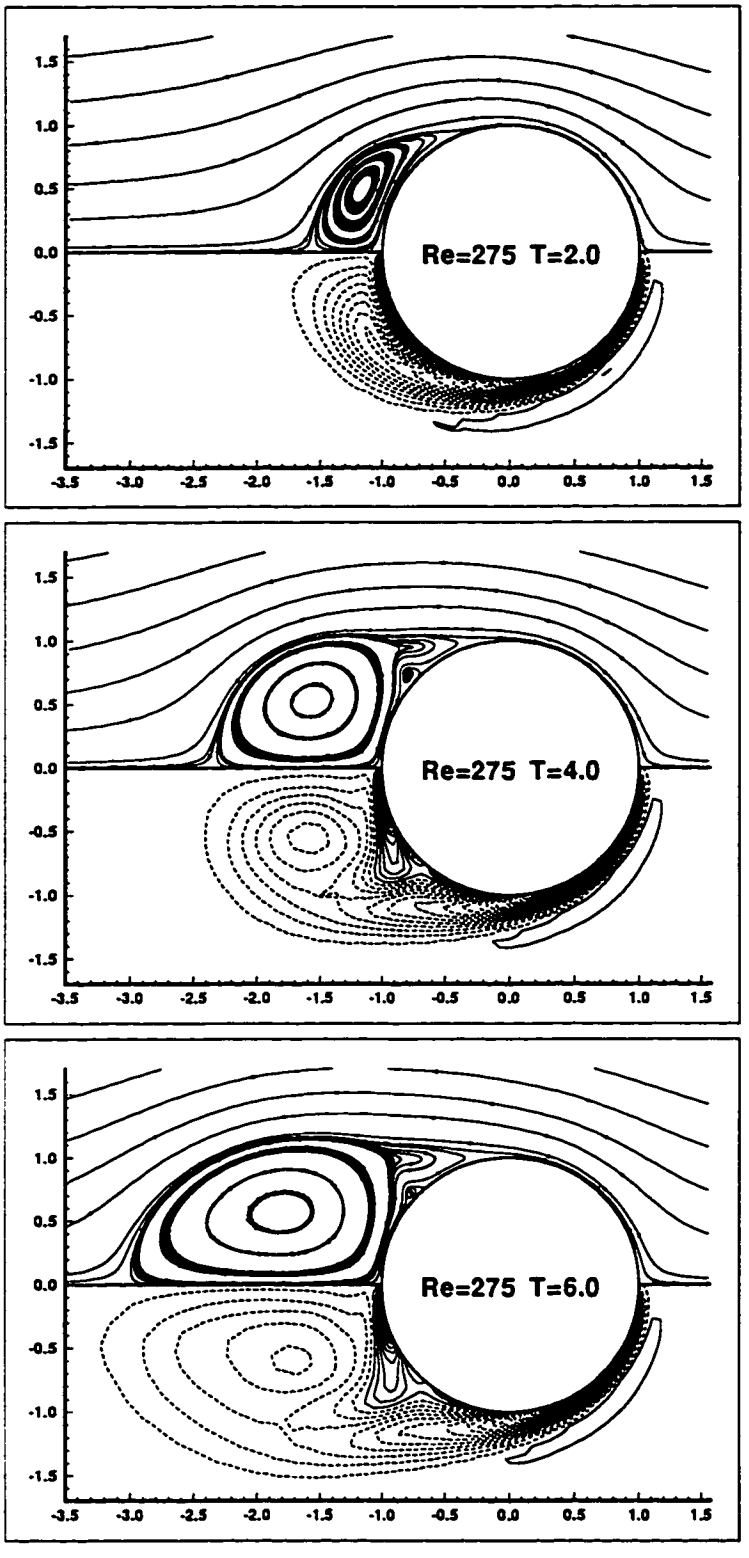

Figure 5.22: Pathlines and vorticity contours for two-dimensional flow around an impulsively started cylinder at $Re = 275$. Contour values equal $-22.0(0.825)11.000$.

Reproduced with permission of the copyright owner. Further reproduction prohibited without permission. www.manaraa.com

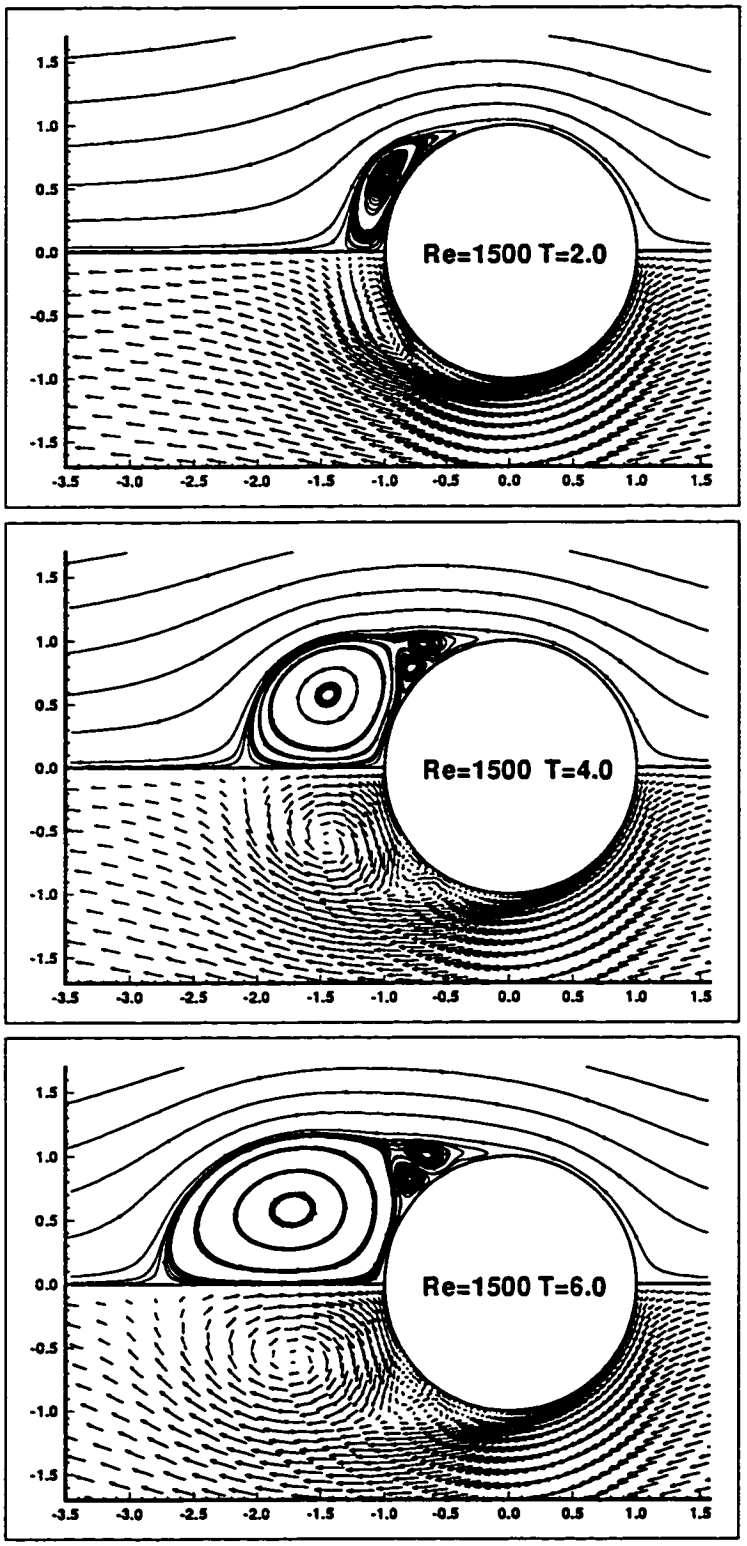

Figure 5.23: Pathlines and velocity vectors for two-dimensional flow around an impulsively started cylinder at $Re = 1500$.

Reproduced with permission of the copyright owner. Further reproduction prohibited without permission. www.manaraa.com

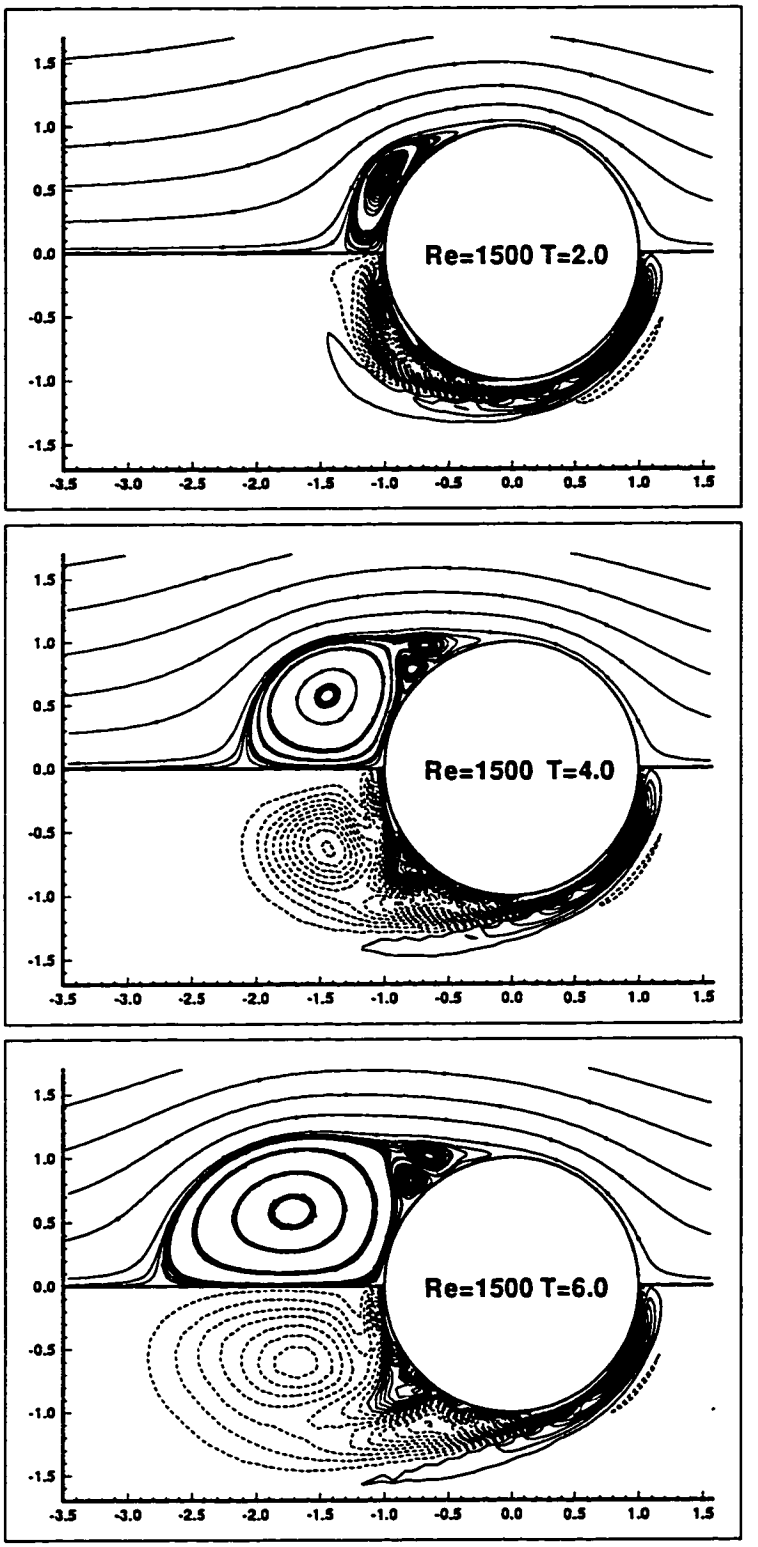

Figure 5.24: Pathlines and vorticity contours for two-dimensional flow around an impulsively started cylinder at $Re = 1500$. Contour values equal $-22.0(0.825)11.000$.

Reproduced with permission of the copyright owner. Further reproduction prohibited without permission. www.manaraa.com

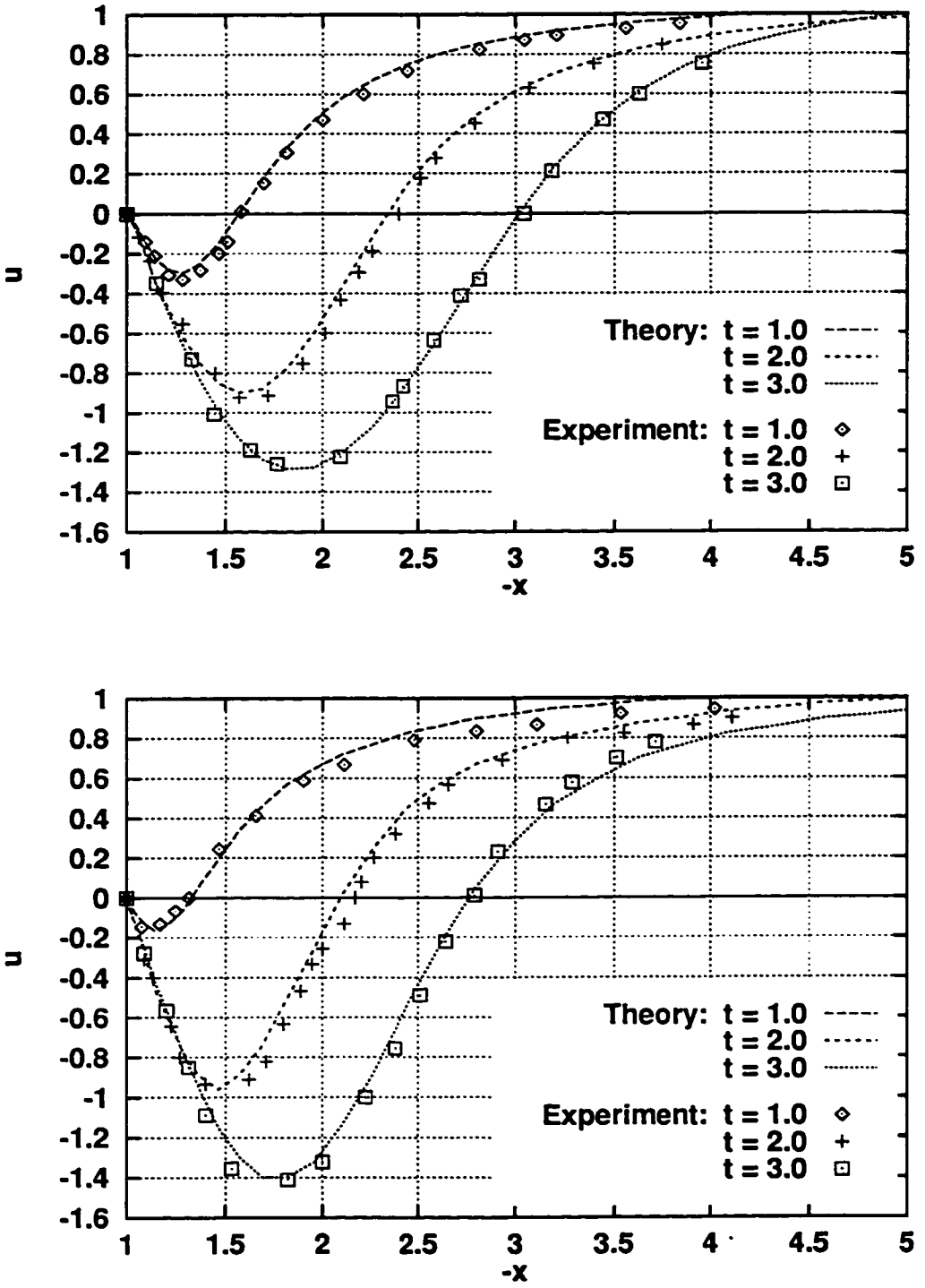

Figure 5.25: Wake velocity for $Re = 275$ (top) and $Re = 1,500$ (bottom). Theory: Current calculation. Experimental: Bouard and Contanceau (1980).

Reproduced with permission of the copyright owner. Further reproduction prohibited without permission. www.manaraa.com

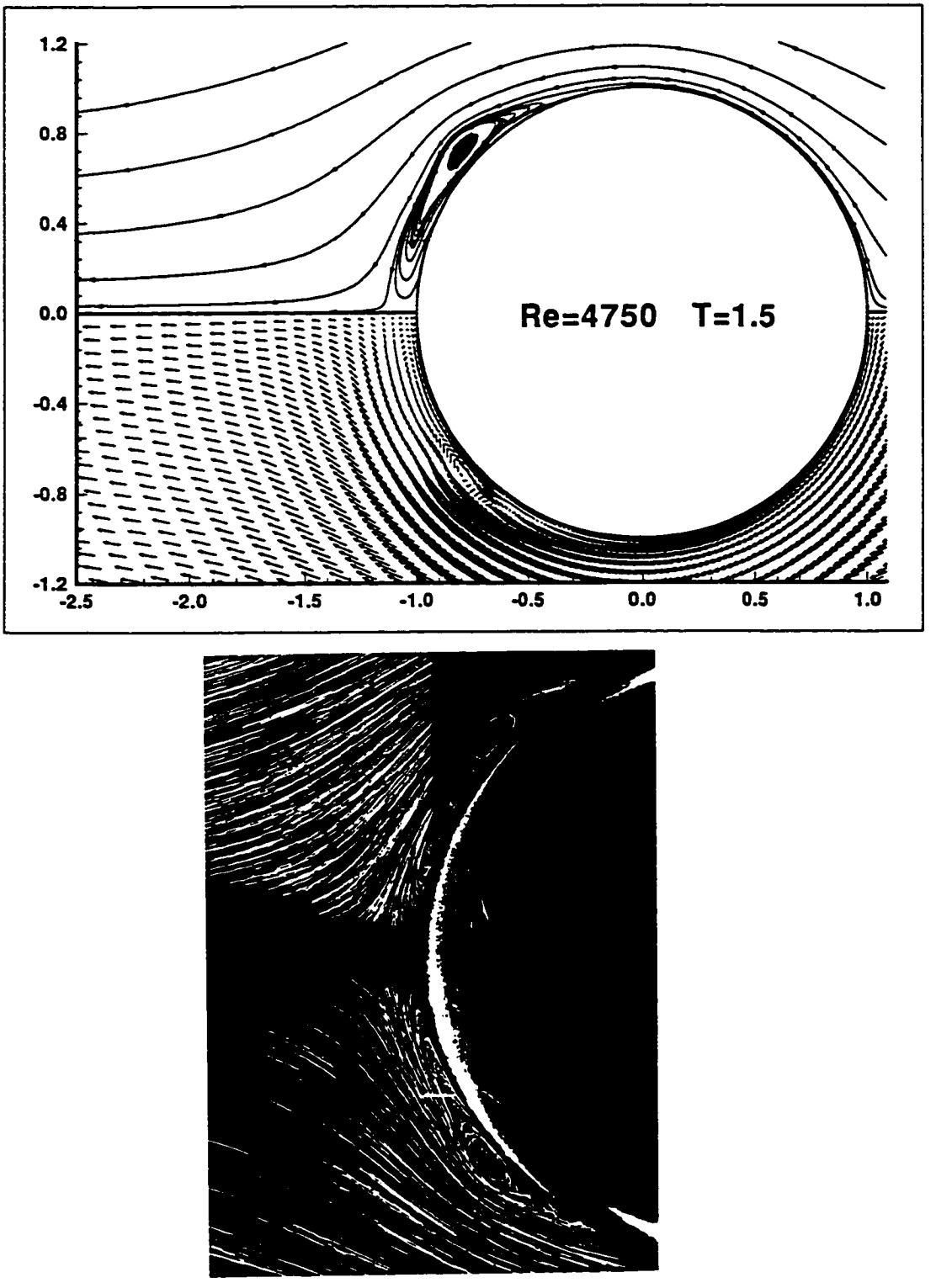

Figure 5.26: Pathlines and vorticity contours (top) and experimental result (Bouard and Contanceau, 1980) (bottom) for $Re = 4750$ at $t = 1.5$.

Reproduced with permission of the copyright owner. Further reproduction prohibited without permission. www.manaraa.com

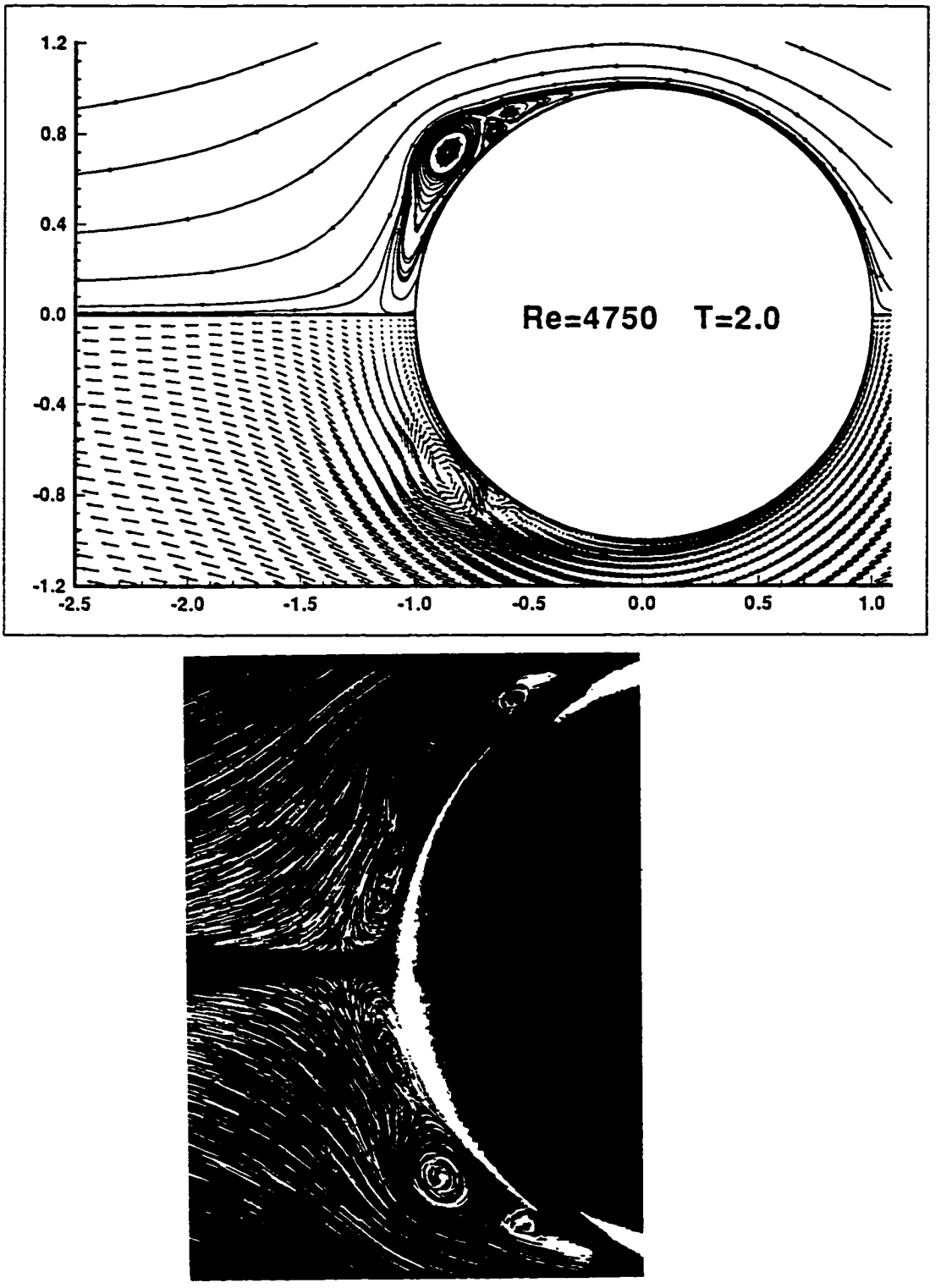

Figure 5.27: Pathlines and vorticity contours (top) and experimental result (Bouard and Contanceau, 1980) (bottom) for $Re = 4750$ at $t = 2.0$.

Reproduced with permission of the copyright owner. Further reproduction prohibited without permission. www.manaraa.com

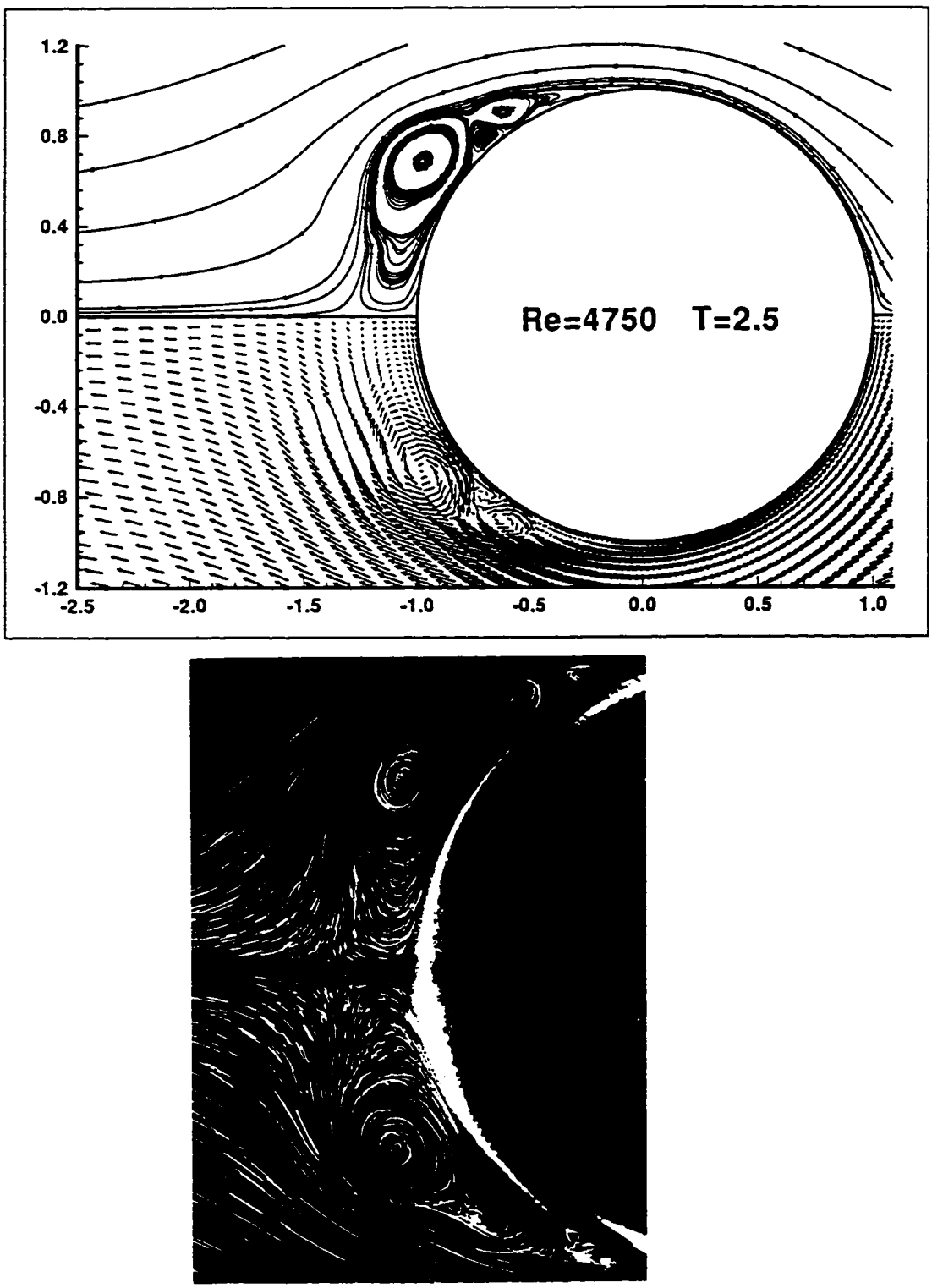

Figure 5.28: Pathlines and vorticity contours (top) and experimental result (Bouard and Contanceau, 1980) (bottom) for $Re = 4750$ at $t = 2.5$.

Reproduced with permission of the copyright owner. Further reproduction prohibited without permission. www.manaraa.com

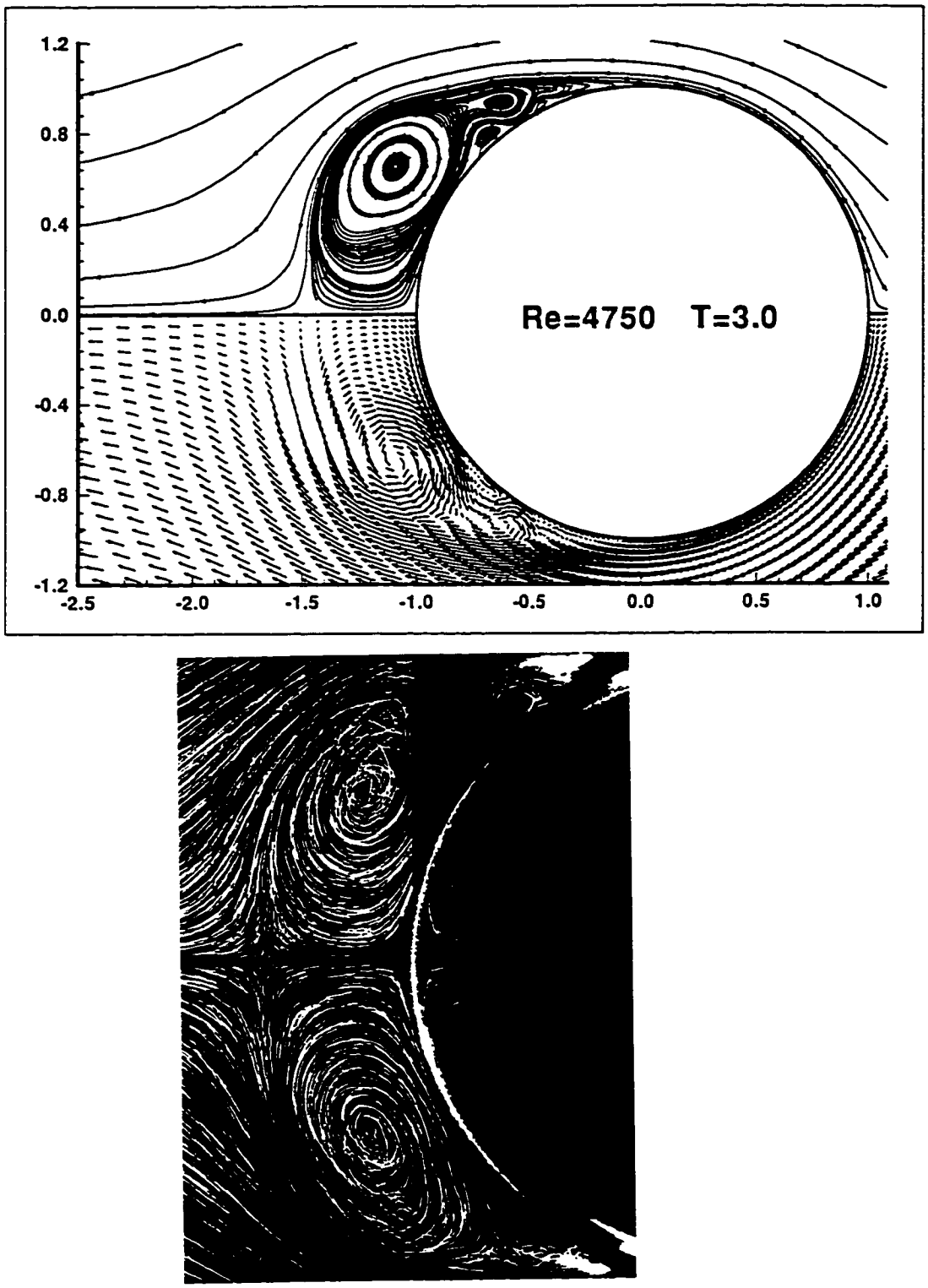

Figure 5.29: Pathlines and vorticity contours (top) and experimental result (Bouard and Contanceau, 1980) (bottom) for $Re = 4750$ at $t = 3.0$.

Reproduced with permission of the copyright owner. Further reproduction prohibited without permission. www.manaraa.com

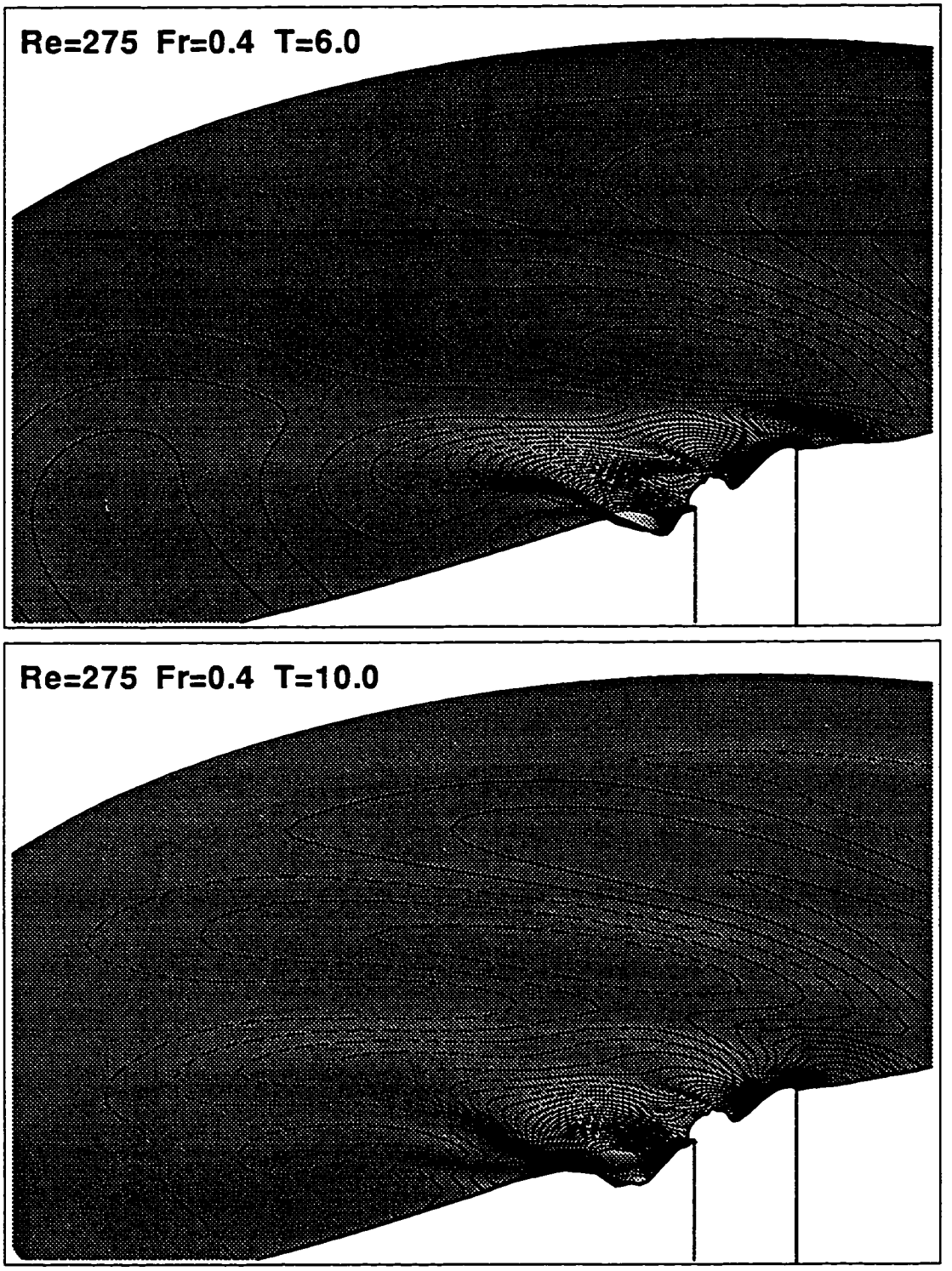

Figure 5.30: Free-Surface perspective views and wave elevation contours for $Re = 275$ and $Fr = 0.4$ at $t = 6.00$ (top) and $t = 10.00$ (bottom). Dashlines present negative elevations.

Reproduced with permission of the copyright owner. Further reproduction prohibited without permission. www.manaraa.com

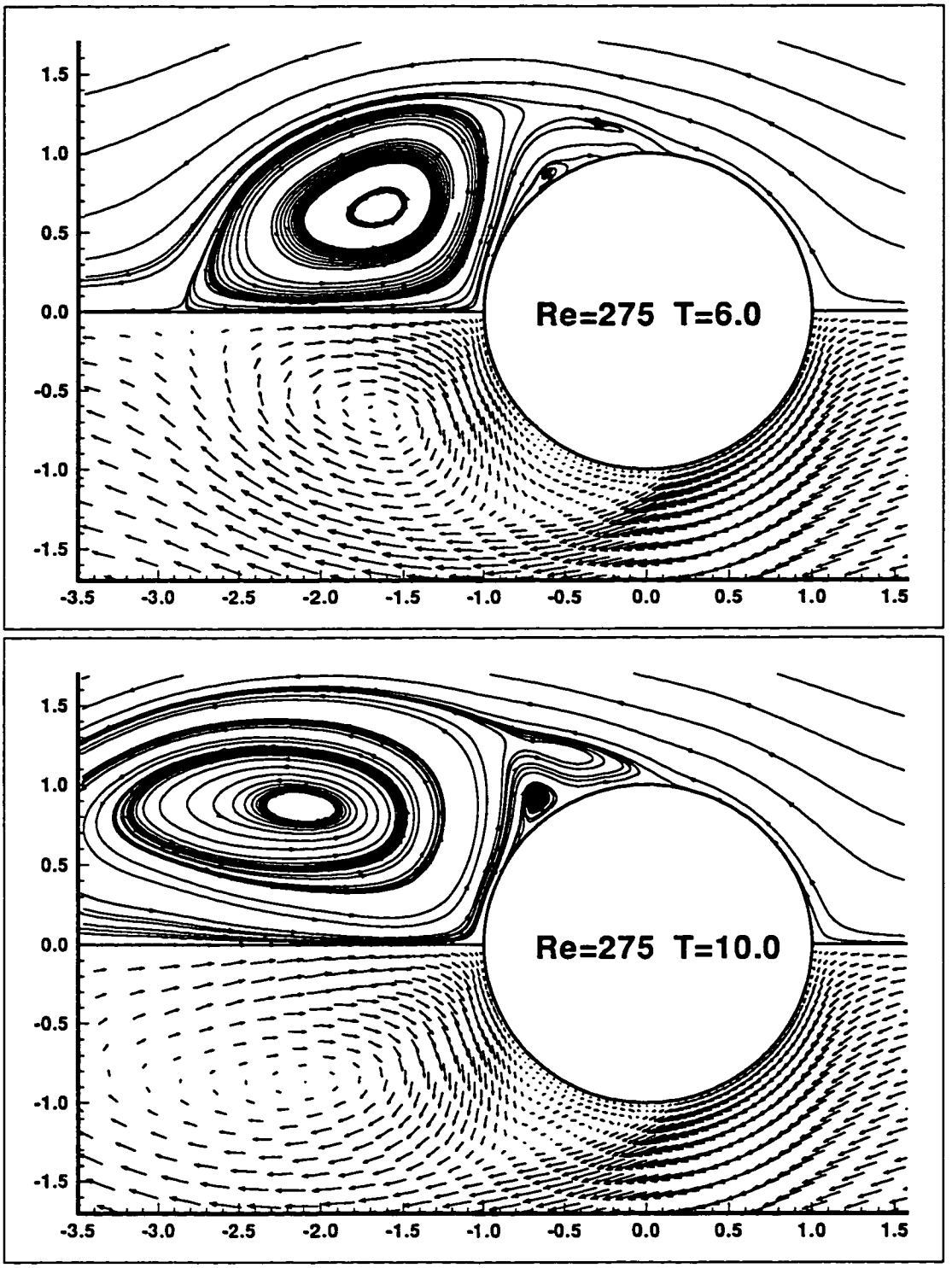

Figure 5.31: Pathlines and velocity vectors on the free surface for $Re = 275$ and $Fr = 0.4$ at $t = 6.00$ (top) and $t = 10.00$ (bottom). Dashlines present negative elevations.

Reproduced with permission of the copyright owner. Further reproduction prohibited without permission. www.manaraa.com

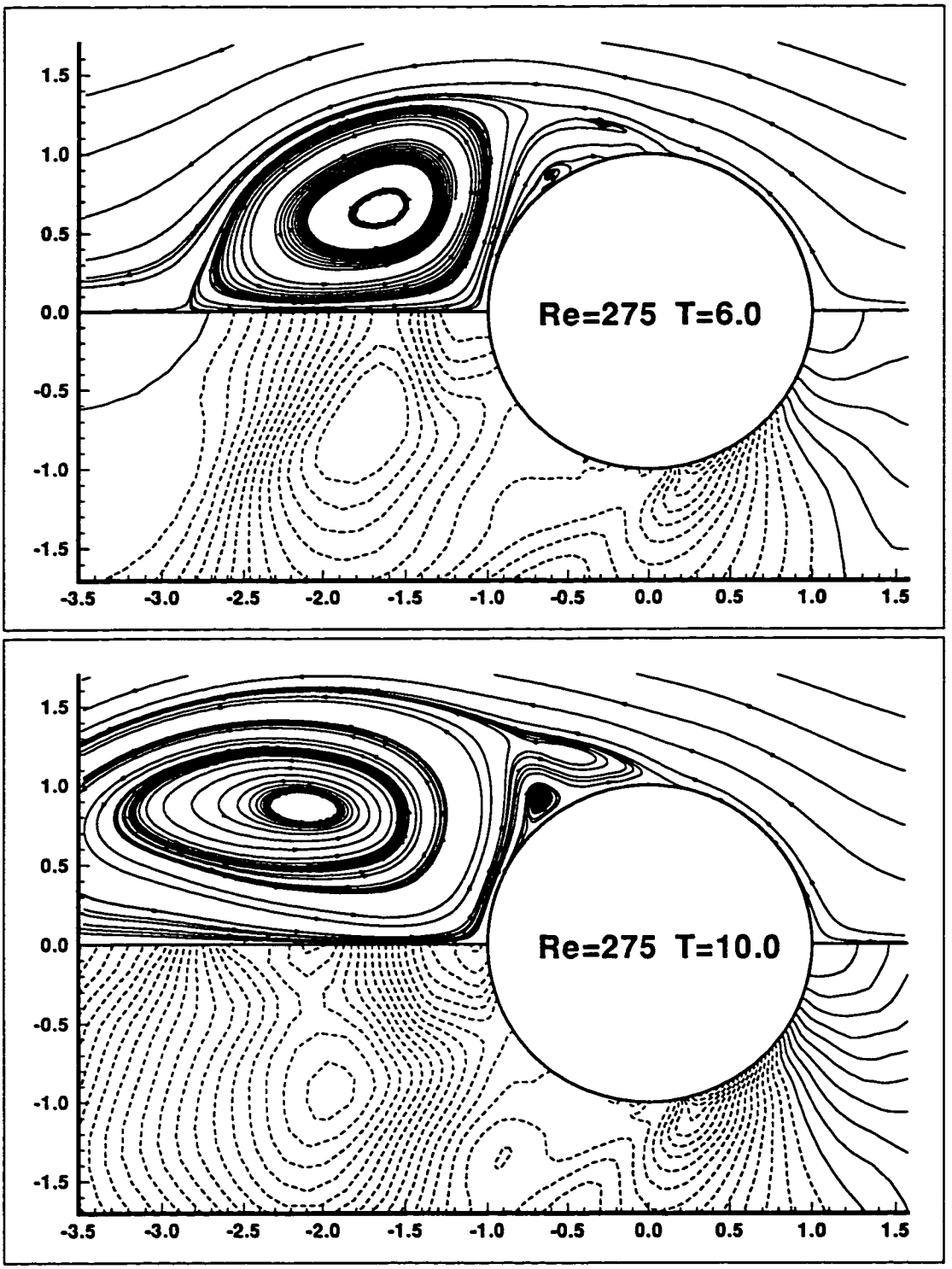

Figure 5.32: Pathlines and wave elevation contours on the free surface for $Re = 275$ and $Fr = 0.4$ at $t = 6.00$ (top) and $t = 10.00$ (bottom). Dashlines present negative elevations.

Reproduced with permission of the copyright owner. Further reproduction prohibited without permission. www.manaraa.com

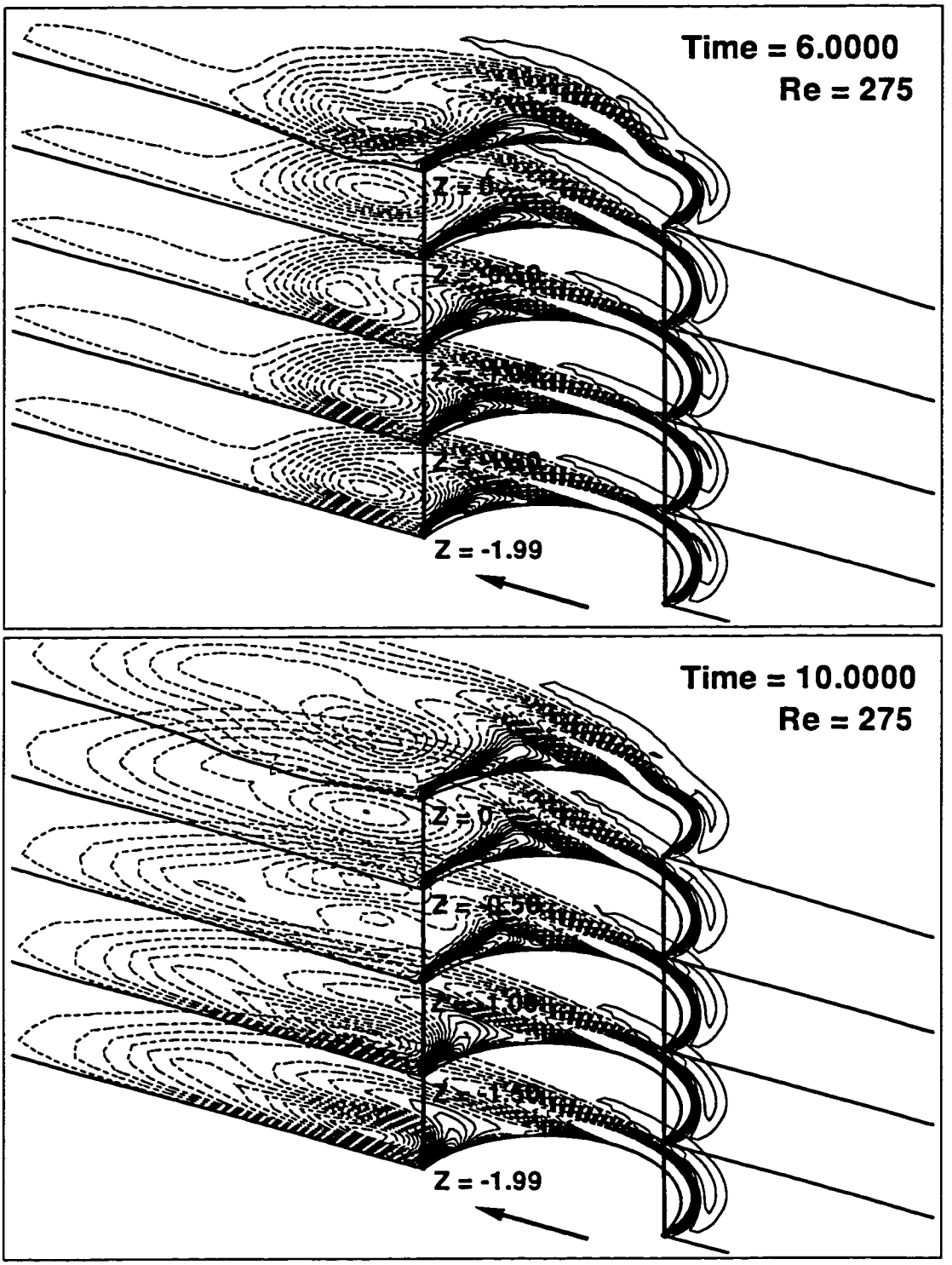

Figure 5.33: Vorticity contours for ω_z on five horizontal planes for $Re = 275$ and $Fr = 0.4$ at $t = 6.00$ (top) and at $t = 10.00$ (bottom). Contours are shown between -5.0 and 5.0 with increment of 0.4. Dashlines present negative values.

Reproduced with permission of the copyright owner. Further reproduction prohibited without permission. www.manaraa.com

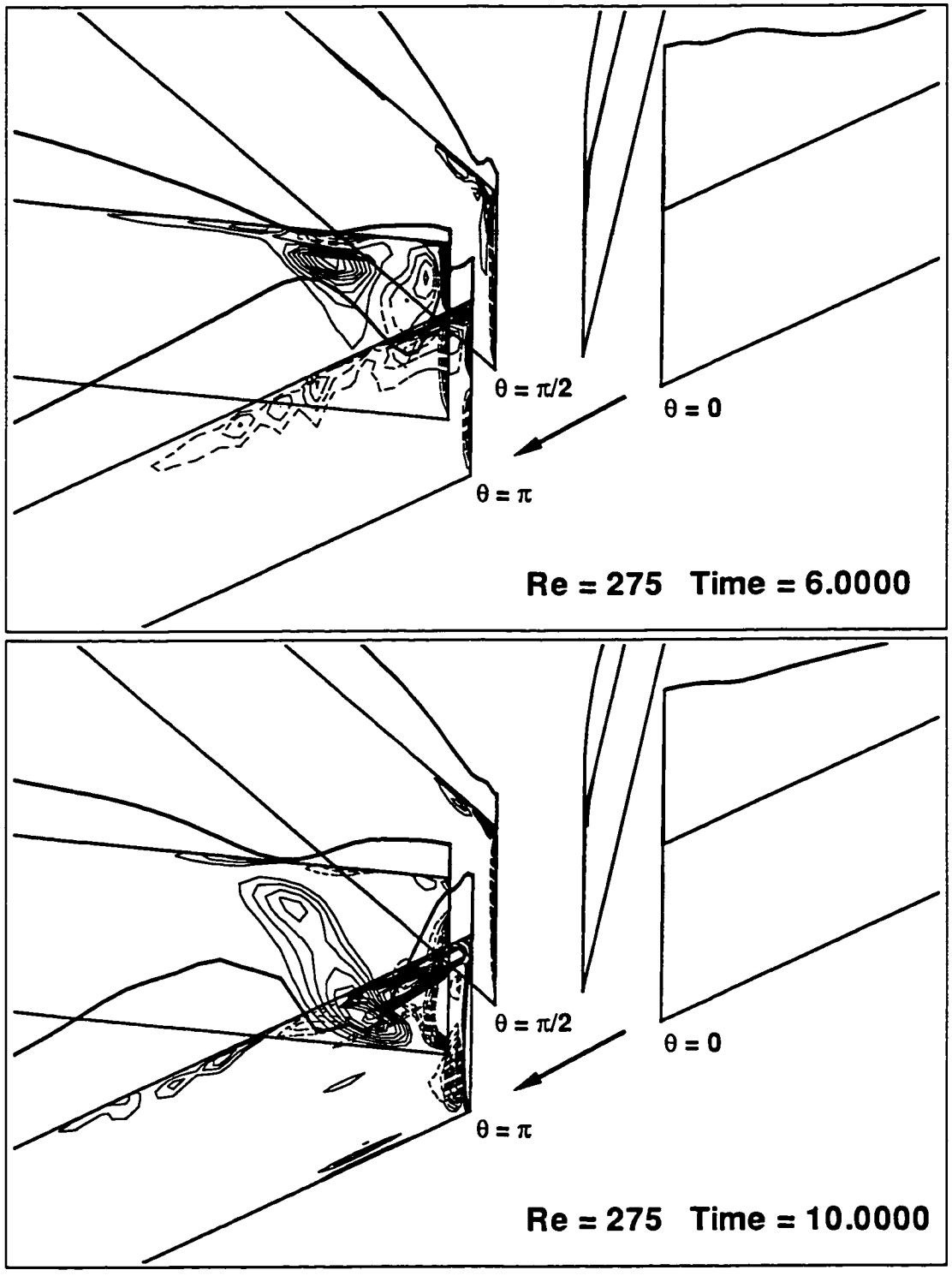

Figure 5.34: Vorticity contours for ω_θ on five radial planes for $Re = 275$ and $Fr = 0.4$ at $t = 6.00$ (top) and $t = 10.00$ (bottom). Contours are shown between -1.00 and 0.75 with increment of 0.07. Dashlines present negative values.

Reproduced with permission of the copyright owner. Further reproduction prohibited without permission. www.manaraa.com

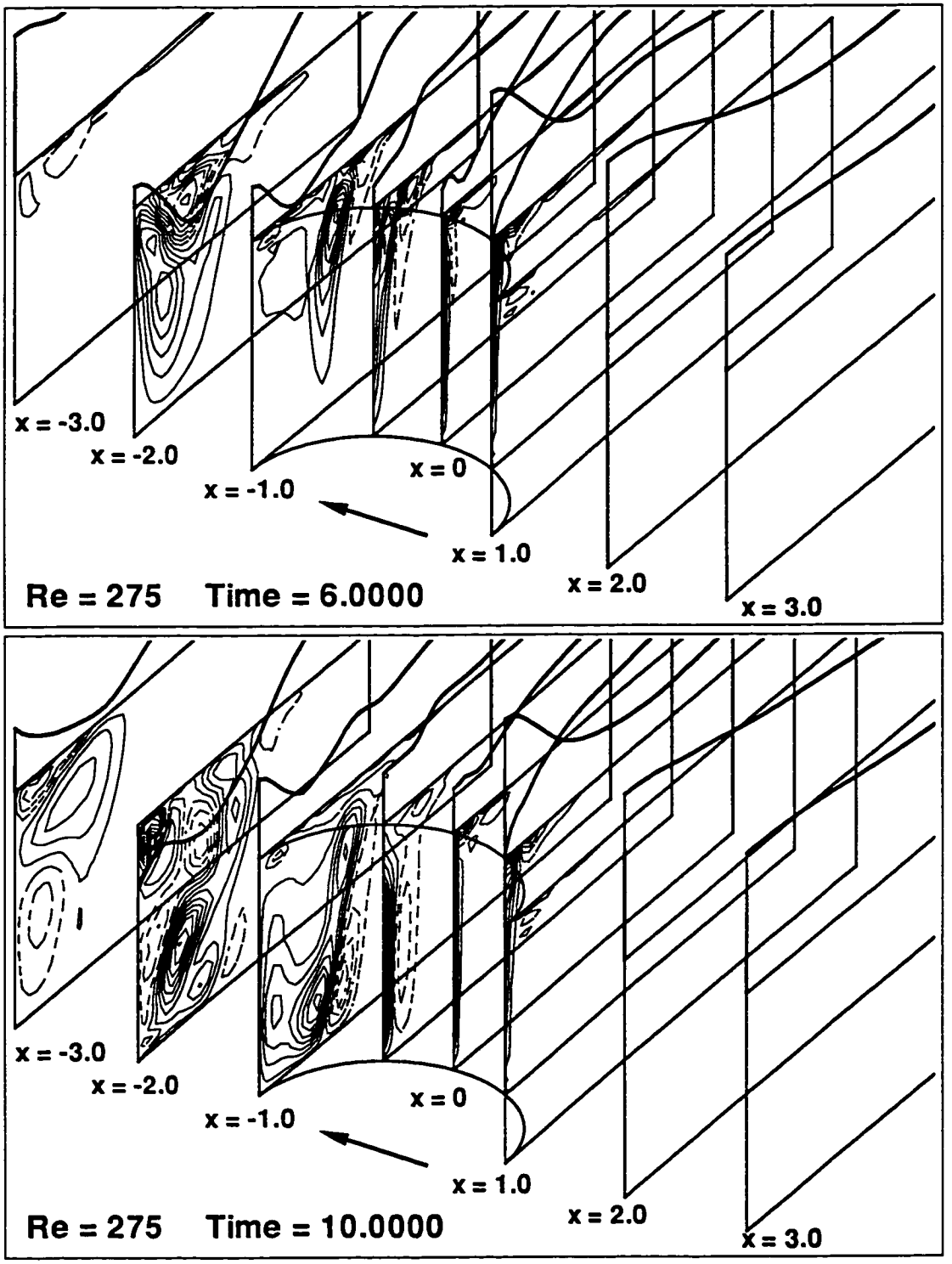

Figure 5.35: Vorticity contours for ω_x on nine transverse planes for $Re = 275$ and $Fr = 0.4$ at $t = 6.00$ (top) and at $t = 10.00$ (bottom). Contours are shown between -2.5 and 2.5 with increment of 0.2. Dashlines present negative values.

Reproduced with permission of the copyright owner. Further reproduction prohibited without permission. www.manaraa.com

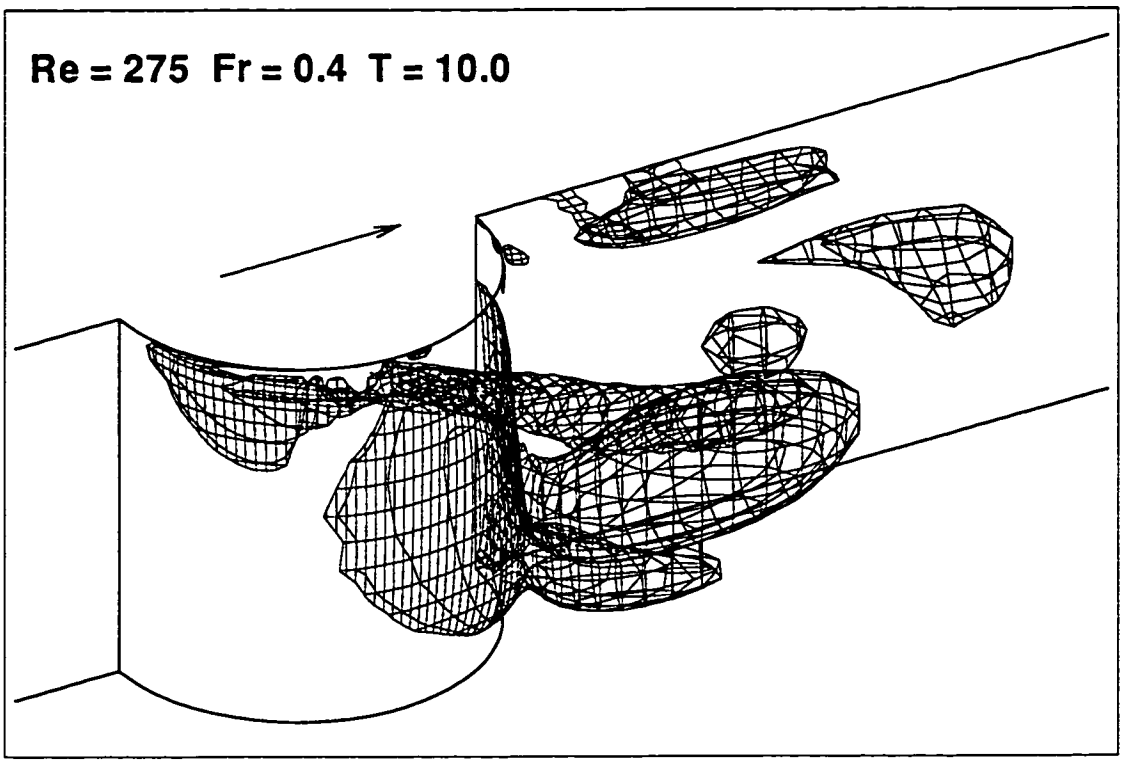

Figure 5.36: Iso-surface for $(\omega_r{}^2 + \omega_\theta{}^2)^{1/2} = 1.0$ for $Re = 275$ and $Fr = 0.4$ at $t = 10.00$.

Reproduced with permission of the copyright owner. Further reproduction prohibited without permission. www.manaraa.com

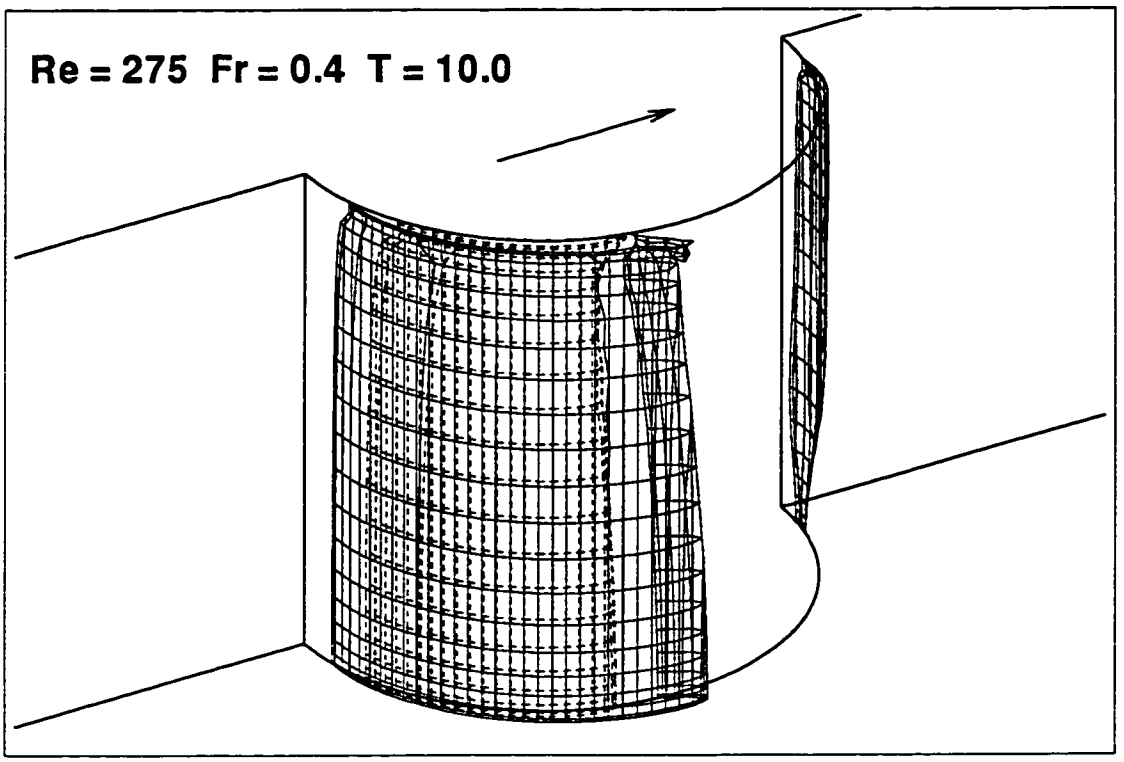

Figure 5.37: Iso-surface for $(\omega_r{}^2 + \omega_\theta{}^2 + \omega_z{}^2)^{1/2}$ for $Re = 275$ and $Fr = 0.4$ at $t = 10.00$. Dashline presents value of 15.0, solidline for 8.0.

Reproduced with permission of the copyright owner. Further reproduction prohibited without permission. www.manaraa.com

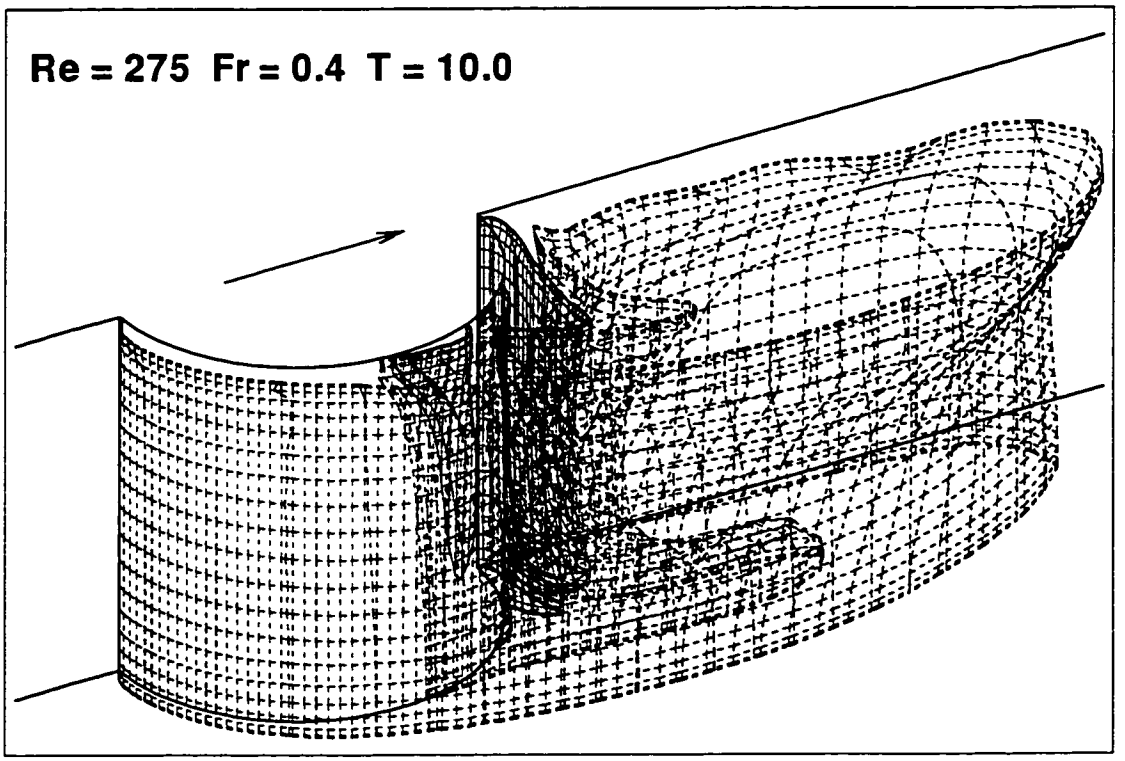

Figure 5.38: Iso-surface for ω_z for $Re = 275$ and $Fr = 0.4$ at $t = 10.00$. Dashline presents negative value of -1.0, solidline for $+1.0$.

Reproduced with permission of the copyright owner. Further reproduction prohibited without permission. www.manaraa.com

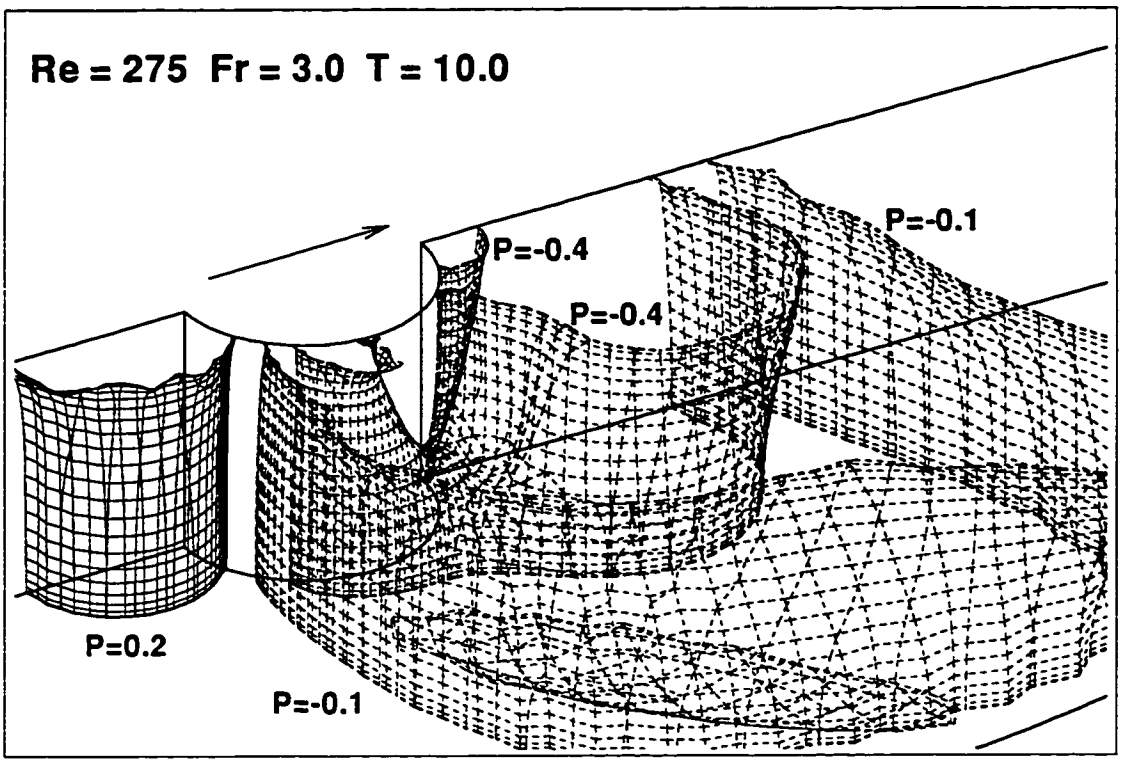

Figure 5.39: Iso-surface for dynamic pressure P for $Re = 275$ and $Fr = 0.4$ at $t = 10.00$. Dashlines present negative values.

Reproduced with permission of the copyright owner. Further reproduction prohibited without permission. www.manaraa.com

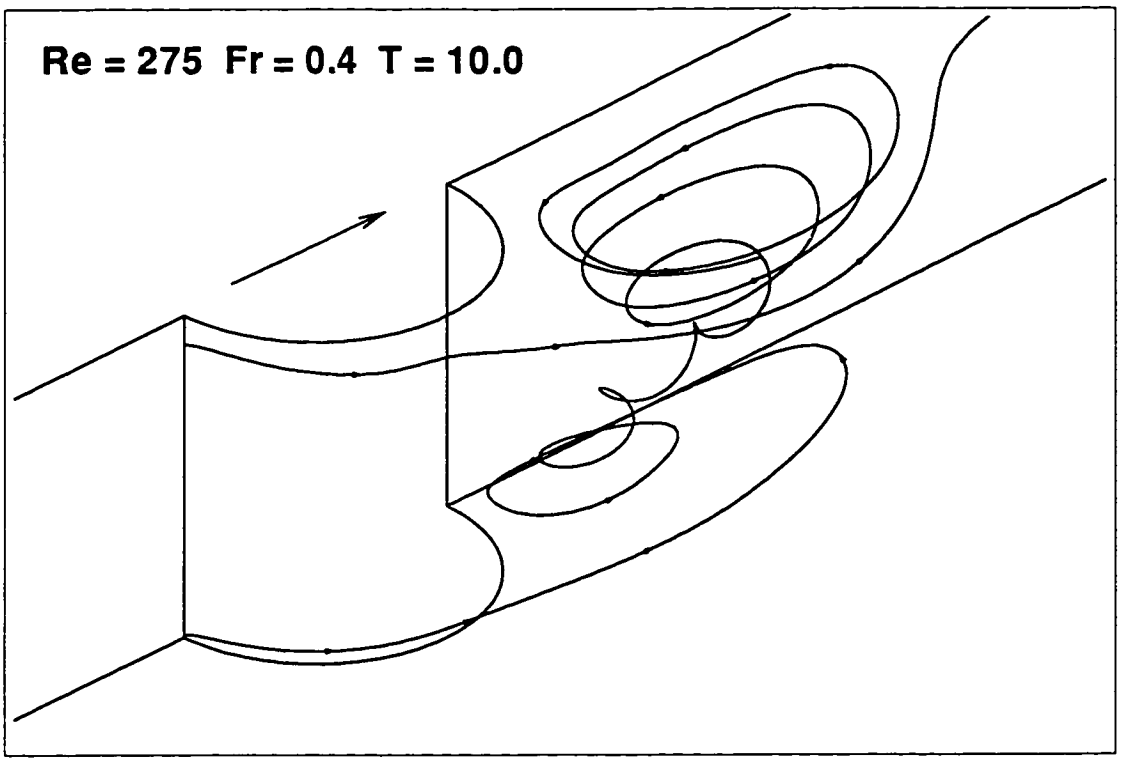

Figure 5.40: Particle trajectories for $Re = 275$ and $Fr = 0.4$ at $t = 10.00$.

Reproduced with permission of the copyright owner. Further reproduction prohibited without permission. www.manaraa.com

Chapter 6

Conclusions

An accurate and efficient pseudo-spectral method is developed in this thesis, for analyzing complex viscous flows around a vertical cylindrical structure with a free surface. The inviscid flow problem with free surface is first considered, followed by the consideration of viscous effects.

A Poisson-equation solver is first developed based on a diagonalization technique and a spectral collocation method. This spectral Poisson solver is then applied to several inviscid-flow problems, which include a three-dimensional Cauchy-Poisson wave problem with linearized free-surface conditions and a second-order wave diffraction problem. Validation with regards to accuracy, efficiency and convergence of the Poisson-equation solver is carried out. As shown in Chapter 3, the Poisson-equation solver yields solutions that converge *exponentially* to the exact ones as the number of grids increases. The total computational counts of this method is of order $O(N^{1.67})$ (N being the total number of grid points). These features allow one, on the one hand, to use fewer grid points to achieve higher accuracy, and, on the other hand, to use finer grid points to achieve higher flow resolution with relatively low computation efforts.

The formulation for the viscous-flow problem is based on the fractional step projection algorithm originated by Chorin (1968) for solving the Navier-Stokes equations. "Momentum equations" without the pressure terms are first solved for an auxiliary velocity field. An ADI algorithm is used to reduce these partial differential

Reproduced with permission of the copyright owner. Further reproduction prohibited without permission. www.manaraa.com

"momentum equations" into sets of ordinary differential equations, which are solved by a spectral collocation method. The Poisson-equation solver developed earlier is used to solve the resulted pressure Poisson equation. A velocity correction procedure concludes the formulation, which yields the "true" velocity field. In the case of free-surface flows, additional boundary conditions based on stress-continuity relations need to be applied. These free-surface boundary conditions are linearized by assuming small wave-slope.

This spectral method is applied to treat several viscous-flow problems. In order to show the method's ability of treating complex wave problems in a viscous fluid, a *viscous* Cauchy-Poisson wave problem is solved. The wave profiles for the case of a viscous fluid approach their inviscid counterparts as the Reynolds number increases. This shows that wave motions have been correctly modeled in the present study. Two problems with strongly nonlinear convective effects have also been studied. In the first case, a sheared current past a vertical cylinder under a free-slip surface is considered. The three-dimensional flow separation behind the cylinder and the formation of horseshoe vortices near the body-bottom juncture are simulated and examined. In the second case, a uniform current past cylinder under a free surface is considered. A Kelvin-like wave system is observed in the solution, and the three-dimensional vortical flow structures near the free surface are analyzed and visualized using visualization techniques. Extensive validations are also performed for viscous-flow solutions. Among them, the two-dimensional uniform flow around an impulsively started circular cylinder is studied, and compared with comprehensive existing experimental data. Excellent agreement is obtained for a wide range of Reynolds number from 550 to 9500, establishing method's ability to handle strongly convective flows. From these numerical studies, the spectral method is proven to be a highly accurate and highly efficient one.

In this work, only flows around a circular cylinder and under a linearized free surface are studied. However, an extension of this work to consider general body geometries and nonlinear free surface can be achieved in a number of ways. With special coordinate systems, treatment of other special body geometries (other than circular cylinder) is possible. As an example, a formulation of flow around

Reproduced with permission of the copyright owner. Further reproduction prohibited without permission. www.manaraa.com

a elliptical cylinder using elliptical coordinates is given in Appendix E. Numerical mapping techniques are also ideal candidates for this extension. For example, a stretching in the vertical direction, which maps a wavy free surface into a flat one, allows the solutions of nonlinear free-surface flows around cylindrical bodies. It is also worthwhile to pursue a spectral element method to tackle flow problems involving complex geometries. It has been proven in many fluid-mechanics applications that spectral element methods enjoy the geometric flexibility of finite element methods, and the accuracy and convergence properties of spectral methods, thus making them ideal for solving nonlinear free-surface flow problems.

Other extensions of the present method can also be made. The implementation of the RANS is straightforward in the present solution framework provided an appropriate turbulent model is incorporated. The high accuracy of this solution method also makes it ideal for direct numerical simulation (DNS) of turbulence. The accuracy of time-dependent solution can be further improved by using a higher-order difference scheme in time.

Reproduced with permission of the copyright owner. Further reproduction prohibited without permission. www.manaraa.com

Bibliography

[1] Alessandrini, B. and Delhommeau, G. (1994). "Numerical calculation of three-dimensional viscous free surface flow around a series 60 $C_b = 60$ ship model", *CFD Workshop Tokyo 1994*, Tokyo, Japan, pp. 95–104.

[2] Baba, E. (1969). "A new component of viscous resistance of ships", *Journal of the Society of Naval Architects of Japan*, **125**, pp. 23–34.

[3] Baba, E. (1981). "Some free surface phenomena around ships to be challenged by numerical analysis", *Proceedings of the 3rd International Conference on Numerical Ship Hydrodynamics,* Paris, France, pp. 9–23.

[4] Batchelor, G. K. (1970). *An Introduction to Fluid Mechanics*, Cambridge University Press, Cambridge, England.

[5] Bouard, R. and Coutanceau, M. (1980). "The early stages of development of the wake behind an impulsively started cylinder for $40 < Re < 10^4$", *Journal of Fluid Mechanics*, **101**, pp. 583–607.

[6] Campana, E., Esposito, P. and Penna, R. (1994). "Numerical simulation of the drift motion of a ship", *Proceedings of the 20th Symposium on Naval Hydrodynamics*, Santa Barbara, CA.

[7] Canuto, C. and Quarteroni, A. (1981). "Spectral and pseudospectral methods for parabolic problems with non-periodic boundary conditions", *Calcolo*, **23**, pp. 197–217.

Reproduced with permission of the copyright owner. Further reproduction prohibited without permission. www.manaraa.com

[8] Canuto, C., Hussaini, M. Y., Quarteroni, A. and Zang, T. A. (1987). *Spectral Methods in Fluid Dynamics*, Springer-Verlag, Berlin.

[9] Chen, H. C., Lin, W. M. and Weems, K. M. (1994). "Second-Moment RANS Calculations of Viscous Flow Around Ship Hulls", *CFD Workshop Tokyo 1994*, Tokyo, Japan, pp. 275–284.

[10] Chorin, A. J. (1968). "Numerical solution of incompressible flow problems," *Studies on Numerical Analysis*, **2**, pp. 64–71.

[11] Chorin, A. J. (1973). "Numerical study of slightly viscous flow", *J. Fluid Mech.*, **57**, pp. 785–796.

[12] Deng, G. B. and Piquet, J. (1992). "Navier-Stokes computations of horseshoe vortex flows", *International Journal for Numerical Methods in Fluids*, **15**, pp. 99–124.

[13] Farmer, J., Mattinelli, L. and Jameson, A. (1994). "Multigrid solutions of the Euler and Navier-Stokes equations for a series 60 $C_b = 0.6$ ship hull for Foude number 0.160, 0.220 and 0.316 (Program 1: Navier-Stokes formulation)", *Proceedings of CFD Workshop Tokyo 1994*, **1**, pp. 56–65.

[14] Goda, K. (1979). "A Multistep technique with implicit difference schemes for calculating two- or three-dimensional cavity flows", *Journal of Computational Physics*, **30**, pp. 76–95.

[15] Gottlieb, D. and Orszag, S. A. (1977). "Numerical analysis of spectral methods: theory, and application," *SIAM*, Philadelphia, PA..

[16] Griffin, O. M.; Keramidas, G. A.; Swean, T. F.; Wang, H. T.; Skop, R. A. and Leipold, Y. (1988). "Ocean and ship wave modification by a surface wake flow pattern", *Proceedings of the 17th Symposium on Naval Hydrodynamics* The Hague, The Netherlands.

Reproduced with permission of the copyright owner. Further reproduction prohibited without permission. www.manaraa.com

[17] Harlow, F. H. and Welch, J. E. (1965). "Numerical calculation of time-dependent viscous incompressible flow of fluid with free surface", *Physics of Fluids*, **8**, pp. 2182–2189.

[18] Havelock, T. H. (1963). *Collected Papers*, ONR/ACR-103. Washington: U.S. Government Printing Office.

[19] Hawthorne, W. R. (1954). "The secondary flow about struts and airfoils", *Journal of the Aeronautical Sciences,* **21**, pp. 588–608.

[20] Huh, C. and Scriven, L. E. (1971) "Hydrodynamic model of steady movement of a solid/liquid/fluid contact lines", *Journal of Colloid and Interface Science*, **35**, pp. 85–101.

[21] Hussaini, M. and Zang, T. (1987). "Spectral methods in fluid dynamics," *Annual Review of Fluid Mechanics*, **19**, pp. 339–367.

[22] Hussaini, M. Y. and Kopriva, D. A. and Patera, A. T. (1989). "Spectral collocation methods", *Applied Numerical Mathematics*, **5**, pp. 177–208.

[23] Karniadakis, G. E., Bullister, E. T. and Patera, A. T. (1986). "A spectral element method for the two- and three-dimensional time-dependent incompressible Navier-Stokes equations", *Proceedings of the Europe-U.S. Symposium on Finite Element Methods for Nonlinear Problems*, Springer, Berlin.

[24] Korczak, K. Z. and Patera, A. T. (1986). "An isoparametric spectral element method for solution of the Navier-Stokes equations in complex geometry," *Journal of Computational Physics*, **62**, pp. 361–382.

[25] Lamb, H. (1932). *Hydrodynamics,* 6th ed., Dover Publication Inc., New York.

[26] Lighthill, M. J. (1979). "Wave and hydrodynamic loading", *Proceedings of the 2nd International Conference on the Behavior of Offshore Structures*, BOSS'79, London.

Reproduced with permission of the copyright owner. Further reproduction prohibited without permission. www.manaraa.com

[27] Longuet-Higgins, M. S. and Cokelet, E. D. (1976). "The deformation of steep surface waves on water: i. a numerical method of computation", *Proceedings of the Royal Society of London*, **A 350**, pp. 1–26.

[28] McCamy, R. C. and Fuch, R. A. (1954). "Wave forces on a pile: a diffraction theory," *Technical Memoir*, **69**, U.S. Army Board, U. S. Army Corp. of Eng.

[29] Mei, C. C. (1989). *The Applied Dynamics of Ocean Surface Waves*, 2nd printing with corrections, Series on Ocean Engineering, World Scientific.

[30] Miyata, H. (1981). "Numerical explanation of nonlinear nondispersive waves around bow", *Proceedings of the 3rd International Conference on Numerical Ship Hydrodynamics*, Paris, France.

[31] Molin, B. (1979). "Second-order diffraction loads upon three dimensional bodies", *Applied Ocean Research*, **1**, pp. 197–202.

[32] Molin, B. and Marion, A. (1986). "Second-order loads and motions for floating bodies in regular waves", *Proceedings of the 5th International Symposium on Offshore Mechanics and Arctic Engineering*, Tokyo.

[33] Nakos, D. E. and Sclavounos, P. D. (1990). "Ship motions by a three-dimensional ranking panel method," *Proceedings of the 18th Symposium on Naval Hydrodynamics*, Ann Arbor, MI., pp. 21–40.

[34] Nayfeh, A. H. (1973). *Perturbation Methods*, Wiley, New York.

[35] Orszag, S. A. (1969). "Numerical methods for the simulation of turbulence", *Physics of Fluids*, **12**, pp. 250–257.

[36] Orszag, S. A. (1980). "Spectral methods for problems in complex geometries", *Journal of Computational Physics*, **37**, pp. 70–92.

[37] Pasciak, J. E. (1980). "Spectral and pseudospectral methods for advection equations", *Mathematics and Computers*, **35**, pp. 1081–1092.

Reproduced with permission of the copyright owner. Further reproduction prohibited without permission. www.manaraa.com

[38] Patera, A. T. (1986). "A spectral element method for fluid dynamics: Laminar flow in a channel expansion", *Journal of Computational Physics*, **54**, pp. 468.

[39] Press, W. H., Flannery, B. P., Teukolsky, S. A and Vetterling, W. T. (1989). *"Numerical Recipes"*, 1st edition, Cambridge University Press, Cambridge, England.

[40] Raven, H. C. (1992). "A Practical Nonlinear Method for Calculating Ship Wavemaking and Wave Resistance", *Proceedings of the 19th Symposium on Naval Hydrodynamics,* Seoul, South Korea.

[41] Sarpkaya, T. (1968) "An analytical study of Separated flow about circular cylinders", *ASME Journal of Basic Engineering*, **90**, pp. 511–520.

[42] Shanks, S. P. (1977). "Numerical simulation of viscous flow about submerged arbitrary hydrofoils using non-orthogonal curvilinear coordinates", Ph.D. thesis, Mississippi State University, Miss.

[43] Sherman, F. S. (1990). *Viscous Flow*, McGraw-Hill, New York.

[44] Sod, G. A. (1985). *Numerical Methods in Fluid Dynamics,* Cambridge University Press, Cambridge, England.

[45] Stansby, P. K. and Dixon, A. G. (1983). "Simulation of flows around cylinders by a Lagrangian vortex scheme", *Applied Ocean Research*, **5**, pp. 167–178.

[46] Schlichting, H. (1968). *Boundary-Layer Theory*, 6th ed., McGraw-Hill, New York.

[47] Tahara, Y., Stern, F. (1994). "A large-domain approach for calculating ship boundary layers and wakes for nonzero Froude number," *Proceedings of CFD Workshop Tokyo 1994*, **1**, pp. 45–55.

[48] Tan, C. S. (1985). "Accurate solution of three-dimensional Poisson equation in cylindrical coordinate by expansion in chebyshev polynomials," *Journal Computational Physics*, **59**, pp. 81–95.

Reproduced with permission of the copyright owner. Further reproduction prohibited without permission. www.manaraa.com

[49] Tan, C. S. (1989). "A multi-domain spectral computation of three-dimensional laminar horseshoe vortex flow using incompressible Navier-Stokes equations," *Journal of Computational Physics*, **85**, pp. 130–158.

[50] Ta Phuoc Loc and Bouard R. (1983). "Numerical solution of the early stage of the unsteady viscous flow around a circular cylinder: a comparison with experimental visualization and measurements", *Journal of Fluid Mechanics*, **160**, pp. 93–117.

[51] Weems, K., Korpus, R., Lin, W. M., Fritts, M. and Chen, H. C. (1994). "Near-field flow predictions for ship design", *Proceedings of the 20th Symposium on Naval Hydrodynamics*, Santa Barbara, CA.

[52] Wehausen, J. V. and Laitone, E. V. (1960). "Surface Waves," *Handbuch der Physik*, **9**, Springer, Berlin.

[53] Yeung, R. W. (1981). "Added mass and damping of a vertical cylinder in finite-depth waters", *Applied Ocean Research*, **3**, pp. 119–133.

[54] Yeung, R. W. (1982). "Numerical methods in free surface flows," *Annual Review of Fluid Mechanics*, **14**, pp. 395–442.

[55] Yeung, R. W. (1985). "A comparative evaluation of numerical methods in free-surface hydrodynamics", *Proceedings of the IUTAM Symposium*, Lisbon.

[56] Yeung, R. W. and Ananthakrishnan, P. (1992). "Vortical flows with and without a surface-piercing body," *Proceedings of the 19th Symposium on Naval Hydrodynamics*, Seoul, South Korea.

[57] Yeung, R. W. and Vaidhyanathan, M. (1992). "Non-linear interaction of water waves with submerged obstacles", *International Journal for Numerical Methods in Fluids*, **14**, pp. 1111–1130.

[58] Zhu, M., Yoshida, O., Miyata, H. and Aoki, K. (1993). "Verification of the viscous flow-field simulation for practical hull forms by a finite-volume method", *6th. International Conference on Numerical Ship Hydrodynamics, Iowa city, Iowa*, pp. 9-12–30.

Reproduced with permission of the copyright owner. Further reproduction prohibited without permission. www.manaraa.com

Appendix A

Coefficients for spectral Poisson equation solver

In this appendix, we give mathematical expressions for γ_{nq} and $D_{mn}(R)$ in Eqn. (2.20).

When n is odd with all q such that $0 \leq q \leq n+1$ and even q such that $n+3 \leq q \leq N-2$

$$\gamma_{nq} = \frac{1}{D_{AB}C_n}(N-1)[(N-1)^2 - n^2][(A_- - B_-N^2)(A_+ + B_+q^2) - (A_+ + B_+N^2)(-1)^q(A_- - B_-q^2)], \tag{A.1}$$

while with odd q such that $n+2 \leq q \leq N-3$

$$\gamma_{nq} = \frac{1}{C_n}q(q^2-n^2) + \frac{1}{D_{AB}C_n}(N-1)[(N-1)^2 - n^2][(A_- - B_-N^2)(A_+ + B_+q^2) - (A_+ + B_+N^2)(-1)^q(A_- - B_-q^2)]. \tag{A.2}$$

$D_{mn}(R)$ is given by

$$D_{mn}(R) = \frac{1}{D_{AB}C_n}(N-1)[(N-1)^2 - n^2] \times [(A_+ + B_+N^2)h_{-m}(R) - (A_- - B_-N^2)h_{+m}(R). \tag{A.3}$$

When n is even with all q such that $0 \leq q \leq n+1$ and odd q such that $n+3 \leq q \leq N-2$

$$\gamma_{nq} = \frac{1}{D_{AB}C_n}N(N^2-n^2)\{[A_- - B_-(N-1)^2][A_+ + B_+q^2]$$

Reproduced with permission of the copyright owner. Further reproduction prohibited without permission. www.manaraa.com

$$+[A_+ + B_+(N-1)^2](-1)^q[A_- - B_-q^2]\}, \tag{A.4}$$

while with even q such that $n+2 \leq q \leq N-2$

$$\gamma_{nq} = \frac{1}{C_n}q(q^2-n^2) + \frac{1}{\{}D_{AB}C_nN(N^2-n^2)[A_- - B_-(N-1)^2][A_+ + B_+q^2]$$
$$+[A_+ + B_+(N-1)^2](-1)^q[A_- - B_-q^2]\}. \tag{A.5}$$

$D_{mn}(R)$ is given by

$$D_{mn}(R) = -\frac{1}{D_{AB}C_n}N(N^2-n^2)$$
$$\times\{[A_- - B_-(N-1)^2]h_{+m}(R) + [A_+ + B_+(N-1)^2]h_{-m}(R)\}. \tag{A.6}$$

The D_{AB} in above equations is given by

$$D_{AB} = -\{[A_- - B_-(N-1)^2][A_+ + B_+N^2] + [A_- - B_-N^2][A_+ + B_+(N-1)^2]\}. \tag{A.7}$$

Reproduced with permission of the copyright owner. Further reproduction prohibited without permission. www.manaraa.com

Appendix B

Solution of ordinary differential equations by spectral collocation methods

In this appendix, we give details on how a second-order ordinary differential equation is solved by a spectral collocation method.

B.1 Solution by Chebyshev collocation method

Consider second-order ODE

$$y''(x) + a(x)y'(x) + b(x)y(x) = c(x) \qquad -1 \leq x \leq +1, \tag{B.1}$$

with boundary conditions

$$\begin{aligned} A_-y(-1) + B_-y'(-1) &= C_-, \\ A_+y(+1) + B_+y'(+1) &= C_+, \end{aligned} \tag{B.2}$$

where $a(x)$, $b(x)$ and $c(x)$ are smooth functions, and A_-, B_-, A_+ and B_+ are constants.

We first expand function $y(x)$ by a truncated Chebyshev series

$$y(x) = \sum_{j=0}^{N} a_j T_j(x), \tag{B.3}$$

Reproduced with permission of the copyright owner. Further reproduction prohibited without permission. www.manaraa.com

where $T_j(x)$ is the Chebyshev polynomial of order j. Substitution of Eqn. (B.3) into Eqn. (B.1) gives

$$\sum_{j=0}^{N} \left[T_j''(x) + a(x)T_j'(x) + b(x)T_j(x)\right] a_j = c(x). \tag{B.4}$$

Using relation

$$T_j''(x) = \frac{xT_j'(x) - j^2 T_j(x)}{1-x^2}, \tag{B.5}$$

we rewrite Eqn. (B.4) as

$$\sum_{j=0}^{N} \left\{ \left[\frac{x}{1-x^2} + a(x)\right] T_j'(x) + \left[b(x) - \frac{j^2}{1-x^2}\right] T_j(x) \right\} a_j = c(x). \tag{B.6}$$

We choose satisfy Eqn. (B.6) at collocation points

$$x_i = -\cos\frac{\pi}{N} i, \quad \text{for} \quad i = 1, N-1. \tag{B.7}$$

It is easy to show that

$$T_j(x_i) = \cos\left(\frac{\pi}{N} ij\right)(-1)^j, T_j'(x_i) = \frac{j(-1)^{j+1}}{\sin\left(\frac{\pi}{N} i\right)} \sin\left(\frac{\pi}{N} ij\right), \tag{B.8}$$

and Eqn. (B.6) can be written as

$$\sum_{j=0}^{N} A_{ij} a_j = c(x_i), \quad \text{for} \quad i = 1, N-1 \tag{B.9}$$

where

$$A_{ij} = \left[\frac{-\cos\frac{\pi}{N} i}{\sin^2\left(\frac{\pi}{N} i\right)} + a(x_i)\right] \frac{j(-1)^{j+1}}{\sin\left(\frac{\pi}{N} i\right)} \sin\left(\frac{\pi}{N} ij\right) + \left[b(x_i) - \frac{j^2}{\sin\left(\frac{\pi}{N} i\right)}\right] (-1)^j \cos\left(\frac{\pi}{N} ij\right). \tag{B.10}$$

To satisfy boundary condition (B.2), we substitute (B.3) into (B.2) to yield

$$\begin{aligned} &\sum_{j=0}^{N} A_- T_j(-1) + B_- T_j'(-1) = C_- \\ &\sum_{j=0}^{N} A_+ T_j(+1) + B_+ T_j'(+1) = C_+. \end{aligned} \tag{B.11}$$

Reproduced with permission of the copyright owner. Further reproduction prohibited without permission. www.manaraa.com

Using relations $T_j(-1) = (-1)^j$, $T_j'(-1) = (-1)^{j+1}j^2$, $T_j(+1) = j$ and $T_j'(+1) = j^2$, we write Eqn. (B.11) as

$$\sum_{j=0}^{N} A_{0j}a_j = C_-,$$
$$\sum_{j=0}^{N} A_{Nj}a_j = C_+, \tag{B.12}$$

where

$$A_{0j} = A_-(-1)^j + B_-(-1)^{j+1}j^2,$$
$$A_{Nj} = A_+ + B_+j^2. \tag{B.13}$$

The linear system in Eqns. (B.9) and (B.12) with full matrix A_{ij} is solved most accurately with a direct method, or by an iterative method (Orszag, 1980).

Note the collocation points in Eqn. (B.7) are of Chebyshev spacing. The spectral convergence of the above procedure in such a spacing is guaranteed, provided $a(x)$, $b(x)$ and $c(x)$ are smooth functions (Canuto and Quarteroni, 1981).

B.2 Solution by Fourier collocation method

Consider periodic function $y(x)$ satisfying a second-order ODE

$$y''(x) + a(x)y'(x) + b(x)y(x) = c(x) \qquad -\pi \le x \le +pi, \tag{B.14}$$

where $a(x)$, $b(x)$ and $c(x)$ are smooth functions.

We first expand function $y(x)$ by a truncated Fourier series

$$y(x) = \sum_{j=-\frac{N}{2}}^{\frac{N}{2}-1} a_j e^{ijx} \tag{B.15}$$

where $i = \sqrt{-1}$. Substitution of Eqn. (B.15) into Eqn. (B.14) gives

$$\sum_{j=-\frac{N}{2}}^{\frac{N}{2}-1} \left[-j^2 + ija(x) + b(x)\right] e^{ijx} = c(x). \tag{B.16}$$

Reproduced with permission of the copyright owner. Further reproduction prohibited without permission. www.manaraa.com

We choose satisfy Eqn. (B.16) at collocation points

$$x_i = \frac{2\pi}{N} i, \quad \text{for} \quad i = -\frac{N}{2}, \frac{N}{2} - 1. \tag{B.17}$$

Eqn. (B.16) can be written as

$$\sum_{j=0}^{N} A_{ij} a_j = c(x_i), \quad \text{for} \quad i = 1, N-1 \tag{B.18}$$

where

$$A_{ij} = \left[-j^2 + \mathrm{i} j a(x_i) + b(x_i) \right] e^{\mathrm{i} j x_i}. \tag{B.19}$$

The linear system in Eqns. (B.18) with full matrix A_{ij} is solved most accurately by a direct method.

The spectral convergence of the above procedure is proved by Pasciak (1980), provided $a(x)$, $b(x)$ and $c(x)$ are smooth functions.

Reproduced with permission of the copyright owner. Further reproduction prohibited without permission. www.manaraa.com

Appendix C

Calculation of derivatives in spectral collocation methods

In this appendix, we give details on how to calculate first-order derivative of a smooth function under the framework of spectral collocation methods. The same treatment also applies to higher-order derivatives.

C.1 Calculation of derivative in Chebyshev collocation method

Let $f(x)$ be a smooth function in the domain $x \in [-1, 1]$. Then $f(x)$ is interpolated by the Nth order polynomial $g_j(x)$ such such that $g_j(x_i) = \delta_{ji}$ at collocation points x_i, i.e.

$$f(x) = \sum_{j=0}^{N} f(x_j) g_j(x). \tag{C.1}$$

If x_i is chosen to be Chebyshev collocation points $x_i = -\cos\frac{\pi}{N} i$, for $i = 0, ..., N$, it is shown by Canuto and Quarteroni (1981) that

$$g_j(x) = \frac{(-1)^{j+1}(1-x^2)T'_N(x)}{c_j N^2 (x - x_j)}, \quad , j = 0, ..., N. \tag{C.2}$$

The derivative of $f(x)$ at collocation points x_i can be computed by taking analytical derivative of $g_j(x)$ and evaluating it at x_i, i.e., $D_{ij} = g'_j(x_i)$. Canuto and

Reproduced with permission of the copyright owner. Further reproduction prohibited without permission. www.manaraa.com

Quarteroni show (1981) that, for $j = 0, ...N$, $i = 0, ..., \frac{N}{2}$

$$\begin{aligned} D_{ij} &= \frac{1}{2}\frac{c_i}{c_j}\frac{(-1)^{i+j}}{\sin\frac{\pi}{2N}(i+j)\sin\frac{\pi}{2N}(i-j)} \quad j \neq k, \\ D_{ii} &= \frac{1}{2}\frac{\cos(\frac{\pi}{N}i)}{\sin^2(\frac{\pi}{N}i)} \quad i \neq 0, \\ D_{00} &= -\frac{2N^2+1}{6}. \end{aligned} \tag{C.3}$$

and

$$D_{ij} = -D_{N-i,N-j}, \text{ for } i = \frac{N}{2}+1, ..., N. \tag{C.4}$$

The derivative of $f(x_i)$ becomes

$$f'(x_i) = \sum_{j=0}^{N} D_{ij} f(x_i), \text{ for } i = 0, ..., N. \tag{C.5}$$

C.2 Calculation of derivative in Fourier collocation method

Let $f(x)$ be a smooth periodic function with period 2π in the domain $x \in [-\pi, \pi]$. We expand $f(x)$ into a truncated Fourier series

$$f(x) = \sum_{i=-N/2}^{N/2-1} \hat{f}_i e^{\mathrm{i}ix}, \tag{C.6}$$

where

$$\hat{f}_i = \frac{1}{N}\sum_{j=0}^{N-1} f(x_j) e^{-\mathrm{i}ix_j}, \tag{C.7}$$

with $x_j = -\pi + \frac{2\pi}{N}j$. Substitution of Eqn. (C.7) into Eqn. (C.6) yields

$$f(x) = \frac{1}{N}\sum_{i=-N/2}^{N/2-1}\left[\sum_{j=0}^{N-1} f(x_j) e^{-\mathrm{i}ix_j}\right] e^{\mathrm{i}ix}. \tag{C.8}$$

Taking derivative of Eqn. (C.8) and changing the sequence of summation, we have

$$f'(x) = \sum_{j=0}^{N-1} f(x_j)\left[\frac{\mathrm{i}}{N}\sum_{i=-N/2}^{N/2-1} i e^{\mathrm{i}i(x-x_j)}\right]. \tag{C.9}$$

At collocation points $x = x_i$, we rewrite Eqn. (C.9) as

$$f'(x_i) = \sum_{j=0}^{N-1} f(x_j) D_{ij}, \tag{C.10}$$

Reproduced with permission of the copyright owner. Further reproduction prohibited without permission. www.manaraa.com

where D_{ij} can be reduced to

$$D_{ij} = \frac{\mathrm{i}}{N} \sum_{i=-N/2}^{N/2-1} i e^{\mathrm{i}i\frac{2\pi(i-j)}{N}} = \frac{\mathrm{i}}{N} \left[-(-1)^{i-j} + 2\mathrm{i} \sum_{i=1}^{N/2-1} i \sin \frac{2\pi(i-j)}{N} \right]. \quad \text{(C.11)}$$

The summation in Eqn. (C.11) can be further reduce by using identity

$$\sum_{k=1}^{n-1} k \sin kx = \frac{\sin nx}{2\sin^2 \frac{x}{2}} - \frac{n \cos \frac{2n-1}{2} x}{2 \sin \frac{x}{2}}, \quad \text{(C.12)}$$

and finally

$$D_{ij} = (-1)^{i-j} \left[-\frac{\mathrm{i}}{N} + \frac{1}{2} \cot \frac{\pi(i-j)}{N} \right] \quad \text{(C.13)}$$

Reproduced with permission of the copyright owner. Further reproduction prohibited without permission. www.manaraa.com

Appendix D

Perturbation expansion of free-surface conditions

In this appendix, we first derive the perturbation expansion of the nonlinear kinematic and dynamic free-surface conditions up to the third order. The difficulties of solving the time-dependent *third-order* diffraction problem using these free-surface conditions are discussed next.

The nonlinear kinematic and dynamic free-surface conditions in cylindrical coordinates are

$$\begin{aligned} \eta_t + \eta_r\phi_r + \frac{1}{r^2}\eta_\theta\phi_\theta - \phi_z = 0 \qquad & z = \eta, \\ \eta + \phi_t + \frac{1}{2}(\phi_r^2 + \frac{1}{r^2}\phi_\theta^2 + \phi_z^2) = 0 \qquad & z = \eta. \end{aligned} \tag{D.1}$$

Note that these two conditions are satisfied at unknown position $z = \eta$. To overcome this difficult, we assume that this displacement of the free-surface η is small, and we express quantities at the exact free surface by Taylor series based on the mean free surface. For example, we write

$$\begin{aligned} \phi(r,\theta,\eta,t) &= \phi(r,\theta,0,t) + \eta\phi_z(r,\theta,0,t) + \frac{1}{2}\eta^2\phi_{zz}(r,\theta,0,t) + O(\eta^3), \\ \phi_r(r,\theta,\eta,t) &= \phi_r(r,\theta,0,t) + \eta\phi_{rz}(r,\theta,0,t) + \frac{1}{2}\eta^2\phi_{rzz}(r,\theta,0,t) + O(\eta^3), \\ \phi_\theta(r,\theta,\eta,t) &= \phi_\theta(r,\theta,0,t) + \eta\phi_{\theta z}(r,\theta,0,t) + \frac{1}{2}\eta^2\phi_{\theta zz}(r,\theta,0,t) + O(\eta^3), \\ &\cdots\cdots \end{aligned} \tag{D.2}$$

Reproduced with permission of the copyright owner. Further reproduction prohibited without permission. www.manaraa.com

Substitution of Eqn. (D.2) in Eqn. (D.1) gives

$$\eta_t + \eta_r(\phi_r + \eta\phi_{rz} + \frac{1}{2}\eta^2\phi_{rzz}) + \frac{1}{r^2}\eta_\theta(\phi_\theta + \eta\phi_{\theta z} + \frac{1}{2}\eta^2\phi_{\theta zz}) - (\phi_z + \eta\phi_{zz} + \frac{1}{2}\eta^2\phi_{zzz}) + O(\eta^3) = 0,$$

$$\eta + (\phi_t + \eta\phi_{tz} + \frac{1}{2}\eta^2\phi_{tzz}) + \frac{1}{2}(\phi_r + \eta\phi_{rz} + \frac{1}{2}\eta^2\phi_{rzz})^2 + \frac{1}{2r^2}(\phi_\theta + \eta\phi_{\theta z} + \frac{1}{2}\eta^2\phi_{\theta zz})^2 + \frac{1}{2}(\phi_z + \eta\phi_{zz} + \frac{1}{2}\eta^2\phi_{zzz})^2 + O(\eta^3) = 0. \quad \text{(D.3)}$$

We now introduce perturbation series with respect to wave steepness ϵ:

$$\phi = \epsilon\phi^{(1)} + \epsilon^2\phi^{(2)} + \epsilon^3\phi^{(3)} + O(\epsilon^4),$$
$$\eta = \epsilon\eta^{(1)} + \epsilon^2\eta^{(2)} + \epsilon^3\eta^{(3)} + O(\epsilon^4). \quad \text{(D.4)}$$

Following the multiple-scales analysis procedure (see Nayfeh, 1973), we also introduce formally slow time variables

$$t_1 = \epsilon t, \quad t_2 = \epsilon^2 t, \quad t_3 = \epsilon^3 t, ..., \quad \text{(D.5)}$$

so that $\frac{\partial}{\partial t}$ should be replaced by

$$\frac{\partial}{\partial t} \to \frac{\partial}{\partial t} + \epsilon\frac{\partial}{\partial t_1} + \epsilon^2\frac{\partial}{\partial t_2} + ... \quad \text{(D.6)}$$

Substituting Eqns. (D.4) to (D.6) into Eqn. (D.3) and collecting terms of same order of ϵ, we obtain:

$O(\epsilon)$:

$$\eta_t^{(1)} - \phi_z^{(1)} = 0,$$
$$\eta^{(1)} + \phi_t^{(1)} = 0; \quad \text{(D.7)}$$

$O(\epsilon^2)$:

$$\eta_t^{(2)} - \phi_z^{(2)} = \left\{-\eta_r^{(1)}\phi_r^{(1)} - \frac{1}{r^2}\eta_\theta^{(1)}\phi_\theta^{(1)} + \eta^{(1)}\phi_{zz}^{(1)}\right\} - \eta_{t_1}^{(1)},$$
$$\eta^{(2)} + \phi_t^{(2)} = \left\{-\eta^{(1)}\phi_{tz}^{(1)} - \frac{1}{2}\left[\phi_r^{(1)2} + \frac{1}{r^2}\phi_\theta^{(1)2} + \phi_z^{(1)2}\right]\right\} - \phi_{t_1}^{(1)}; \quad \text{(D.8)}$$

Reproduced with permission of the copyright owner. Further reproduction prohibited without permission. www.manaraa.com

$O(\epsilon^3)$:

$$\eta_t^{(3)} - \phi_z^{(3)} = \left\{ -\left[\eta_r^{(1)}\phi_r^{(2)} + \eta_r^{(2)}\phi_r^{(1)}\right] - \frac{1}{r^2}\left[\eta_\theta^{(1)}\phi_\theta^{(2)} + \eta_\theta^{(2)}\phi_\theta^{(1)}\right]\right\}$$
$$-\eta^{(1)}\left[\eta_r^{(1)}\phi_{rz}^{(1)} + \frac{1}{r^2}\eta_\theta^{(1)}\phi_{\theta z}^{(1)} - \phi_{zz}^{(2)}\right] + \left[\eta^{(2)}\phi_{zz}^{(1)} + \frac{1}{2}\eta^{(1)^2}\phi_{zzz}^{(1)}\right] - \left[\eta_{t_2}^{(1)} + \eta_{t_1}^{(2)}\right],$$
$$\eta^{(3)} + \phi_t^{(3)} = -\left[\eta^{(1)}\phi_{tz}^{(2)} + \eta^{(2)}\phi_{tz}^{(1)} + \frac{1}{2}\phi_{tzz}^{(1)}\right] - \left[\phi_r^{(1)}\phi_r^{(2)} + \frac{1}{r^2}\phi_\theta^{(1)}\phi_\theta^{(2)} + \phi_z^{(1)}\phi_z^{(2)}\right]$$
$$-\eta^{(1)}\left[\phi_r^{(1)}\phi_{rz}^{(1)} + \frac{1}{r^2}\phi_\theta^{(1)}\phi_{\theta z}^{(1)} + \phi_z^{(1)}\phi_{zz}^{(1)}\right] - \left[\phi_{t_2}^{(1)} + \phi_{t_1}^{(2)} + \eta^{(1)}\phi_{zt_1}^{(1)}\right]. \tag{D.9}$$

The solutions for velocity potentials $\phi^{(1)}$ and $\phi^{(2)}$ can be derived using the method of separation of variables, accounting for the free-surface conditions in Eqns. (D.7) and (D.8) (see Mei, 1989). The results are given as

$$\phi^{(1)} = Re\left[\frac{A(t_2)\omega}{k}\frac{\cosh k(z+d)}{\sinh kd}e^{i\theta}\right],$$
$$\phi^{(2)} = Re\left[\frac{3A^2(t_2)\omega}{8}\frac{\cosh 2k(z+d)}{\sinh^4 kd}e^{2i\theta}\right], \tag{D.10}$$

where $\theta = kx - \omega t$, with ω satisfying $\omega^2 = kg\tanh kd$.

A combined free-surface condition for $\phi^{(3)}$ can be derived by eliminating $\eta^{(3)}$ from Eqn. (D.9). Substitution of Eqn. (D.10) into this combined free-surface condition gives:

$$\phi_{tt}^{(3)} + \phi_z^{(3)} = \frac{\omega k^2}{16\sinh^4 kd}[(-iA^3e^{3i\theta} + iA^{*3}e^{-3i\theta})(6\cosh 2kd - 33)$$
$$+|A|^2(-iAe^{i\theta} + iA^*e^{-i\theta})(-\cosh 4kd - 8)] + [Ae^{i\theta} + A^*e^{-i\theta}]. \tag{D.11}$$

The terms proportional to $e^{i\theta}$ or $e^{-i\theta}$ are the so-called "secular terms", which have to be eliminated, in order to have solution $\phi^{(3)}$ bounded at large t (see Nayfeh, 1973). This leads to

$$\frac{dA}{dt_2} + i\omega_2|A|^2A = 0, \tag{D.12}$$

where $\omega_2 = \omega k^2\frac{\cosh 4kd+8}{16\sinh^4 kd}$. The solution to Eqn. (D.12) is

$$A(t_2) = ae^{-i\omega_2 a^2 t_2}, \tag{D.13}$$

where a is a constant.

Reproduced with permission of the copyright owner. Further reproduction prohibited without permission. www.manaraa.com

Substituting Eqn. (D.13) into Eqn. (D.10) gives

$$\phi^{(1)} = \frac{a\omega}{k}\frac{\cosh k(z+d)}{\sinh kd}\sin(kx-\tilde{\omega}t),$$
$$\phi^{(2)} = \frac{3A^2(t_2)\omega}{8}\frac{\cosh 2k(z+d)}{\sinh^4 kd}\sin 2(kx-\tilde{\omega}t), \tag{D.14}$$

where $\tilde{\omega}$ is the modified wave frequency given by

$$\tilde{\omega} = \omega\left[1 + a^2k^2\frac{\cosh 4kd + 8}{16\sinh^4 kd}\right]. \tag{D.15}$$

The solutions in Eqns. (D.14) with the modified frequency $\tilde{\omega}$ do not *exactly* satisfy the free-surface conditions in Eqns. (D.7) and (D.8). As a consequence, if Eqns. (D.14) are given as boundary and initial conditions for the first and second order problems (as in Section 3.4), the waves will modulate even before they interact with the cylinder.

Reproduced with permission of the copyright owner. Further reproduction prohibited without permission. www.manaraa.com

Appendix E

Solution of Poisson equation in elliptical coordinates using a spectral method

In elliptical coordinates (R, θ, Z), the Poisson equation can be written as

$$\left[\frac{1}{\zeta^2}\frac{\partial^2}{\partial R^2} + \frac{\partial^2}{\partial \theta^2} + \frac{a^2(\cosh^2 r - \cos^2\theta)}{\kappa^2}\frac{\partial^2}{\partial Z^2}\right] U(R,\theta,Z) = S(R,\theta,Z) \tag{E.1}$$

with boundary conditions

$$\alpha_{\pm} U(\theta, Z) + \beta_{\pm}\frac{\partial U(\theta,Z)}{\partial R} = F_{\pm}(\theta, Z), \quad \text{at} \quad R = \pm 1 \tag{E.2}$$

$$A_{\pm} U(R, \theta) + B_{\pm}\frac{\partial U(R,\theta)}{\partial Z} = H_{\pm}(R, \theta), \quad \text{at} \quad Z = \pm 1, \tag{E.3}$$

where $r = \zeta R + \xi$.

We first procced to expand the Poisson equation and its boundary conditions as

$$\begin{Bmatrix} U(R,\theta,Z) \\ S(R,\theta,Z) \\ F_{\pm}(\theta,Z) \end{Bmatrix} = \sum_{m=-\frac{M}{2}}^{\frac{M}{2}-1}\sum_{n=0}^{N} \begin{Bmatrix} U_{mn}(R) \\ S_{mn}(R) \\ f_{\pm mn} \end{Bmatrix} e^{im\theta} T_n(Z), \tag{E.4}$$

and

$$H_{\pm}(R,\theta) = \sum_{m=-\frac{M}{2}}^{\frac{M}{2}-1} h_{\pm mn}(R) e^{im\theta}. \tag{E.5}$$

Reproduced with permission of the copyright owner. Further reproduction prohibited without permission. www.manaraa.com

Substitution of Eqn. (E.4) into Poisson equation (E.1) yields

$$\sum_{m=-\frac{M}{2}}^{\frac{M}{2}-1}\sum_{n=0}^{N}\left[\frac{1}{\zeta^2}\frac{\partial^2}{\partial R^2}-m^2\right]U_{mn}(R)e^{im\theta}T_n(Z)+\frac{a^2\cosh^2 r}{\kappa^2}\sum_{m=-\frac{M}{2}}^{\frac{M}{2}-1}\sum_{n=0}^{N}U_{mn}(R)e^{im\theta}T_n''(Z)$$

$$-\frac{a^2\cos^2\theta}{\kappa^2}\sum_{m=-\frac{M}{2}}^{\frac{M}{2}-1}\sum_{n=0}^{N}U_{mn}(R)e^{im\theta}T_n''(Z)=S(R,\theta,Z). \tag{E.6}$$

It is easy to proof the following identity

$$\cos^2\theta\sum_{m=-\frac{M}{2}}^{\frac{M}{2}-1}a_m e^{im\theta}=\sum_{m=-\frac{M}{2}}^{\frac{M}{2}-1}\frac{1}{4}[a_{m-2}+2a_m+a_{m+2}]e^{im\theta}. \tag{E.7}$$

Applying the above identity on the last term at the left-hand side of Eqn. (E.6), we rewrite Eqn. (E.6) as

$$\sum_{m=-\frac{M}{2}}^{\frac{M}{2}-1}\sum_{n=0}^{N}\left[\frac{1}{\zeta^2}\frac{\partial^2}{\partial R^2}-m^2\right]U_{mn}(R)e^{im\theta}T_n(Z)+\frac{a^2\cosh^2 r}{\kappa^2}\sum_{m=-\frac{M}{2}}^{\frac{M}{2}-1}\sum_{n=0}^{N}U_{mn}(R)e^{im\theta}T_n''(Z)$$

$$-\frac{a^2}{4\kappa^2}\sum_{m=-\frac{M}{2}}^{\frac{M}{2}-1}\sum_{n=0}^{N}[U_{m-2,n}(R)+2U_{mn}(R)+U_{m+2,n}(R)]e^{im\theta}T_n''(Z)=S(R,\theta,Z). \tag{E.8}$$

By introducing a Chebyshev-Tau representation (Gottlieb and Orszag, 1977) to incorporate the boundary conditions (E.3) at $Z=\pm 1$, and by applying the recurrence relations for the derivatives of Chebyshev polynomials, we derive

$$\frac{\partial^2 U}{\partial Z^2}=\sum_{m=-\frac{M}{2}}^{\frac{M}{2}-1}\sum_{n=1}^{N-1}U_{mn}(R)e^{im\theta}T_n''(Z)=\sum_{m=-\frac{M}{2}}^{\frac{M}{2}-1}\sum_{n=1}^{N-1}U_{mn}^{(0,2)}(R)e^{im\theta}T_n(Z), \tag{E.9}$$

where

$$U_{mn}^{(0,2)}(R)=\sum_{q=0}^{N-2}\gamma_{nq}U_{mq}(R)+D_{mn}(R), \tag{E.10}$$

with γ_{nq} and $D_{mn}(R)$ given in Appendix A. Substitution of Eqns. (E.9) into the Poisson equation (E.8) yields

$$\left[\frac{1}{\zeta^2}\frac{\partial^2}{\partial R^2}-m^2\right]U_{mn}(R)+\frac{a^2\cosh^2 r}{\kappa^2}\sum_{q=0}^{N-2}\gamma_{nq}U_{mq}(R)$$

$$-\frac{a^2}{4\kappa^2}\sum_{q=0}^{N-2}\gamma_{nq}[U_{m-2,q}(R)+2U_{mq}(R)+U_{m+2,q}(R)]$$

$$=S_{mn}(R)+\frac{a^2}{4\kappa^2}[D_{m-2,n}(R)+2D_{mn}(R)+D_{m+2,n}(R)]\equiv\sigma_{mn}(R), \tag{E.11}$$

Reproduced with permission of the copyright owner. Further reproduction prohibited without permission. www.manaraa.com

for $m = -\frac{M}{2}$ to $\frac{M}{2} - 1$, and $n = 1$ to $N - 1$.

To avoid solving Eqn. (E.11) with full coupling between m with n, we proceed to diagonalize the matrix Γ with elements γ_{nq} using the same diagonalization techniques used in the case of cylindrical coordinates. Eqn. (E.11) can thus be reduced to

$$\left[\frac{1}{\zeta^2}\frac{\partial^2}{\partial R^2} - m^2\right]\hat{U}_{mn}(R) + \frac{a^2}{\kappa^2}\lambda_n\left[\cosh^2 r\hat{U}_{mn}(R) - \frac{1}{4}(\hat{U}_{m-2,n}(R) + 2\hat{U}_{mn}(R) + \hat{U}_{m+2,n}(R))\right] = \hat{\sigma}_{mn}(R). \tag{E.12}$$

Here λ_n are the eigenvalues of Γ, and $\hat{U}_{mn}(R)$ and $\hat{\sigma}_{mn}(R)$ are elements of matrices $\hat{\mathbf{U}}$ and $\hat{\mathbf{\Sigma}}$ respectively, which satisfies

$$\begin{aligned} \mathbf{U} &= \hat{\mathbf{U}}\boldsymbol{\epsilon}^T, \\ \mathbf{\Sigma} &= \hat{\mathbf{\Sigma}}\boldsymbol{\epsilon}^T, \end{aligned} \tag{E.13}$$

with $\boldsymbol{\epsilon}$ being is the eigenvector matrix of Γ, and $\boldsymbol{\epsilon}^T$ its transpose.

To remove the remaining coupling between m with n, we write Eqn. (E.12) as

$$\left[\frac{1}{\zeta^2}\frac{\partial^2}{\partial R^2} - m^2 + \frac{a^2}{\kappa^2}\lambda_n\cosh^2 r\right]\hat{U}_{mn}(R) - \frac{a^2\lambda_n}{4\kappa^2}\sum_{q=-\frac{M}{2}}^{\frac{M}{2}-1}\gamma'_{mq}\hat{U}_{qn}(R) = \hat{\sigma}_{mn}(R), \tag{E.14}$$

where γ'_{mq} are elements of matrix Γ', which is defined as

$$[\Gamma'] = \begin{bmatrix} 2 & 0 & 1 & 0 & 0 & \dots & 0 & 1 & 0 \\ 0 & 2 & 0 & 1 & 0 & \dots & 0 & 0 & 1 \\ 1 & 0 & 2 & 0 & 1 & \dots & 0 & 0 & 0 \\ 0 & 1 & 0 & 2 & 0 & \dots & 0 & 0 & 0 \\ & & & & & \dots & & & \\ 0 & 0 & 0 & 0 & 0 & \dots & 0 & 1 & 0 \\ 0 & 0 & 0 & 0 & 0 & \dots & 2 & 0 & 1 \\ 1 & 0 & 0 & 0 & 0 & \dots & 0 & 2 & 0 \\ 0 & 1 & 0 & 0 & 0 & \dots & 1 & 0 & 2 \end{bmatrix}. \tag{E.15}$$

Reproduced with permission of the copyright owner. Further reproduction prohibited without permission. www.manaraa.com

We then use the same diagonalization technique used above to diagonalize matrix $\mathbf{\Gamma}'$, and reduce Eqn. (E.14) to

$$\left[\frac{1}{\zeta^2}\frac{\partial^2}{\partial R^2} - m^2 + \frac{a^2}{\kappa^2}\lambda_n \cosh^2 r\right]\hat{\tilde{U}}_{mn}(R) - \frac{a^2\lambda_n\lambda'_m}{4\kappa^2}\hat{\tilde{U}}_{mn}(R) = \hat{\tilde{\sigma}}_{mn}(R), \qquad \text{(E.16)}$$

or

$$\hat{\tilde{U}}''_{mn}(R) + \zeta^2\left\{-m^2 + \frac{a^2}{\kappa^2}\lambda_n\left[\cosh^2(\zeta R + \xi) - \frac{\lambda'_m}{4}\right]\right\}\hat{\tilde{U}}_{mn}(R) = \zeta^2\hat{\tilde{\sigma}}_{mn}(R), \quad \text{(E.17)}$$

for $m = -\frac{M}{2}$ to $\frac{M}{2} - 1$, and $n = 1$ to $N - 1$. Here λ'_m are the eigenvalues of $\mathbf{\Gamma}'$, and $\hat{\tilde{U}}_{mn}(R)$ and $\hat{\tilde{\sigma}}_{mn}(R)$ are elements of matrices $\hat{\tilde{\mathbf{U}}}$ and $\hat{\tilde{\mathbf{\Sigma}}}$ respectively, which satisfies

$$\begin{aligned} \hat{\mathbf{U}} &= \hat{\tilde{\mathbf{U}}}\boldsymbol{\epsilon}'^T, \\ \hat{\mathbf{\Sigma}} &= \hat{\tilde{\mathbf{\Sigma}}}\boldsymbol{\epsilon}'^T, \end{aligned} \qquad \text{(E.18)}$$

with $\boldsymbol{\epsilon}'$ being is the eigenvector matrix of $\mathbf{\Gamma}'$.

The ODE with variable R in Eqn. (E.17) can be solved using a spectral collocation method for each combination of m and n.

Reproduced with permission of the copyright owner. Further reproduction prohibited without permission. www.manaraa.com